University of Bath

PHD

Optical and electrical frequency-modulated studies of nanocrystalline electrodes

Franco, Gabriella

Award date:
1999

Awarding institution:
University of Bath

Link to publication

Alternative formats
If you require this document in an alternative format, please contact:
openaccess@bath.ac.uk

Copyright of this thesis rests with the author. Access is subject to the above licence, if given. If no licence is specified above, original content in this thesis is licensed under the terms of the Creative Commons Attribution-NonCommercial 4.0 International (CC BY-NC-ND 4.0) Licence (https://creativecommons.org/licenses/by-nc-nd/4.0/). Any third-party copyright material present remains the property of its respective owner(s) and is licensed under its existing terms.

Take down policy
If you consider content within Bath's Research Portal to be in breach of UK law, please contact: openaccess@bath.ac.uk with the details. Your claim will be investigated and, where appropriate, the item will be removed from public view as soon as possible.

Download date: 05. May. 2023

OPTICAL AND ELECTRICAL FREQUENCY-MODULATED STUDIES OF NANOCRYSTALLINE ELECTRODES

submitted by **Gabriella Franco**

for the degree of PhD

of the University of Bath

1999

COPYRIGHT

Attention is drawn to the fact that copyright of this thesis rests with its author. This copy of the thesis has been supplied on condition that anyone who consults it is understood to recognize that its copyright rests with its author and that no quotation from the thesis and no information derived from it may be published without prior written consent of the author.

This thesis may be made available for consultation within the University Library and may be photocopied or lent to other libraries for purposes of consultations.

Gabriella Franco

UMI Number: U532746

All rights reserved

INFORMATION TO ALL USERS
The quality of this reproduction is dependent upon the quality of the copy submitted.

In the unlikely event that the author did not send a complete manuscript
and there are missing pages, these will be noted. Also, if material had to be removed,
a note will indicate the deletion.

UMI U532746
Published by ProQuest LLC 2013. Copyright in the Dissertation held by the Author.
Microform Edition © ProQuest LLC.
All rights reserved. This work is protected against
unauthorized copying under Title 17, United States Code.

ProQuest LLC
789 East Eisenhower Parkway
P.O. Box 1346
Ann Arbor, MI 48106-1346

UNIVERSITY OF BATH
LIBRARY
30 - 6 JUL 1999

A mamma e papà

University of Bath

School of Chemistry

Doctor of Philosophy

OPTICAL AND ELECTRICAL FREQUENCY-MODULATED STUDIES OF NANOCRYSTALLINE ELECTRODES

By

Gabriella Franco

ABSTRACT

Electron transport in dye-sensitised and dye-free porous TiO_2 films was investigated using frequency-resolved techniques: photoelectrochemical impedance spectroscopy (PEIS), intensity modulated photocurrent spectroscopy (IMPS), intensity modulated photovoltage spectroscopy (IMVS) and photomodulated infrared transmittance spectroscopy (PITS).

An inhomogeneous dye distribution in dye-sensitised nanocrystalline solar cells was detected using IMPS. The presence of a dye-free region was taken into account in the generation/collection equation which describes the photoelectrochemical behavior of

porous systems. Comparison of the experimental IMPS response with the predictions of the model indicated a dye-free region of 4μm. IMPS measurements were also performed on dye-free TiO_2 electrodes, and these were interpreted as evidence for non-homogeneous porosity. It is proposed that the film near the substrate is compact and the net injection efficiency is very low.

The combination of IMPS, PEIS, IMVS and PITS on a dye-sensitised solar cell allowed determination of the absorption cross section of electrons at 940nm ($10^{-17}cm^2$). The net electron injection efficiency was also evaluated from these measurements and it was found to be 1 at short circuit and 0.3 at open circuit, indicating that under strong accumulation the reaction of electrons with the oxidised dye competes with dye regeneration. It was also found that the majority of the electrons detected were trapped and relaxed predominantly via back reaction with I_3^-.

Potential-modulated infrared transmittance was performed on dye-free TiO_2 under strong accumulation. The optical cross section of electrons was found to be $5\times10^{-19}cm^{-2}$. The discrepancy between this result and the value obtained by PITS measurements was attributed to the fact that free electrons dominate the optical response in this experiment.

ACKNOWLEDGEMENTS

My first thank you goes to Professor Laurence M. Peter, who supported my work during these three years with enthusiasm, broad scientific knowledge and novel ideas. Thank you also to Dr. D. Jason Riley, who supervised me together with Prof. Peter during my first year. I would also like to thank K. G. U. Wijayantha for making the TiO_2 cells and I. Lauermann and I. Uhlendorf (INAP) for providing the dye-sensitized solar cells. Many thanks to E. Ponomarev as well, who I met very briefly in Paris, for giving me the starting point of the model developed in the present work. I am thankful to the members of the staff of the School of Chemistry: Dr. A. C. Fisher, Dr. G. J. Price, Dr. S. Roser, Dr. P. Bartlett and Dr. J. Chalmers for enlightening discussions. I would also like to thank Mrs. P. Croft for her kind assistance, Dr. M. Bailes and J. Collins for their technical support. Many thanks to all members of the group: some are still here, some have left: Gareth, Laurent, Fulian, Steve, Siva, Mallika, Greg, Pete, Nicola, Rachel, Upul, Alicia, Ruilin, Silvan, Khaled, Noel and Nia. I would also like to thank my friends: Mario, who has pioneered a whole generation of Italians in England, Diego, Stefania, Antonella, Nicki, Christabelle, Kim, Wendy, Roger, Sergio, Cristiana and her daughter Margherita. I am also thankful to my friends in Italy who have supported me with their E-mails: Alberto, Camilla, Cristina, Piero and Simona. I am mostly thankful to my wonderful parents who supported my decision to move and work away for all these years, far and away they have always helped me. Finally thank you to my boyfriend, Jason, for believing in me.

To all many thanks,

Gabriella

GLOSSARY OF SYMBOLS

$A(\omega)$	Attenuation factor
A/V	Surface area to volume ratio
C	Capacitance
C_{cb}	Conduction band capacitance
C_{sc}	Space charge region capacitance
C_t	Surface state capacitance
C_{tot}	Total capacitance
D	Diffusion coefficient
d	Film thickness
D_{eff}	Effective diffusion coefficient
d_{sc}	Width of the space charge region
$E_A/E^0_{redox}/ E^0$	Standard redox energy
E_C	Energy of the conduction band edge
E_{fb}	Flat band energy
E_F	Fermi level energy
$E_{F,n}$	Electron quasi-Fermi level
$E_{F,p}$	Hole quasi-Fermi level
E_g	Band-gap energy
$E_{n,d}$	Electron demarcation level
$E_{p,d}$	Hole demarcation level
E_{ox}	Energy of the oxidised agent
E_{red}	Energy of the reduced agent

E_{redox}	Redox energy
E_V	Energy of the valence band edge
f(E)	Fermi-Dirac probability distribution function
$G(\omega)$	Gain
h	Plank's constant
h^+	Hole
i	$\sqrt{-1}$
I_0	Incident photon flux
δI_0	Modulated incident photon flux
I_t	Transmitted photon flux
j_0	Saturation dark current density
j_{photo}	Short circuit photocurrent density
k	Boltzmann constant
k_{rec}	Electron recombination with I_3^- rate constant
k^0_{ext}	Extraction rate constant at open circuit
k^0_{inj}	Injection rate constant at open circuit
k_{back}	Electron recombination with the dye rate constant
k_{detrap}	Electron detrapping rate constant
k_{ETfree}	Free hole transfer rate constant
k_{ETtrap}	Trapped hole transfer rate constant
k_{ext}	Electron extraction rate constant
k_{inj}	Electron injection rate constant
k_{reg}	Dye regeneration rate constant
$k_{release}$	Thermal release rate constant
k_{trap}	Electron trapping rate constant

L	Hole diffusion length
L_d	Electron diffusion length
m	Non-ideality factor
n	Electron concentration
N	Trapped electron concentration
$n(0)$	Electron concentration at the surface
n_0	Electron concentration in the dark at equilibrium
N_C	Total number of states in the conduction band
N_d	Electron donor concentration
n_t^0	Trapped electron concentration in the dark at equilibrium
N_V	Total number of states in the valence band
Δn	Excess of electron concentration
$\delta n/\delta n_f$	Free electron modulated concentration
δn_t	Trapped electron modulated concentration
Ox	Oxidising agent
p	Hole concentration
$p(0)$	Hole concentration at the surface
p_0	Hole concentration in the dark at equilibrium
Δp	Excess of hole concentration
q	Elementary charge
Q_{cb}	Free charge
Q_t	Trapped charge
δQ_{cb}	Modulated conduction band charge
δQ_{tot}	Modulated total charge
r	Radius

R	Resistance
R/O	Redox couple
R_{ct}	Charge transfer resistance
R_{detrap}	Detrapping resistance
Red	Reducing agent
R_{el}	Electrolyte resistance
R_S	Serial resistance
R_{sheet}	Sheet resistance
T	Absolute temperature
t	Time
T_{oc}	Open circuit transmission
$\Delta T/T$	Normalised transmittance
U_{fb}	Flat band potential
U_{photo}	Photovoltage
δU_{photo}	Modulated photovoltage
V	Voltage
$\hat{V}$	Complex notation of periodic voltage
$\|V\|$	Amplitude of the periodic voltage
V_H	Potential drop across the Helmholtz layer
V_{oc}	Open circuit voltage
X	Filled surface state
x	Spatial co-ordinate
X^+	Vacant surface state
Z	Impedance
α	Absorption coefficient

β	Symmetry factor/ Normalised absorption coefficient
β_n	Electron capture rate constant
β_p	Hole capture rate constant
ε	Relative permittivity
ε_0	Permittivity of free space
φ	Migration potential
ϕ	Phase shift
Φ	Photocurrent conversion efficiency
$\Delta\phi_{SC}$	Potential drop across the space charge region
ϕ_{sol}	Potential of the solution
λ	Reorganisation energy/Wavelength
μ_p	Mobility of holes
η	Net electron injection efficiency
σ	Optical cross section
σ_f	Free electron optical cross section
σ_t	Trapped electron optical cross section
τ	Electron lifetime
τ_D	Electron diffusion time
τ_{eff}	Electron effective lifetime
τ_p	Hole lifetime
τ_{trap}	Trapped electron lifetime
ω	Radial frequency
ω_{MIN}	Radial frequency corresponding to the minimum in the complex plot

ABBREVIATIONS

EIS	Electrochemical Impedance Spectroscopy
IMPS	Intensity Modulated Photocurrent Spectroscopy
IMVS	Intensity Modulated Photovoltage Spectroscopy
IPCE	Incident Photon to Current Conversion Efficiency
MLCT	Metal-to-Ligand Charge Transfer
MOCVD	Metal Organic Chemical Vapour Deposition
ohp	Outer Helmholtz Plane
PEIS	Photoelectrochemical Impedance Spectroscopy
PITS	Photomodulated Infrared Transmittance Spectroscopy
SCR	Space Charge Region

INDEX

CHAPTER I-INTRODUCTION	1-28
1.1 Introduction	1
1.2 Titanium Dioxide	2
1.2.1 General Features	2
1.2.2 Preparation	4
1.2.3 Applications	5
1.3 Dye-Sensitised Nanocrystalline TiO_2 Solar Cells	6
1.3.1 Overview	6
1.3.2 Timescale of the Mechanisms	8
1.3.3 Electrolyte	9
1.3.4 Dyes	9
1.3.5 Current-Voltage Characteristics	11
1.4 Dye-Free Porous Systems	12
1.5 Experimental Methods to Study Charge Transport in Nanocrystalline Electrodes	13
1.6 Conclusion	15
1.7 References	16
CHAPTER II-PHOTOELECTROCHEMISTRY	29-54
2.1 Introduction	29
2.2 Semiconductors and Electrolytes	30
2.3 The Double Layer	34
2.4 Flat Electrodes	37
2.4.1 Semiconductor/Electrolyte Interface in the Dark	37

2.4.2 Semiconductor/Electrolyte Interface under Illumination 39

2.4.3 Interfacial Processes 41

2.5 Porous Electrodes 44

2.5.1 Porous Semiconductor Electrodes 44

2.5.2 Porous Semiconductor Electrodes under Illumination 46

2.6 Conclusion 51

2.7 References 52

CHAPTER III–THEORY 55-91

3.1 Introduction 55

3.2 Ac Techniques 56

3.3 Intensity Modulated Photovoltage Spectroscopy 65

3.4 Photoelectrochemical Impedance Spectroscopy 69

3.5 Intensity Modulated Photocurrent Spectroscopy 72

3.5.1 The Generation/Collection Problem: Steady State and Periodic Solutions 72

3.5.2 The Influence of Electron Trapping and Detrapping 83

3.6 Photomodulated Infrared Transmittance Spectroscopy 85

3.7 Conclusion 90

3.8 References 90

CHAPTER IV-EXPERIMENTAL METHODS 92-104

4.1 Introduction 92

4.2 Preparation of the Samples 93

4.2.1 Dye-Sensitised TiO_2 Nanocrystalline Photovoltaic Cells 93

4.2.2 Dye-Free TiO_2 Nanocrystalline Cells 94

4.3 Intensity Modulated Photocurrent Spectroscopy 96

4.4 Intensity Modulated Photovoltage Spectroscopy 99

4.5 Photoelectrochemical/Electrochemical Impedance Spectroscopy 99

4.6 Photomodulated Infrared Transmittance Spectroscopy 100

4.7 Dc Current-Voltage Measurements 102

4.8 Potential-Modulated Infrared Transmittance 102

4.9 References 103

CHAPTER V-INTENSITY MODULATED PHOTOCURRENT SPECTROSCOPY 105-127

5.1 Introduction 105

5.2 Theory 106

5.3 Experimental Section 109

5.3.1 Dye-Sensitised Nanocrystalline TiO_2 Cells 109

5.3.2 Dye-Free Nanocrystalline TiO_2 `Cells 110

5.4 Results and Discussion 111

5.4.1 Dye-Sensitised Nanocrystalline TiO_2 Cells 111

5.4.2 Dye-Free Nanocrystalline TiO_2 Cells 116

5.5 Conclusion 126

5.6 References 126

CHAPTER VI-FREQUENCY-RESOLVED OPTICAL DETECTION OF ELECTRONS 128-143

6.1 Introduction 128

6.2 Experimental Section 129

6.3 Results and Discussion 130

6.3.1 Calculation of the Optical Absorption Cross Section of Electrons 130

6.3.2 Calculation of the Net Electron Injection Efficiency at Open Circuit 133

6.3.3 Analysis of the Frequency Dependence of the Photomodulated Transmittance 136

6.3.4 Trapping and Back Reaction in Dye-Sensitised Cells 139

6.4 Conclusion 141

6.5 References 142

CHAPTER VII-POTENTIAL-MODULATED TRANSMITTANCE 144-157

7.1 Introduction 144

7.2 Theory 145

7.3 Experimental Section 148

7.4 Results and Discussion 150

7.5 Conclusion 156

7.6 References 156

CHAPTER VIII-CONCLUSIONS 158-161

8.1 Conclusions 158

8.2 References 161

CHAPTER I

INTRODUCTION

1.1 Introduction

The work presented in this thesis describes studies on porous nanocrystalline TiO_2; both dye-sensitised and dye-free TiO_2 have been investigated. In this chapter the main features of single crystal and porous TiO_2 are reviewed with reference to the literature. Recently porous TiO_2, and especially dye-sensitised porous TiO_2, has attracted great scientific interest as efficient photovoltaic devices can be built from this material. The first group to produce photovoltaic devices from dye-sensitised porous TiO_2 was Grätzel and co-workers [1] in Switzerland in 1991. Since then an expanding body of work has been undertaken to investigate these novel devices which could be the answer to the need for new sources of electric energy. Work is in progress to make these devices financially viable in the near future as a real alternative to silicon. However, the Grätzel cell is also very interesting from a scientific point of view as it involves a variety of processes taking place over a wide range of timescales. These processes can be analysed using time and frequency-resolved techniques. The present work sets out to study electron transport in the Grätzel cell, and in porous systems in general, identifying the processes occurring in the system and how they affect the efficiency of the photovoltaic device.

1.2 Titanium Dioxide

1.2.1 General Features

Titanium dioxide, TiO_2, is a wide indirect band-gap (3-3.2eV) semiconductor and it absorbs in the ultra-violet. It is, therefore, transparent to visible light and it absorbs at about 370nm. There are three different crystalline structures of TiO_2: rutile, anatase and brookite. Rutile is the most thermodynamically stable and it crystallises in the tetragonal system, in which six oxygen atoms form distorted octahedra around the titanium with four shorter and two longer Ti-O distances. Anatase has a very similar tetragonal structure but with slightly different octahedra. This difference in their crystalline structure makes the densities of the two forms of TiO_2 quite different. The density of anatase, $3.89gcm^{-3}$, is lower than the density of rutile, $4.26gcm^{-3}$ [2].

The electronic structure of the valence band is composed of oxygen $2p$ orbitals hybridised with titanium $3d$ orbitals. The electronic structure of the conduction band is primarily composed of titanium $3d$ orbitals [2-5]. Although the structures of rutile and anatase are well known, to date no theoretical calculations have been able to explain fully their electronic properties. Only the tight-binding linear combination of atomic orbitals Hamiltonian was able to produce the correct band-gap of 3eV [6]. The modelling of the electronic structure of TiO_2 is difficult because crystal defects cannot be neglected when evaluating the electronic properties of TiO_2.

The physical and catalytic properties [7,8] of single crystal rutile have been investigated for a long time. Only recently has single crystal anatase been studied and analysed in more detail [9]. Comparing the electrical and optical properties of anatase and rutile it was found that anatase luminescences strongly at 500nm, whilst no luminescence was observed for rutile. The luminescence of anatase has been explained by the emission of self-trapped excitons localised in the TiO_6-octahedra [10,11]. This demonstrates the importance of crystal defects in these materials. In other experiments,

it has also been shown that anatase is a *n*-type semiconductor [12].

As mentioned above, TiO_2 is an indirect band-gap semiconductor of 3.05eV [13] for rutile and of 3.2eV [14] for anatase. However, oxygen vacancies form inter-band states at an energy of 1-1.4eV below the conduction band edge [15,16]. The presence of these inter-band states is responsible for the absorption tails of the main absorption edge, the so-called Urbach tails [17]. These tails are observed in the UV-visible absorption spectrum of both rutile and anatase single crystals [11].

Recently, TiO_2 nanocrystalline films have become more interesting than single crystals due to their exciting properties. Nanocrystalline films consist of small particles with diameters of 1-1000nm packed to form a porous structure; this enhances their active surface area. The most common technique to make nanocrystalline film is the sol-gel method; starting from the synthesis of the colloid, which is then deposited on the desired substrate by screen printing or spreading [18]. This technique can be extended to other oxides such as SiO_2 [19-23], ZnO [24-26] or Nb_2O_5 [27,28]. If the particle size is very small, electrons in the particles become 'quantum confined'. This means that the band-gap becomes wider as the particle size is decreased [18,29,30]. However, the dimensions of the particles used in the present work are too big to show quantum confinement effects.

When equilibrium is established between a single crystal semiconductor and a redox couple, the energy bands of the semiconductor are subject to bending, i.e. an electrical field forms in the space charge region [31,32]; for further detail see chapter II. However, for nanoparticulate semiconductor systems it can occur that the particle size is of the same order of magnitude as the space charge region, and therefore no band bending takes place. According to theoretical calculations [33], nanocrystalline TiO_2 with small particles (<20nm) should not show bending at potentials positive of E_{fb}. This means that no depletion layer forms.

Another interesting aspect of semiconductors, and especially nanocrystalline semiconductors, is intercalation or insertion of small cations. Intercalation was observed in smooth TiO_2 films prepared by metal organic chemical vapour deposition (MOCVD) [34] and sputtering [35]. Kinetic experiments [35] appear to indicate that the insertion of lithium is limited to the accumulation layer of the semiconductor (≈11nm). However this would not explain the high insertion yield of about x=0.6 (x=TiO_2/Li) found for anatase particles of 0.25μm [36]. Lindström et al. [37] studied the intercalation of lithium into nanocrystalline TiO_2 and compared the results to those of MOCVD films. They ascertained that the insertion-extraction process is significantly more reversible in nanocrystalline films and that the rate constant of insertion into a 50% porous film is 300 times faster compared to dense films in the potential range between 0 and –1.5V vs. Ag/AgCl. Obviously, the mechanism for intercalation seems to be not only function of the lattice structure but also of the morphology.

1.2.2 Preparation

Nanocrystalline TiO_2 can be prepared by dip-coating, sol-gel, vapour-phase techniques and by electrophoresis. In dip-coating, an alcoholic solution of $TiCl_4$ is brought onto the substrate and, after evaporation of the solvent, the films are hydrolysed in humid air and annealed at about 450^0C. The procedure is repeated several times to produce films of a thickness of several micrometers [38]. The evaporation and annealing steps produce cracks in the film, which are the sources of the porous structure.

Sol-gel colloidal synthesis of metal oxides is widely used and has been reported in reviews and books [19-23,39-41]. The most frequent preparation of TiO_2 colloids is based on the arrested hydrolysis of alkoxides of titanium [1]. During the hydrolysis,

primary particles of TiO_2 are formed with typical diameters of 5-10nm. These particles are peptised in an acidic or basic environment at about 80^0C to avoid aggregation of these particles. However at present it is not clear whether this step is really necessary for the synthesis of high quality colloids of TiO_2 [42]. To increase the particle size and crystallinity, the sol is auto-claved at temperatures of 200-250 ^{0}C for several hours. Eventually, dispersions of anatase or rutile particles with typical diameters of 10-20nm are obtained. These can be spread or screen-printed on substrates and fired at temperatures of 400-550^{0}C. To avoid cracking of the films during heat treatment, additives such as derivatives of polyethyleneglycol (Triton-X or carbowax) are introduced in small quantities to the dispersion before depositing the film.

The vapour-phase preparation can be divided into two different approaches: (1) direct depositions of nanocrystalline films via aerosol formation of volatile titanium compounds and (2) preparation of TiO_2 particles by hydrolysis of $TiCl_4$ vapour in a flame of a plasma [43] followed by the processing of these particles into pastes. These dispersions can also be used as starting materials for electrophoretic deposition of nanocrystalline porous TiO_2 films [44]. In this technique, the electrode to be coated is placed into an electrochemical cell and the deposition is carried out under constant current conditions until the film thickness is satisfactory.

1.2.3 Applications

There are many applications of porous TiO_2 films based on charge transfer between either a solution species and nanocrystalline TiO_2 electrodes or between a surface-bound molecular modifier and TiO_2. Devices without surface attached molecules rely exclusively on the intrinsic properties of nanocrystalline TiO_2 films. Some of these devices are based on intercalation such as batteries [45] and

electrochromic devices [46]. Other applications are electrocatalysis [47-49], photoelectrocatalysis [50-53], electroluminescence [54-56] and sensors [57,58]. Recently devices based on nanocrystalline TiO_2 films with molecular modification have drawn significant scientific interest. Electrochromics [59,60], photochromics [61,62], sensitised photochromics [63], electrocatalysis [64], electroluminescence [65-67], sensors [68,69] and photovoltaic devices [1] are amongst the applications of modified nanocrystalline TiO_2. Especially photovoltaic devices have attracted great scientific interest in the last decade and they are the main object of investigation of the present work.

1.3 Dye-Sensitised Nanocrystalline TiO_2 Solar Cells

1.3.1 Overview

In the 1970s and 1980s, conversion of solar energy into electricity was of great interest. Most of the work was carried out on smooth semiconducting films [70-80]. The light harvesting efficiencies of these materials did not prove to be very high, the best result obtained was below 1%. Dye-sensitisation was introduced by Matsumura et al. [81] and Alonso et al. [82] on ZnO. Later Willig et al. [83] reported higher quantum yields in dye-sensitising SnS_2, but the conversion yields were still below 1%. At the beginning of the 1990s there was a major breakthrough in this field, when Grätzel and co-workers [1] used TiO_2 porous electrodes. The high surface area to volume ratio of these electrodes dramatically enhanced the photocurrent efficiencies, and values close to unity were achieved. **Figure 1.1** illustrates the principle of dye-sensitised solar cells. The light absorbed by the dye excites an electron to the upper LUMO orbital of the dye, the electron is then injected into the conduction band of the TiO_2 semiconducting porous film and then is collected at the back contact; usually a tin oxide coated glass.

The I^- ions in solution replace the hole left in the HOMO state of the dye, regenerating the cell. This is possible as the particle size in the nanocrystalline phase is small and the electrolyte phase penetrates throughout the porous solid phase. The electron diffusion time in the cell is very slow, therefore for the dye-sensitised solar cell to be efficient it is essential that the rate of reaction of electrons with I_3^- is even slower. It has been shown [84-86] that the photogenerated electrons require several milliseconds to diffuse to the back contact in a 10μm film. If the electron lifetime for back reaction of photoinjected electrons with I_3^- is longer than the transit time the short circuit collection efficiency approaches 100%.

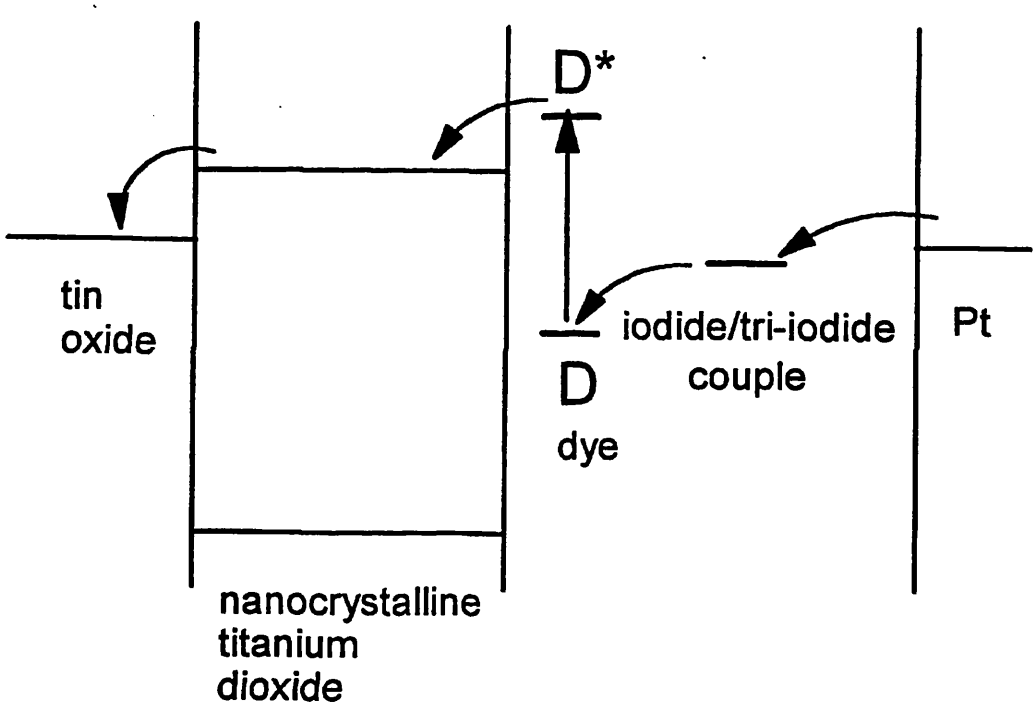

Figure 1.1. Energy scheme for the regenerative dye-sensitised TiO_2 cell. Photo-excitation of the dye is followed by rapid electron injection into the conduction band of the oxide. The dye is regenerated rapidly from its oxidised state by I^-. Electrons collected at the tin oxide substrate pass via the external circuit to the counter electrode where they reduce I_3^- back to I^-.

1.3.2 Timescale of the Mechanisms

In the Grätzel cell, processes occur over a wide range of timescales. The shortest timescale is associated with the injection of an electron from the excited state of the dye into the conduction band of TiO_2. Spectroscopic studies [87,88] have established that this process occurs on the femtosecond timescale. The oxidised dye is then regenerated rapidly (ns) by reaction with I^- [89]. The injected electrons are collected at the tin oxide coated glass back contact, and the I_3^- produced in the dye regeneration reaction diffuses to the counter electrode, where it is reduced back to I^-. These two processes are slow as they involve diffusion of ions and electrons; the injected electrons and the photogenerated I_3^- require several milliseconds to diffuse to the respective contacts. Another important process in dye-sensitised solar cells is recombination of electrons with D^+. This process depends strongly on the applied voltage and it can take from 200ms to 30ns [89]. For negative bias, i.e. under strong accumulation, it is a very fast process because of the high concentration of electrons in the conduction band and traps of TiO_2. It occurs more slowly as the bias approaches 0V. Another process of interest is the electron recombination with I_3^-, which in order for photovoltaic cells to be efficient must be slower than the electron transit time to the back contact. Schlichthörl et al. [90] have shown that the electron lifetime depends on the concentration of I_3^- in the electrolyte and on the illumination intensity. Normally under illumination of 1 sun the electron lifetime is about 10ms. Finally, trapping and detrapping rates in dye-sensitised nanocrystalline TiO_2 cells must be considered. They depend mostly on the trap density, and for high densities, the processes can occur in the range on nanoseconds.

The rates of the processes described above have been measured using time and frequency-resolved measurements. In the present work frequency-resolved techniques have been applied to study dye-sensitised TiO_2 photovoltaic cells and porous TiO_2 electrodes. Although no time resolved experiments were performed, the relationship in

between frequency and time domain experiments is discussed in section 3.2.

1.3.3 Electrolyte

An important aspect of dye-sensitised solar cells is the back reaction of electrons with I_3^- ions in solution. According to Huang et al. [91] the order of this reaction is 0.7 with respect to the electron concentration and 2nd order in the concentration of the oxidised species. The second-order process is attributed [92,93] to the dismutation of I_2^- to I_3^- and I^-. Taking the dismutation reaction into consideration, the mechanism for the electron recombination is described as follows:

$$I_3^- \rightleftharpoons I^- + I_2 \tag{1.1}$$

$$e^- + I_2 \rightarrow I_2^- \tag{1.2}$$

$$2I_2^- \xrightarrow{slow} I_3^- + I^- \tag{1.3}$$

$$\text{net: } 2e^- + I_3^- \rightarrow 3I^- \tag{1.4}$$

The back electron transfer can, in principle, occur not only at the TiO_2/electrolyte interface but also at the SnO_2/electrolyte interface. However, it is reported [94] that due to the large surface area of the TiO_2 porous electrode, the back reaction mostly takes place at the TiO_2/electrolyte interface.

1.3.4 Dyes

The dye adsorption onto the TiO_2 porous electrode plays an important role for the functioning of the photovoltaic device. Conceptually, the sensitiser consists of an anchoring group (a linker) and a light absorber. The sensitiser absorbs the light and injects an electron into the conduction band of TiO_2. Many dyes have been employed

for the sensitisation of TiO_2 nanocrystalline films, for example: erythrosin B [95], eosin [96-100], rose bengal [101,102], rhodamines [103-107], cresyl violet [108-110], thionine [111], chlorophyllins [112,113], anthracene-9-carboxylate [114], 8-hydroxyquinoline [115], porphyrins [116], phthalocyanines [117,118], transition metal cyanides [119,120], $[Ru(bpy)_3]^{2+}$ and its analogues [1,121-130], cyanines [131-139], squaraines [140-142] and phenylfluorone [143]. The most successful family of sensitisers found so far has been the ruthenium complexes containing polypyridyl ligands [144-146], as shown in **Figure 1.2**. The absorption of **1** and other ruthenium complexes results from a metal-to-ligand charge transfer (MLCT). Work is still in process to try and obtain a high absorption coefficient and a fast injection rate at the same time. For example, it is possible to increase the absorbance of complex **1** by introducing phenyl groups between the carboxylates and the pyridyl ring of 4,4'-dicarboxy-2,2'-bipyridine, but the injection efficiency of the corresponding complex drops in comparison to **1**. This shows that the length of the linker and the electronic properties play an important role for the overall injection efficiency.

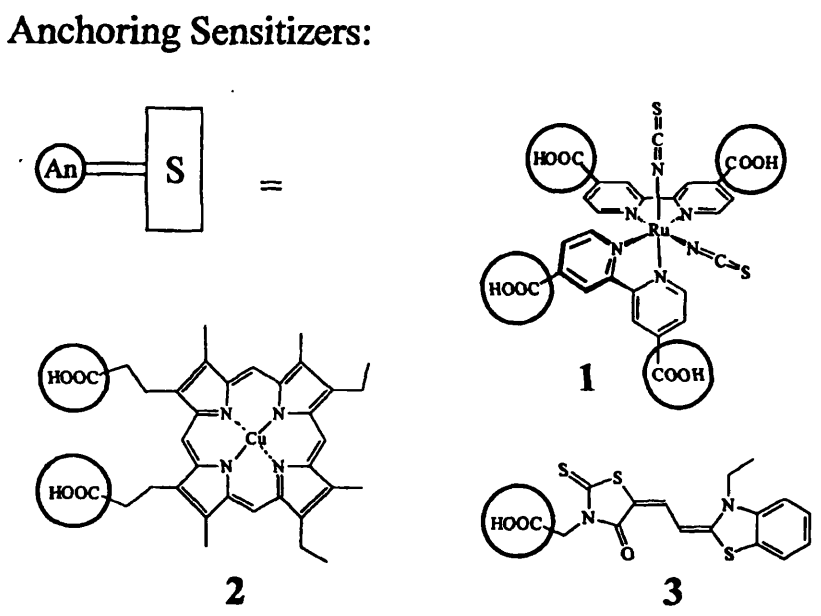

Figure 1.2. S are the different sensitisers (**1-3**) and An is the anchoring group. Compound **1** is *cis*-$(NCS)_2$-bis(2,2'-bipyridyl-4,4'-dicarboxylate)ruthenium(II), compound **2** is a chlorophyll derivative and compound **3** is a mesocyanine.

1.3.5 Current-Voltage Characteristics

Nanocrystalline solar cells can be compared with solid state p^+-i-n^+ solar cells. In a p-i-n solar cell hole-electron pairs are photogenerated in the intrinsic region and the electron travels towards the n^+ semiconductor and the holes towards the p^+ semiconductor. Under steady state conditions the flux of electrons towards one contact and of holes towards the other contact are the same. For a nanostructured cell the majority carrier, usually the electron, travels through the porous system reaching the back contact, whilst the hole reacts at the interface. In this way there are two fluxes, one of electrons and one of oxidised species in solution which is regenerated at the counter electrode. Under steady state conditions the number of electrons reaching the back contact is the same as the number of oxidised ions in solution [147].

For a nanoparticulate film, the expression for the photocurrent as function of the voltage, i.e. the I-V characteristics, can be obtained by solving the generation/collection equation (see equation 2.19) for the steady state case. Södergren et al. [148] have derived I-V characteristics for nanoparticulate films assuming that electron transport occurs via diffusion and that the recombination process is first-order in the electron concentration. The expression obtained is similar to the one of a p-i-n junction and it is given by:

$$j = j_{photo} - j_0\left(1 - e^{\frac{qV}{mkT}}\right) \tag{1.5}$$

where j_{photo} is the short circuit photocurrent, j_0 is the saturation dark current under reverse bias, V is the voltage and m is the non-ideality factor that is reported to be close to 2 for dye-sensitised cells [91,148]. The open circuit photovoltage $V_{photo}=V_{oc}$ is defined by the condition $j=0$, typical values of the open circuit photovoltage are 0.65V. The back reaction of electrons with D^+ can significantly contribute to the limitation of the open circuit voltage in dye-sensitised solar cells [89,129,149]. This means that at

open circuit recombination of electrons in TiO_2 with the oxidised state of the dye competes with the dye regeneration. Typical short circuit photocurrent densities, j_{photo}, are of about $18mAcm^{-2}$ at 1 sun (AM 1.5) [145,150]. j_{photo} is determined by light absorption, charge injection and collection. Only the light absorbed by the dye is expected to contribute to the short circuit photocurrent. When an electron is excited into the upper LUMO orbital it can either be injected into the TiO_2 or recombine with D^+, the latter process can obviously limit the photocurrent efficiency. This process can also be mediated by TiO_2 after the electron injection. The performance of the cell can also be limited by the recombination of photoinjected electrons with the I_3^- in solution before they reach the back contact.

1.4 Dye-Free Porous Systems

High quantum efficiencies have been reported for nanoparticulate systems, e.g. CdSe [151], these were attributed to the interpenetration between the electrolyte and the porous network. This means that the photogenerated minority carriers in the porous network are always close to the semiconductor/electrolyte interface, so that they can be captured by the reducing agent in solution instead of recombining. The photogenerated electron travels quite slowly through the porous network before reaching the back contact, photocurrent and photovoltage transients measured on porous ZnO show time constants in the μs to ms range [152,153]. Such a slow transport of photogenerated electrons thorough the nanoparticulate network can be attributed to the temporary localisation of electrons in the traps. An interesting porous system is based on *n*-type GaP [154], where the dimension of the particles are such that a depletion layer exits encouraging hole-electron separation. As the photogenerated holes in the porous network are within a distance smaller than their diffusion length, the recombination

losses can be neglected. The transit time of electrons in *n*-GaP is smaller compared with other porous systems, suggesting that electron localisation in the traps does not play an important role in this system. Photocurrent generation in dye-free nanoporous TiO_2 [155,156] presents different characteristics with respect to *n*-GaP. Firstly the hole-electron separation is not as effective, and this means that recombination losses can no longer be neglected. This is related to the fact that in nanoporous TiO_2 the size of the particles is such that there is no depletion layer which promotes hole-electron separation. Secondly electron transport in nanoporous TiO_2 is slower compared with *n*-GaP, suggesting that in the former system the temporary localisation of electrons in the traps is not negligible.

1.5 Experimental Methods to Study Charge Transport in Nanocrystalline Electrodes

Electron transport and reactions in porous electrodes have been extensively studied with a variety of spectroscopic techniques. For example, reactions involving dye-sensitised charge injection, regeneration and back-reaction have been analysed using picosecond and femtosecond transient laser techniques [87,129]. Other methods used include time of flight photocurrent measurements with pulsed laser excitation [84] and photocurrent response to chopped illumination [85]. The response of nanocrystalline systems to large variations of the light intensity is not linear, see section 3.2, i.e. the rise and fall of the photocurrent generally do not follow first order (exponential) kinetics. It follows that these experiments cannot be described with differential equations with constant coefficients. For this reason, techniques have been developed that use small amplitude perturbations of light or of voltage superimposed on a constant background value in order to allow linearisation. The most widespread frequency-resolved technique is electrochemical impedance spectroscopy [157-159]

(EIS), which analyses the response of electrochemical systems to periodic (sinusoidal) perturbations of voltage or current. Since in EIS both the perturbation and the response are electrical, the analysis of experimental data is normally based on linear equivalent circuit elements. EIS can be used to study semiconductor electrodes not only in the dark, but also under conditions of steady illumination, in which case it is termed photoelectrochemical impedance spectroscopy (PEIS) [160-165]. Another widely applied frequency-resolved technique is intensity modulated photocurrent spectroscopy (IMPS) [85,86,154-156,166-215] which involves modulation of the intensity of illumination incident on an electrode and measurement of the magnitude and phase shift of the resulting photocurrent relative to the periodic illumination. IMPS has been used to study a wide range of single crystal semiconductors as well as anodic film metals [184-186,199-201] and porous or nanocrystalline systems [85,86,154-156]. Methods related to IMPS include intensity modulated photovoltage spectroscopy (IMVS) [216-218] and light modulated microwave reflectance [219-222]. More recently Franco et al. [149] have developed photomodulated infrared transmittance spectroscopy (PITS).

The nature of the force which drives electron transport in nanoporous systems is not well understood, in principle it can be attributed either to migration or diffusion. To date there is no theory able to account for both forms of transport, and most of the work on electron transport in nanostructured films assumes that the driving force is diffusion. This is discussed in more detail in section 2.5.2. Here it suffices to say that in this work diffusion is considered to be the dominating form of transport. PEIS, IMPS, IMVS and PITS were used to investigate electron transport in dye-free and dye-sensitised TiO_2 nanocrystalline systems. It was found that trapping and detrapping have a major effect [149] on the electron transport in nanoparticulate films. A theoretical model with a single-trap was developed to take into account the effect of trapping and detrapping. However it proved to be inadequate in explaining some of the experimental results

obtained with frequency-resolved techniques. This suggests that a distribution of traps should be considered throughout the band-gap in order to achieve better agreement between theoretical and experimental results. Another limiting aspect of the modelling presented in this work is the fact that the parameters such as the diffusion coefficient and the electron lifetime are considered to be constant across the cell thickness. In fact, this may not be the case, particularly under short circuit conditions. Although the modelling requires further development to take account of the trapping/detrapping and the distance dependence of the parameters, the frequency-resolved techniques employed in the present work remain a powerful tool to investigate electron transport in nanoporous networks.

Other problems concerning dye-sensitised solar cells have recently attracted scientific interest. For example, is the back reaction of free electrons with the oxidised state of the dye a limiting factor for the efficiency of the cell? Do these porous films possess a uniform structure across their thickness? Does the dye adsorb uniformly onto the nanoporous TiO_2? All these questions remain only partially solved at present, and this work provides some answers within the framework of frequency-resolved techniques.

1.6 Conclusion

Electron transport in dye-free and dye-sensitised nanoparticulate TiO_2 has been investigated with IMPS, IMVS, PEIS and the novel technique of photomodulated infrared transmittance spectroscopy (PITS). The combination of all these frequency-resolved measurements provides a powerful tool to understand the functioning of these novel systems. In the other chapters IMPS, IMVS, PEIS and photomodulated infrared transmittance are introduced from both a theoretical and experimental point of view.

These experimental techniques applied to the porous systems give some useful answers to the problem of electron transport in nanocrystalline devices.

1.7 References

[1] B. O'Regan and M. Grätzel, Nature, 353, 737, (1991).

[2] J. K. Burdett, T. Hughbanks, G. J. Miller, J. W. Richardson and J. V. Smith, J. Am. Chem. Soc., 109, 3639, (1987).

[3] B. Silvi, N. Fourati, R. Nada, and C. R. A. Catlow, J. Phys. Chem. Solids, 52, 1005, (1991).

[4] K. M. Glassford and J. R. Chelikowski, Phys. Rev. B, 45, 3874, (1992).

[5] A. Fahmi, C. Minot, B. Silvi and M. Causà, Phys. Rev. B, 47, 11717, (1993).

[6] P. J. Hardman, G. N. Raikar, C. A. Muryn, G. van der Laan, P. L. Wincott, G. Thornton, D. W. Bullett and P. A. D. M. A. Dale, Phys. Rev. B, 49, 7170, (1994).

[7] R. Falckenberg, 'Crystal Growth: Theory and Techniques', C. H. L. Goodman, Ed., Plenum, New York, p. 177, (1978).

[8] T. E. Phillips, K. Morrjani, J. C. Murphy and T. O. Poehler, J. Electrochem. Soc., 129, 1210, (1982).

[9] H. Berger, H. Tang and F. Levy, J. Cryst. Growth, 130, 108, (1993).

[10] H. Tang, H. Berger, P. E. Schmid, F. Lèvy and G. Burri, Solid State Comm., 87, 847, (1993).

[11] H. Tang, H. Berger, P. E. Schmid and F. Lèvy, Solid State Comm., 92, 267, (1994).

[12] L. Forro, O. Chauvet, D. Emin, L. Zuppiroli, H. Berger and F. Lèvy, J. Appl. Phys., 75, 633, (1994).

[13] F. A. Grant, Rev. Mod. Phys., 31, 646, (1958).

[14] R. I. Bickley, Chem. Phys. Solids Surf., 7, 118, (1978).

[15] S. Kodaira, Y. Sakisaka, T. Maruyama, Y. Haruyama, Y. Aiura and H. Kato, Solid State Comm., 89, 9, (1994).

[16] F. Cao, G. Oskam, P. C. Searson, J. M. Stipkala, T. A. Heimer, F. Farzad and G. J. Meyer, J. Phys. Chem., 99, 11974, (1995).

[17] F. Urbach, Phys. Rev., 92, 1324, (1953).

[18] A. Henglein, Chem. Rev., 89, 1861, (1989).

[19] C. J. Brinker, D. E. Clark and D. R. Ulrich, Eds., 'Better Ceramics Thorough Chemistry II', Materials Research Society Symposium Proceedings, 73, (1986).

[20] C. J. Brinker, D. E. Clark and D. R. Ulrich, Eds., 'Better Ceramics Thorough Chemistry III', Materials Research Society Symposium Proceedings, 121, (1988).

[21] B. J. J. Zelinski, C. J. Brinker, D. E. Clark and D. R. Ulrich, Eds., 'Better Ceramics Through Chemistry IV', Materials Research Society Symposium Proceedings, 180, (1990).

[22] M. J. Hampden-Smiths, W. G. Klemperer and C. J. Brinker, Eds., 'Better Ceramics Through Chemistry V', Materials Research Society Symposium Proceedings, 271, (1992).

[23] A. K. Cheetham, C. J. Brinker, M. L. Mecartney and C. Sanchez, Eds., 'Better Ceramics Through Chemistry VI', Materials Research Society Symposium Proceedings, 346, (1994).

[24] S. Hotchandani and P. V. Kamat, J. Electrochem. Soc., 139, 1630, (1992).

[25] P. Höyer, R. Eichberger and H. Weller, Ber. Bunsenges. Phys. Chem., 97, 630, (1993).

[26] U. Björkstèn, Ph.D Thesis, 'On the Photo-electrochemisty of Nanocrystalline Porous Metaloxide Semiconducting Electrodes', EPF Lausanne, Switzerland, (1995).

[27] R. C. Faria and L. O. S. Bulhões, J. Electrochem., Soc., 141, L29, (1994).

[28] C. O. Avellaneda, M. A. Macêdo, A. O. Florenetino, D. A. B. Filho and M. A. Aergerter, SPIE, 2288, 422, (1994).

[29] A. Henglein, Top. Curr. Chem., 143, 113, (1988).

[30] L. Kavan, T. Stoto, M. Grätzel, D. Fitzmaurice and V. Shklover, J. Phys. Chem., 97, 9493, (1993).

[31] H. Yoneyama, Crit. Rev. Solid State Matter. Sci., 18, 69, (1993).

[32] A. Hagfeldt and M. Grätzel, Chem. Rev., 95, 45, (1995).

[33] G. Rothenberger, D. Fitzmaurice and M. Grätzel, J. Phys. Chem., 96, 5983, (1992).

[34] W. J. Macklin and R. J. Neat, Solid State Ionics, 694, 53, (1992).

[35] M. P Cantão, J. I. Cismeros and R. M. Torresi, J. Phys. Chem., 98, 4865, (1994).

[36] F. Bonino, L. Busani, M. Lazzari, M. Manstretta, B. Rivolta and B. Scrosatti, J. Power Sources, 6, 261, (1981).

[37] H. Lindström, S. Södergren, A. Solbrand, H. Rensmo, J. Hjelm, A. Hagfeldt and S.-E. Lindquist, J. Phys. Chem. B, 101, 7710, (1997).

[38] N. Vlachopoulos, P. Liska, J. Augustynski and M. Grätzel, J. Am. Chem. Soc., 110, 1216, (1988).

[39] R. Reisfeld and C. K. Jorgensen, Struct. Bond., 77, 207, (1992).

[40] L. C. Klein, Annu. Rev. Mater. Sci., 23, 437, (1993).

[41] R. C. Mehrotra, Struct. Bonding, 77, 1, (1992).

[42] K.-N. P. Kumar, J. Kumar and K. Keizer, J. Am. Ceram. Soc., 77, 1369, (1994).

[43] H. B. Clark, 'Treatise in Coatings', P. R. Myers and J. S. Long, Eds., Marcel-Dekker, New York, p. 479, (1977).

[44] D. Matthews, A. Kay and M. Grätzel, Aust. J. Chem., 47, 1869, (1994).

[45] D. Guyomard and J. M. Tarascon, J. Electrochem. Soc., 139, 937, (1992).

[46] C. G. Granqvist, Appl. Phys. A., 57, 19, (1993).

[47] S. Trasatti, 'Electrochemistry of Novel Materials', J. Lipkowski and P. N. Ross, Eds., VCH, Weinheim, Germany, p.207, (1994).

[48] C. Ravichandran, C. J. Kennedy, S. Chellammal, S. Thangavelu and P. N. Anantharaman, J. Appl. Electrochem., 21, 60, (1991).

[49] D. Vaseduvan, S. Chellammal and P. N. Anantharaman, J. Appl. Electrochem., 21, 839, (1991).

[50] K. Honda and A. Fujishima, Nature, 238, 37, (1972).

[51] P. V. Kamat, Chem. Rev., 93, 267, (1993).

[52] A. L. Linsebigler, G. Lu and J. T. Yates, Chem. Rev., 95, 735, (1995).

[53] S. N. Frank and A. J. Bard, J. Am. Chem. Soc., 99, 4667, (1997).

[54] R. N. Noufi, P. A. Kohl, S. N. Frank and A. J. Bard, J. Electrochem. Soc., 125, 246, (1978).

[55] Y. Hamasaki, S. Ohkubo, K. Murakami, H. Sei and G. Nogami, J. Electrochem. Soc., 141, 660, (1994).

[56] Y. Athanassov and M. Grätzel, unpublished results.

[57] Y. Takahashi, A. Ogiso, R. Tomoda, K. Sugiyama, H. Minoura and M. Tsuiki, J. Chem. Soc. Faraday Trans. I, 78, 2563, (1982).

[58] M. A. Rashti and D. E. Brodie, Thin Solid Films, 240, 163, (1994).

[59] A. Hageldt, N. Vlachopoulos, G. Gilbert and M. Grätzel, Proc. SPIE-Int. Soc. Opt. Eng., XIII. 2255, 297, (1994).

[60] A. Hagfeldt, L. Walder and M. Grätzel, Proc. SPIE-Int. Soc. Opt. Eng., XIV, 2531, 60, (1995).

[61] K. Itaya, K. Shibayama, H. Akahoshi and S. Toshima., J. Appl. Phys., 53, 804, (1982).

[62] D. W. DeBerry and A. Viehbeck, J. Electrochem. Soc., 130, 249, (1983).

[63] T. K. Lakshmanan, C. A. W. Wysocki and W. J. Slegesky, IEEE Comp. Parts,

CP-11 (2), 14, (1964).

[64] M. Mayor, A. Hagfeldt, M. Grätzel and L. Walder, Chimia, 50, 47, (1996).

[65] M. J. Cook, A. P. Lewis, G. S. G. McAuliffe, V. Skarda, A. J. Thomson, J. L. Glasper and D. J. Robbins, J. Chem. Soc. Perkin Trans., 2, 1293, (1984).

[66] M. J. Cook and A. J. Thomson, Chem. Ber., 20, 914, (1984).

[67] P. C. Alford, M. J. Crook, A. P. Lewis, G. S. G. McAuliffe, V. Skarda, A. J. Thomson, J. L. Glasper and D. J. Robbins, J. Chem. Soc. Perkin. Trans., 2, 705, (1985).

[68] J. Janata, Anal. Chem., 62, 33R, (1990).

[69] J. Janata, Anal. Chem., 64, 196R, (1992).

[70] K. Bucher and Fricke, J. Phys. Zeit, 21, 237, (1980).

[71] K. Honda and A. Fujishima, Nature, 238, 37, (1972).

[72] B. J. Tufts, I. L. Abrahams, P. G. Santangelo, G. N. Ryba, L. G. Casagrande and N. S. Lewis, Nature, 326, 681, (1987).

[73] S. Licht, G. Hodes, R. Tenne and J. Manassen, Nature, 326, 863, (1987).

[74] A. J. Nozik, Phil. Trans. R. Soc. Lond., A295, 453, (1980).

[75] H. Tributsch and J. C. Bennet, J. Electroanal. Chem., 81, 97, (1977).

[76] R. Memming, Philos. Tech. Rev., 38, 160, (1979).

[77] M. S. Wrighton, Acc. Chem. Res., 12, 303, (1979).

[78] A. Heller, Acc. Chem. Res., 14, 154, (1981).

[79] H. Gerischer, Electrochim. Acta, 35, 1677, (1990).

[80] A. J. Bard, Science, 207, 139, (1980).

[81] R. Matsumura, Y. Nomura and H. Tsubomura, Bull. Chem. Soc. Japan, 50, 2533, (1977).

[82] N. Alonso, V. M. Beley, P. Chartier and V. Ern, Rev. Phys. Appl., 16, 5, (1977).

[83] F. Willig, R. Eichberger, N. S. Sundaresan and B. A. Parkinson, J. Am. Chem. Soc., 112, 2701, (1990).

[84] A. Solbrand, H. Lindström, H. Rensmo, A. Hagfeldt, S. E. Linquist and S. Södergen, J. Phys. Chem. B, 101, 2514, (1997).

[85] F. Cao, G. Oskam, G. J. Meyer and P. C. Searson, J. Phys. Chem., 100, 17021, (1996).

[86] L. Dloczik, O. Ileperuma, I. Lauermann, L. M. Peter, E. A. Ponomarev, G. Redmond, N. J. Shaw and I. Uhlendorf, J. Phys. Chem. B, 101, 10281, (1997).

[87] Y. Tachibana, J. E. Moser, M. Grätzel, M. Klug and D. R. Durrant, J. Phys. Chem. 100, 20056, (1996).

[88] T. Hannappel, B. Burfeindt, W. Storck and F. Willig, J. Phys. Chem. B, 101, 6799, (1997).

[89] S. A. Haque, Y. Tachibana, D. R. Klug and J. R. Durrant, J. Phys. Chem. B, 102, 1745, (1998).

[90] G. Schlichthörl, S. Y. Huang, J. Sprague and A. J. Frank, J. Phys. Chem. B, 101, 8141, (1997).

[91] S. Y. Huang, G. Schlichthörl, A. J. Nozik, M. Grätzel and A. J. Frank, J. Phys. Chem. B, 101, 2576, (1997).

[92] D. J. Fritzmaurice and H. Frei, Langmuir, 7, 1129, (1991).

[93] D. J. Fritzmaurice, M. Eschle and H. Frei, J. Phys. Chem., 97, 3806, (1993).

[94] A. Stanley and D. Matthews, Aust. J. Phys. Chem., 48, 1294, (1995).

[95] P. V. Kamat and M. A. Fox, Chem. Phys. Lett., 102, 379, (1983).

[96] J. Moser and M. Grätzel, J. Am. Chem. Soc., 106, 6557, (1984).

[97] R. Rossetti and L. E. Brus, J. Am. Chem. Soc., 106, 4336, (1984).

[98] M. A. Ryan, E. C. Fitzgerald and M. T. Spitler, J. Phys. Chem., 93, 6150, (1989).

[99] V. Heleg and I. Willner, J. Chem. Soc. Chem. Commun., 2113, (1994).

[100] S. Umapathy, A. M. Cartner, A. W. Parker and R. E. Hester, J. Phys. Chem., 94, 8880, (1990).

[101] K. R. Gopidas and P. V. Kamat, J. Phys. Chem., 93, 6428, (1989).

[102] R. E. Fessenden and P. V. Kamat, Chem. Phys. Lett., 123, 233, (1986).

[103] T. Takizawa, T. Watanabe and K. Honda, J. Phys. Chem., 82, 1391, (1978).

[104] K. Hashimoto, M. Hiramoto and T. Sakata, Chem. Phys. Lett., 148, 215, (1988).

[105] K. Hashimoto, M. Hiramoto and T. Sakata, J. Phys. Chem., 92, 4272, (1988).

[106] Y. Liang, P. F. Moy, J. A. Poole and A. M. Ponte Goncalves, J. Phys. Chem., 88, 2451, (1984).

[107] K. Bitterling and F. Willig, J. Electroanal. Chem. Interfacial Electrochem., 204, 211, (1986).

[108] R. L. Crackel and W. S. Struve, Chem. Phys. Lett., 120, 473, (1985).

[109] F. Willig, R. Eichberger, N. S. Sundaresan and B. A. Parkinson, J. Am. Chem. Soc., 112, 2701, (1990).

[110] R. Eichberger and F. Willig, Chem. Phys. Lett., 141, 159, (1990).

[111] B. Patrick and P. V. Kamat, J. Phys. Chem., 96, 1423, (1992).

[112] P. V. Kamat, J. P. Chauvet and R. W. Fessenden, J. Phys. Chem., 90, 1389, (1986).

[113] A. Kay, R. Humphry-Baker and M. Grätzel, J. Phys. Chem., 98, 952, (1994).

[114] P. V. Kamat, J. Phys. Chem., 93, 859, (1989).

[115] V. H. Houlding and M. Grätzel, J. Am. Chem. Soc., 105, 5695, (1983).

[116] K. Kalyanasundaram, N. Vlachopoulos, V. Krishnan, A. Monnier and M. Grätzel, J. Phys. Chem., 91, 2342, (1987).

[117] C. Arbour, D. K. Sharma and C. H. Langford, J. Phys. Chem., 94, 331, (1990).

[118] F. R. F. Fan and A. J. Bard, J. Am. Chem. Soc., 101, 6139, (1979).

[119] E. Vrachnou, N. Vlachopoulos and M. Grätzel, J. Chem. Soc. Chem. Commun., 12, 868, (1987).

[120] E. Vrachnou, M. Grätzel and A. J. McEvoy, J. Electroanal. Chem. Interfacial

Electrochem., 258, 193, (1989).

[121] Y. I. Kim, S. J. Atherton, E. S. Brigham and T. E. Mallouk, J. Phys. Chem., 97, 11802, (1993).

[122] I. Bedja, S. Hotchandani and P. V. Kamat, J. Phys. Chem., 98, 4133, (1994).

[123] I. Willner, Y. Eichen, A. J. Frank and M. A. Fox, J. Phys. Chem., 97, 7264, (1993).

[124] K. M. M. Taqui, D. Chatterjee, A. Hussain and M. A. Moiz, J. Photochem. Photobiol. A, 76, 97, (1993).

[125] P. K. Ghosh and T. G. Spiro, J. Am. Chem. Soc., 102, 5543, (1980).

[126] D. A. Gulino and H. G. Drickamer, J. Phys. Chem., 88, 1173, (1984).

[127] R. Dabestani, A. J. Bard, A. Campion, M. A. Fox, T. E. Mallouk, S. E. Webber and J. M. White, J. Phys. Chem., 92, 1872, (1988).

[128] M. K. Nazeeruddin, P. Liska, J. Moser, N. Vlachopoulos and M. Grätzel, Helv. Chim. Acta, 73, 1788, (1990).

[129] B. O'Regan, J. Moser, M. Anderson and M. Grätzel, J. Phys. Chem., 94, 8720, (1990).

[130] W. E. Ford and M. A. J. Rodgers, J. Phys. Chem., 98, 3822, (1994).

[131] M. A. Ryan and M. T. Spitler, J. Imaging Sci., 33, 46, (1989).

[132] T. Iwasaki, S. Oda, H. Kamada and K. Honda, J. Phys. Chem., 84, 1060, (1980).

[133] H. Hada, Y. Yonezawa and H. Inaba, Ber. Bunseges. Phys. Chem., 85, 425, (1981).

[134] C. Kavassalls and M. T. Spitler, J. Phys. Chem., 87, 3166, (1983).

[135] L. M. Natoli, M. A. Ryan and M. T. Spitler, J. Phys. Chem., 89, 1448, (1985).

[136] Y. Hayashi, S. Ogawa, M. Sanada and R. Hirohashi, J. Imaging. Sci., 33, 124, (1989).

[137] T. Tani, T. Suzumoto and K. Ohzeki, J. Phys. Chem., 94, 1298, (1990).

[138] R. Kietzmann, A. Ehret, M. Spitler and F. Willig, J. Am. Chem. Soc., 115, 1930, (1993).

[139] C. Nasr, S. Hotchandani, P. V. Kamat, S. Das, K. George Thomas and M. V. George, Langmuir, 11, 1777 (1995).

[140] P. V. Kamat, K. R. Gopidas and N. M. Dimitrijevic, Mol. Cryst. Liq. Cryst., 183, 439,4 (1990).

[141] S. Hotchandani, S. Das, K. G. Thomas, M. V. George and P. V. Kamat, Res. Chem. Intermed., 20, 927, (1994).

[142] Y.-S. Kim, K. Liang, K.-Y. Law and D. G. Whitten, J. Phys. Chem., 98, 984, (1994).

[143] H. Frei, D. J. Fitzmaurice and M. Grätzel, Langmuir, 6, 198, (1990).

[144] B. O' Regan, J. Moser, M. Anderson, and M. Grätzel, J. Phys. Chem., 94, 8720, (1990).

[145] M. K. Nazeeruddin, A. Kay, I. Rodicio, R. Humphry-Baker, E. Müller, P. Liska, N. Vlachopoulos and M. Grätzel, J. Am. Chem. Soc., 115, 6382, (1993).

[146] P. Péchy, F. P. Rotzinger, M. K. Nazeeruddin, O. Kohle, S. M. Zakeeruddin, R. Humphry-Baker and M Grätzel, J. Chem. Soc. Chem. Commun., 65, (1995).

[147] L. M. Peter and D. Vanmaekelbergh, Adv. Electrochem. Sci. and Eng., Ed., R. C. Alkire and D. M. Kolb, 6, 77, (1999).

[148] S. Södergren, A. Hagfeldt, J. Olsson and S.-E. Lindquist, J. Phys. Chem., 98, 5552, (1994).

[149] G. Franco, J. Gehring, L. M. Peter, E. A. Ponomarev and I. Uhlendorf, J. Phys. Chem. B, 103, 692, (1999).

[150] C. J. Barbé, F. Arendse, P. Comte, M. Jirousek, F. Lenzmann, V. Shklover and M. Grätzel, J. Am. Ceram. Soc., 80, 3157, (1997).

[151] G. Hodes, I. D. Howell and L. M. Peter, J. Electrochem. Soc., 139, 3136, (1992).

[152] S. Hotchandani and P. V. Kamat, J. Electrochem. Soc., 139, 1630, (1992).

[153] P. Hoyer and H. Weller, J. Phys. Chem., 99, 14096, (1995).

[154] D. Vanmaekelbergh, F. Iranzo Marín and J. van de Lagemaat, Ber. Bunsenges. Phys. Chem., 100, 616, (1996).

[155] P. E. de Jongh and D. Vanmaekelbergh, Phys. Rev. Lett., 77, 3427, (1996).

[156] P. E. de Jongh and D. Vanmaekelbergh, J. Phys. Chem. B, 101, 2716, (1997).

[157] D. D. MacDonald 'Transient Techniques in Electrochemistry', Plenum, New York, (1977).

[158] G. Gabrielli, 'Identification of elecrochemical processes by frequency response analysis', Technical report No 004/83. Solatron Instrument, UK, (1980).

[159] J. R. Macdonald (Editor), 'Impedance Spectroscopy emphasising solid materials and systems', Wiley, New York, (1987).

[160] P. Allongue and H. Cachet, J. Electroanal. Chem., 119, 371, (1981).

[161] J. Schefold and H. M. Kühne, J. Electroanal. Chem., 300, 211, (1991).

[162] F. Cardon and D. Vanmaekelbergh, Electrochim. Acta, 37, 837, (1992).

[163] J. Schefold, J. Electrochem. Soc., 142, 850, (1995).

[164] W. P. Gomes and D. Vanmaekelbergh, Electrocim. Acta, 41, 967, (1996).

[165] E. A. Ponomarev and L. M. Peter, J. Electroanal. Chem., 397, 45, (1995).

[166] W. J. Albery and P. N. Bartlett, J. Electrochem. Soc., 129, 2254, (1982).

[167] J. Li and L. M. Peter, J. Electroanal. Chem., 193, 27, (1985).

[168] J. Li and L. M Peter, J. Electroanal. Chem., 199, 1, (1986).

[169] L. M. Peter, 'Trends in Interfacial Electrochemistry', p. 523. Editor F. A. Silva. Reidel, Dordrecht (1986).

[170] R. Peat and L. M. Peter, Electrochim. Acta, 31, 731, (1986).

[171] R. Peat and L. M. Peter, J. Electroanal. Chem., 209, 307, (1986).

[172] R. Peat and L. M. Peter, Ber. Bunsenges. Phys. Chem., 91, 382, (1987).

[173] R. Peat and L. M. Peter, J. Electroanal. Chem., 228, 351, (1987).

[174] R. Peat and L. M. Peter, Appl. Phys. Lett., 51, 328, (1987).

[175] L. M. Peter, 'Photocatalysis and the Environment'. p. 275. Editor M. Schiavello, Kluwer, Dordrecht, (1987).

[176] H-J. Lewerenz, J. Stumper and L. M. Peter, Phys. Rev. Lett., 61, 1989, (1988).

[177] L. M. Peter, J. Li, R. Peat, H.J. Lewerenz and J. Stumper, Electrochim. Acta, 35, 1657, (1990).

[178] L. M. Peter, Chem. Rev., 90, 753, (1990).

[179] L. M. Peter, A. N. Borazio, H. J. Lewerenz and J. Stumper, J. Electroanal. Chem., 290, 229, (1990).

[180] L. M. Peter, Croat. Chem. Acta, 63, 401, (1990).

[181] B. P. Minks, N. A. M. Verhaegh, J. J. Kelly, J. Stumper and L. M. Peter, J. Electroanal. Chem., 303, 277, (1991).

[182] P. Herrasti and L. M. Peter, J. Electroanal. Chem., 305, 241, (1991).

[183] H. K. Song and D. D Macdonald, J. Electrochem. Soc., 138, 1408, (1991).

[184] Z. A. Rotenberg and O. A. Semenikhin, J. Electroanal. Chem., 316, 165, (1991).

[185] O. A. Semenikhin, Z. A. Rotenberg and A. G. Pschenichnikov, Soviet Electrochemistry, 27, 317, (1991).

[186] O. A. Semenikhin, Z. A. Rotenberg and G. L. Teplitskaya, Soviet Electrochemistry, 27, 190, (1991).

[187] J. J. Kelly, B. P. Minks, N. A. M. Verhaegh, J. Stumper and L. M. Peter, Electrochim. Acta, 37, 877, (1992).

[188] R. S. Hutton and L. M. Peter, J. Electroanal. Chem., 332, 315, (1992).

[189] P. Herrasti and L. M. Peter, J. Electroanal. Chem., 334, 133, (1992).

[190] J. Schefold, J. Electroanal. Chem., 341, 111, (1992).

[191] P. C. Searson, D. D. MacDonald and L. M. Peter, J. Electrochem. Soc., 139,

2538, (1992).

[192] A. R. de Wit, D. Vanmaekelbergh and J. J. Kelly, J. Electrochem. Soc., 139, 2508, (1992).

[193] Z. A. Rotenberg, Soviet Electrochemistry, 28, 1317, (1992).

[194] D. Vanmaekelbergh, A. R. de Wit and F. Cardon, J. Appl. Phys., 73, 5049, (1993).

[195] B. H. Erné, D. Vanmaekelbergh and I. E. Vermeir, Electrochim. Acta, 38, 2559, (1993).

[196] I. E. Vermeir, W. P. Gomes, B. H. Erné and D. Vanmaekelbergh, Electrochim. Acta, 38, 2659, (1993).

[197] A. M. Chaparro, P. Salvador, A. Tabernero, R. Navarro, B. Coll and V. Caselles, Surf. Sci., 295, 457, (1993).

[198] P .C. Searson and D. D. Macdonald, Electrochim. Acta, 38, 1913, (1993).

[199] A. Goossens and D. D Macdonald, J. Electroanal. Chem., 352, 65, (1993).

[200] A. Goossens and D. D. Macdonald, Electrochim. Acta, 38, 1965, (1993).

[201] A. D. Modestov, G. D. Zhou, H. H. Ge and B. H Loo, J. Electroanal. Chem., 375, 293, (1994).

[202] R. S. Hutton and D. E. Williams, Electrochim. Acta, 39, 701, (1994).

[203] G. Schlichthörl, E. A. Ponornarev and L. M. Peter, J. Electrochem. Soc., 142, 3062, (1995).

[204] E. A. Ponomarev and L. M. Peter, J. Electroanal. Chem., 396, 209, (1995).

[205] J. Schefold, J. Electroanal. Chem., 394, 35, (1995).

[206] A. M. Chaparro, P. Salvador and L. M. Peter, J. Phys. Chem., 99, 6677, (1995).

[207] G. H. Schoenrnakers, D. Vamnaekelbergh and J. J. Kelly, J. Phys. Chem., 100, 3215, (1996).

[208] A. Goossens, Surf. Sci., 365, 662, (1996).

[209] G. Oskarn, J. C. Schmidt and P. C. Searson, J. Electrochem. Soc., 142, 2538, (1996).

[210] E. A. Meulenkamp and A. R. deWit, Electrochim. Acta, 41, 109, (1996).

[211] D. J. Fermín, E. A. Ponomarev and L. M. Peter, J. Electroanal. Chem, 401, 207, (1996).

[212] E. A. Ponomarev, R. Tenne, A. Katty and C. Levy-Clement, Sol. Energy Mat. and Sol. Cells, 52, 125, (1998).

[213] D. Vamnaekelbergh, J. van de Lagemaat, P. E. I. Schopp and F. Cardon, Phil. Mag. B-Phys. Cond. Matter Stat. Mec. Elec. Opt. Magn. Properties, 79, 291, (1999).

[214] G. H. Schoenmakers, D. Vanmaekelbergh and J. J. Kelly, J. Chem. Soc. Faraday Trans., 93, 1127, (1997).

[215] L. M. Peter, E. A. Ponomarev and D. J. Fermín, J. Electroanal. Chem., 427, 79, (1997).

[216] E. Kamieniecki, J. Vac. Sci. Technol., 20, 811, (1982).

[217] E. Kamieniecki, J. Appl. Phys., 54, 6481, (1983).

[218] G. Schlichthörl and H. Tributsch, Electrochim. Acta, 37, 919, (1992).

[219] G. Schlichthörl, E. A. Ponomarev and L M. Peter, J. Electrochem. Soc., 142, 3062, (1995).

[220] H. Tributsch, G. Schlichthörl and L. Elstner, Electrochim. Acta, 38, 141, (1993).

[221] H. J. Lewerenz and G. Schlichthörl, J. Appl. Phys., 75, 3544, (1994).

[222] F. Wunsch, Y. Nakato, M. Kunst and H. Tributsch, J. Chem. Soc. Faraday Trans., 92, 4053, (1996).

CHAPTER II

PHOTOELECTROCHEMISTRY

2.1 Introduction

All photoelectrochemical systems have in common the fact that they involve electron transfer induced by light absorption. In the 1980s there was great interest in photoelectrochemistry, and it was demonstrated that semiconductor/electrolyte junctions could be used for solar energy conversion [1-10]. However problems like stability and cost prevented practical large-scale implementation of these devices. Consequently there was a decline of interest in photoelectrochemistry at the end of the 1980s. A few years later the Swiss scientist Michael Grätzel [11] used dye-sensitized porous TiO_2 electrodes instead of flat electrodes to achieve monochromatic photocurrent quantum yields as high as 90%. This breakthrough revitalized interest in photoelectrochemistry and stimulated studies of the fundamental properties of nanocrystalline semiconductor electrodes.

This chapter reviews the fundaments of flat and porous semiconductor/electrolyte junctions in the dark and under illumination. Porous electrodes have attracted great scientific interest because of their high surface area to volume ratio. In these porous electrodes, formed by interconnected nanoparticles, the mechanism of electron transport is an issue at present [12-14]. In the present work electron transport is assumed to occur by diffusion, the basis for this assumption is discussed at the end of this chapter.

2.2 Semiconductors and Electrolytes

The Fermi energy describes the distribution of holes and electrons in the available energy levels of a solid. To a first approximation, all states below the Fermi energy are occupied and the ones above empty. A more detailed description of the Fermi level is given by the Fermi-Dirac probability distribution function, $f(E)$, which expresses the probability that a level at energy E is occupied by an electron. The Fermi-Dirac probability distribution function is given by:

$$f(E) = \frac{1}{1 + e^{(E-E_F)/kT}} \tag{2.1}$$

here E_F is the Fermi level, whose probability of being occupied is 50%, k is the Boltzmann constant and T is the absolute temperature.

The position of the Fermi level relative to the bands of a solid distinguishes a metal from a semiconductor or an insulator. For example, if the Fermi energy is in a region of the band with a very high density of states, then the material is a metal. For a metal all the energy levels below E_F are occupied and the ones above are empty. On the other hand, if the Fermi level is in a forbidden region of the band, the material is either a semiconductor or an insulator. The forbidden region for most semiconductors is of the order of at least 1 eV. The bottom edge of the band-gap is called the valence band and the top edge conduction band. For an intrinsic semiconductor, the Fermi level is in the middle of the forbidden band-gap. For an *n*-type semiconductor, the Fermi level is just below the conduction band and for a *p*-type semiconductor is just above the valence band as shown in **Figure 2.1**.

A *degenerate semiconductor* is a material that would normally be considered a semiconductor but is quasi-metallic because large densities of electrons have been added to the conduction band or large densities of holes to the valence band. A degenerate semiconductor is defined as one where the Fermi energy has been moved into the band-either valence or conduction band. Such addition of electrons and holes is

achieved by very heavy doping with donors or acceptors, respectively.

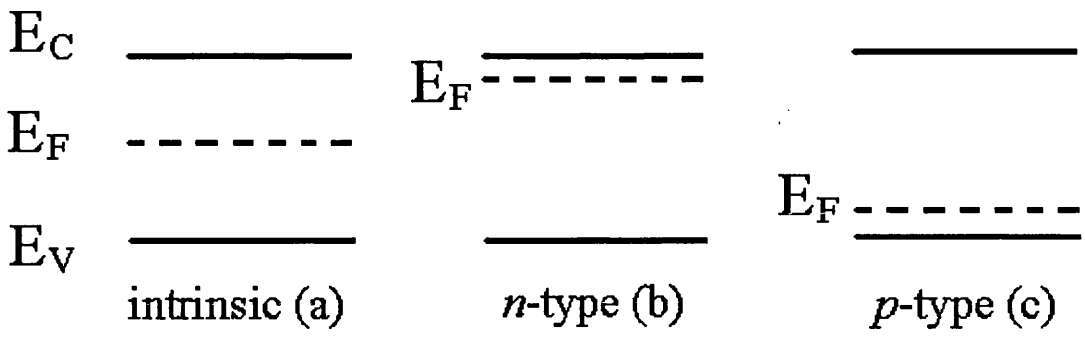

Figure 2.1. Energy diagrams of an intrinsic (a), *n*-doped (b), *p*-doped (c) semiconductor.

For a non-degenerate semiconductor, the concentration of electrons in the conduction band is given by:

$$\frac{n}{N_C} = e^{-(E_C - E_F)/kT} \tag{2.2}$$

The concentration of holes in the valence band is given by:

$$\frac{p}{N_V} = e^{-(E_F - E_V)/kT} \tag{2.3}$$

Here N_C and N_V are respectively the total number of states in the conduction band and in the valence band respectively.

The Fermi level describes the occupation of energy levels at thermodynamic equilibrium, but an important case in semiconductor electrochemistry is when thermodynamic equilibrium is not attained. Illumination of the sample by photons of energy greater than the band-gap is an important example and it is discussed in section 2.4.2.

When a semiconductor and a redox couple in solution are brought together, it can be shown that the Fermi level of the semiconductor is given by:

$$E_F = qE_A - \frac{kT}{n} ln\left(\frac{O}{R}\right) - q\phi_{sol} \tag{2.4}$$

where E_A (in volts) is a property of the redox couple *R/O* and describes the tendency to inject or extract electron from the material, *O* and *R* are the respective concentrations of the oxidizing and reducing species and ϕ_{sol} is the potential of the solution. It is important to define a reference potential in order to use equation (2.4). The hydrogen couple is normally chosen as the reference system, with corresponding Fermi energy equal to –4.5eV with respect to the energy of an electron at infinity. If the couple being tested tends to inject electrons into the electrode more than the hydrogen couple under standard conditions, the redox couple potential is negative. On the other hand, if the hydrogen couple tends to inject more electrons, then the redox potential of the couple is positive. Equation (2.4) then becomes:

$$E_F = -qE^0 - \frac{kT}{n} ln\left(\frac{O}{R}\right) \tag{2.5}$$

here E_F is the Fermi energy of the electrode in contact with the redox couple *R/O*, and E^0 is the 'standard redox potential' of the redox couple *R/O*. The parameter E^0 is tabulated as the potential measured relative to the hydrogen reference electrode when the specified redox couple of interest is present at unit concentration.

Equilibrium between the electrode and the redox couple is reached when the Fermi energy of the electrode moves to the energy E_{redox} due to electron exchange with the redox couple. Thus E_{redox} is defined to be equal to E_F at equilibrium:

$$E_{redox}=E_F \tag{2.6}$$

E_{redox} is a property of the solution and it can only be measured by its influence on the electrode. A case of particular interest is when there are equal concentrations of the oxidizing and reducing species, in which case the symbol E^0_{redox} is used. E_{redox} and E^0_{redox} are related using equation (2.5) and (2.6), by:

$$E_{redox} = E^{0}_{redox} - \frac{kT}{n} ln\left(\frac{O}{R}\right) \tag{2.7}$$

It can be shown that at equilibrium E_{redox} is given by:

$$E_{redox} = \frac{1}{2}(E_{ox} + E_{red}) \tag{2.8}$$

here E_{ox} and E_{red} are respectively the energy of the reduced and oxidized agent in solution.

For an *n*-type semiconductor, if E_F lies above E_{redox}, electrons will flow from the semiconductor (which becomes positively charged) into the solution phase (which becomes negatively charged). This situation is referred to as *depletion*. This means that the surface region is depleted of majority carriers, and as minority carriers are not present, the surface is depleted of both forms of mobile carriers. On the other hand, if E_F lies below E_{redox}, electrons will flow from the solution (which becomes positively charged) into the semiconductor (which becomes negatively charged). This situation is known as *accumulation*. The excess of charge in the semiconductor is distributed in a *space charge* region. The electric field in the space charge region results in a bending of the energy bands. The bands are bent upwards (depletion) when the semiconductor space charge is positive (i.e. ionized donor states). An excess electron in the space charge region will thus move toward the bulk semiconductor in the direction consistent with the existing electric field. An excess hole in the space charge region will move toward the interface. The bands are instead bent downwards in accumulation, this means that an excess electron in the space charge region moves toward the surface and an excess hole moves toward the bulk semiconductor. In this case the accumulation layer is very thin compared with the depletion layer. This is due to the fact that electrons are mobile, whereas the donors ions are fixed in the lattice.

2.3 The Double Layer

Charged planes and space charge regions form at interfaces. For example, if charges of positive sign form at the interface they will attract charges of opposite sign in the adjacent phase, hence double layers form. In between the double layers there will then be very high electric fields. At a solid/liquid interface three double layers can be distinguished: the space charge, the Helmholtz and the Gouy-Chapman double layer [15].

For example, for an *n*-type semiconductor in depletion, the space charge double layer is given by the positive charge which forms in the depletion region balanced by counter ions in solution. The Helmholtz double layer is instead the charge in between the surface of the semiconductor and the outer Helmholtz plane (ohp), which is the plane nearest to the surface of non-adsorbed species. Finally the Gouy-Chapman double layer is formed between the ohp and the bulk solution.

The Gouy-Chapman double layer is formed when the charge on the ohp is not enough to compensate the charge on the electrode, hence charge of opposite sign to the charge on the electrode extend into the solution. If the solution is very concentrated, the Gouy-Chapman double layer is very thin and essentially it can be considered melded into the outer Helmholtz plane. It follows that for very concentrated solution the Gouy-Chapman double layer can be neglected.

The Helmholtz double layer is formed in between two planar sheets, one is the surface of the electrode and the other is the outer Helmholtz layer. The distance in between the two sheets is of molecular size, as shown in **Figure 2.2**, and the corresponding capacitance is high compared with the one of the space charge region. The potential drop across the Helmholtz double layer, V_H, plays an important role in the electrochemistry of solid/electrolyte junctions. On the solution side the charge originates by the accumulation of ions at the ohp. The charge on the solid side of the

Helmholtz double layer can be of three different forms depending on the type of material: accumulation of free electronic charges, electronic charge trapped at surface states and finally ionic charge associated with adsorption at surface termination.

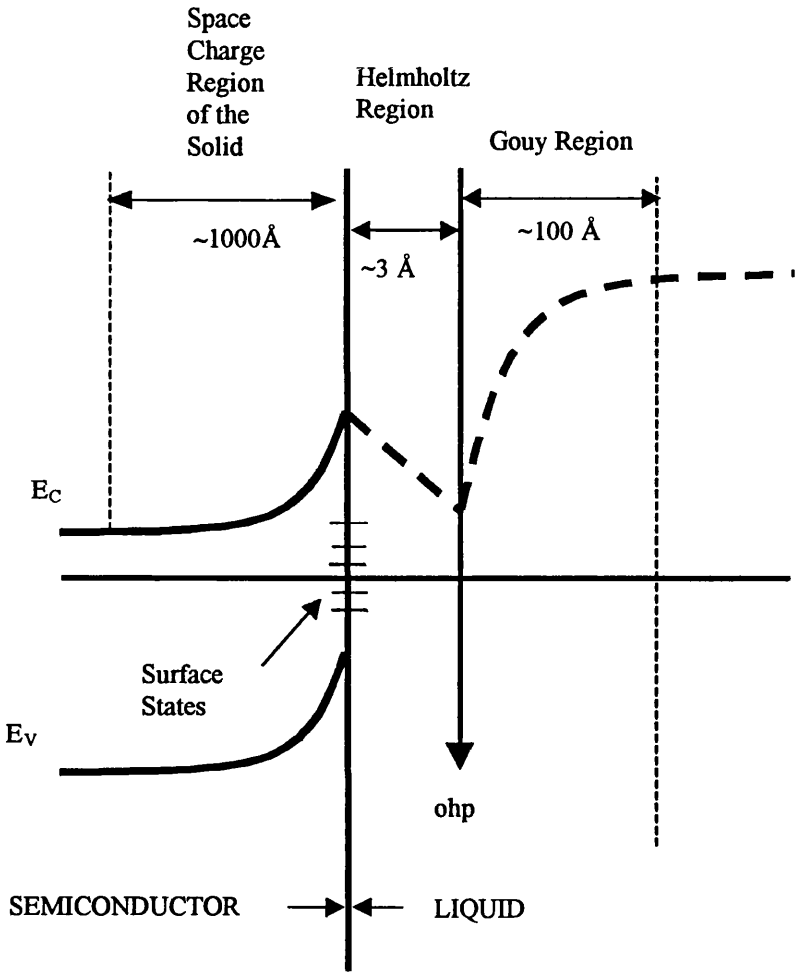

Figure 2.2. Double layers at the solid/liquid interface. The dashed line through the liquid indicates the variation in potential energy of a unit negative charge as it moves from the conduction band of the solid into the solution. The Gouy layer thickness indicated would represent a very dilute solution.

If the solid is an insulator, the charge on the solid side of the Helmholtz double layer cannot be free charge, it is therefore adsorbed ions or dipoles. At equilibrium the Helmholtz double layer adjust itself so that the rate of adsorption equals the rate of desorption of ions. For aqueous solvents, it can be shown that the Helmholtz potential

decreases of about 60mV per pH unit [16,17].

If the material is a metal immersed in a solution containing a redox couple the charge on the solid side of the Helmholtz double layer is mostly due to free electrons in levels near the Fermi level at the surface. When a metal/liquid interface is formed, depending on the position of the energy of the redox couple and the Fermi level of the metal, electrons will, for example, flow from the electrolyte into the metal in order to establish equilibrium. At equilibrium, the rate of electron transfer in and out of the metal is equal. The negative charge formed on the metal surface is compensated by ions in solution, thus the electrical field, V_H, will be formed across the interface. Any change in the applied bias will appear across the Helmholtz double layer; thus a cathodic current from the metal to the solution will flow for negative bias.

For a semiconductor, the voltage across the Helmholtz double layer can be controlled by both adsorption/desorption [18,19] and charge transfer. For a non-degenerate semiconductor in depletion at the solid/liquid interface there are no mobile carriers, and the surface region is essentially insulting. Therefore the adsorption/desorption process controls the potential distribution at the surface and any applied voltage appears in the space charge region leaving V_H unchanged. On the other hand, if the semiconductor is under strong accumulation conditions (as shown in **Figure 2.3**), i.e. the Fermi level crosses the conduction band, metallic [20] behavior is observed at the surface. Consequently, any applied bias appears at the Helmholtz double layer and no longer in the space charge region. In other words the semiconductor becomes degenerate and its energy bands are no longer pinned at the surface.

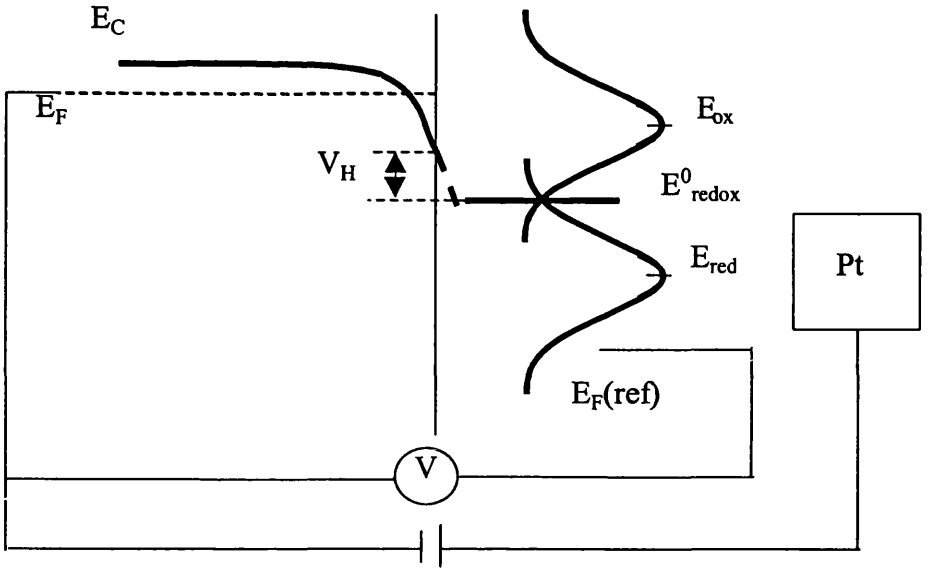

Figure 2.3. Schematic diagram of the degeneracy of a semiconductor due to strong cathodic bias. The voltage appears across the Helmholtz layer causing quasi-metallic behavior.

2.4 Flat Electrodes

2.4.1 Semiconductor/Electrolyte Interface in the Dark

The thickness of the Helmholtz is considerably smaller than the space charge region, so that the potential drop across the space charge region, $\Delta\phi_{SC}$, occurs over a larger distance than V_H. This is due to the fact that $\Delta\phi_{SC}$ arises from the ionization of donors in the solid, whilst V_H is given by the ions accumulated a few Angstroms away from the surface as illustrated in **Figure 2.4**. As the capacitances of the Helmholtz double layer and the space charge region appear to be in series, and given that the Helmholtz capacitance is normally much larger than the space charge capacitance, the former can be neglected under depletion conditions. It follows that any externally applied bias appears only in the space charge region, modifying the band bending profile. The potential at which the concentration of electrons at the surface is the same as in the bulk is called *flat band potential* (**Figure 2.5**). Therefore any change in the applied potential between the reference and the working electrode can be written:

$$U=\Delta\phi_{SC}+U_{fb} \tag{2.9}$$

At potentials more positive than U_{fb} the surface concentration of electrons is decreased producing a *depletion layer*. On the other hand, at potentials more negative than U_{fb} electrons generate an *accumulation layer*, bending the bands to lower energies.

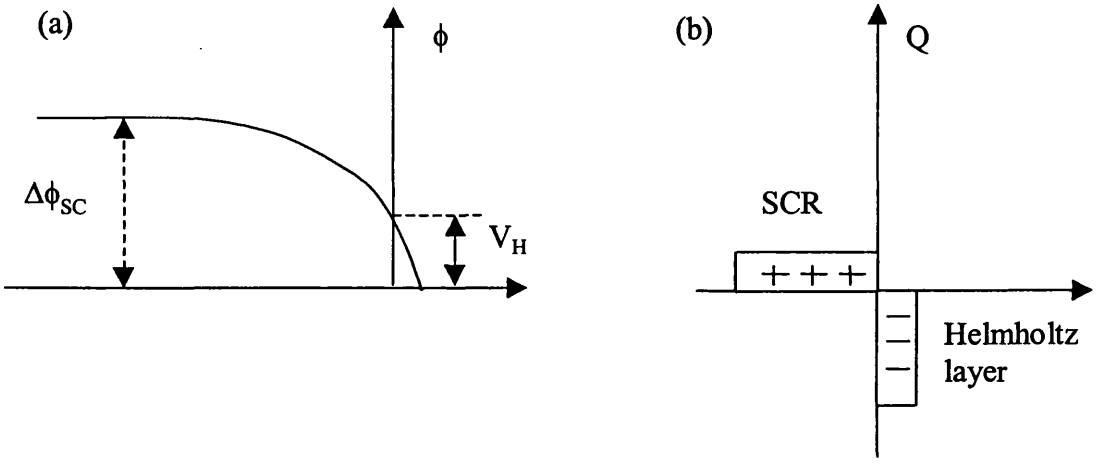

Figure 2.4. Schematic representation of the potential drop (a) and charge (b) across the semiconductor electrolyte interface under depletion conditions.

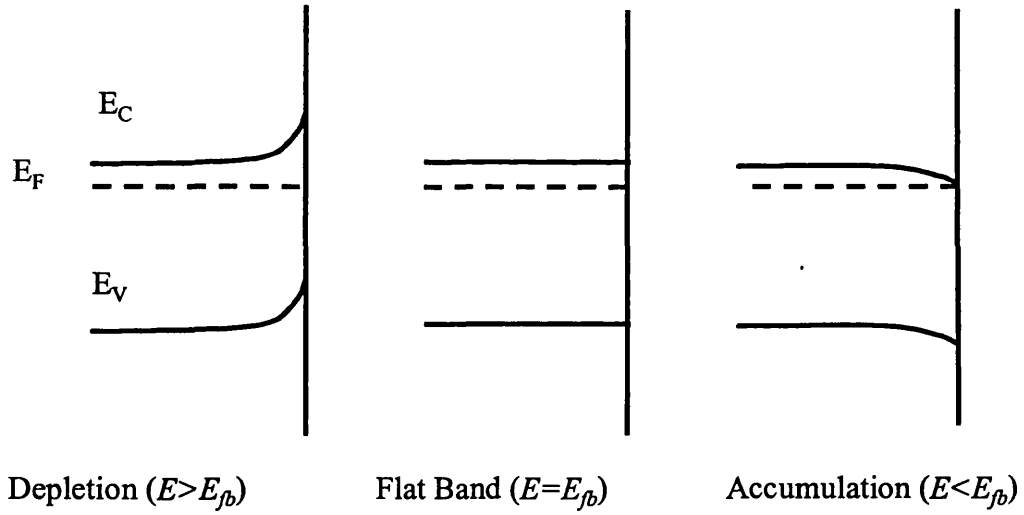

Figure 2.5. Potential dependence of the band bending for an *n*-type semiconductor.

From Poisson's equation, and applying the Fermi-Dirac statistics for free electrons, it is found that the width of the space charge region, d_{SC}, and the potential drop between the surface and the bulk of the semiconductor, $\Delta\phi_{SC}$, are related by:

$$\Delta\phi_{sc}=(qN_d/2\varepsilon\varepsilon_0)d_{sc}^2 \quad (2.10)$$

here N_d is the electron donor concentration and ε is the relative permittivity of the solid. It follows that the capacitance of the space charge, C_{sc} can be calculated from:

$$C_{sc}=\varepsilon\varepsilon_0/d_{sc} \quad (2.11)$$

For densities of free carriers between 10^{15} and 10^{19} cm^{-3}, C_{sc} ranges from 10^{-9} to 10^{-7}F cm^{-2} for $U-U_{fb}$=1V and ε=10.

Using equations. (2.9), (2.10), (2.11) the capacitance of the space charge region can be evaluated as function of the applied potential U:

$$C_{sc}^{-2}=\frac{2}{\varepsilon\varepsilon_0 qN_d}\left(U-U_{FB}-\frac{kT}{q}\right) \quad (2.12)$$

The above expression is referred to as the Mott-Schottky equation and plots of C^{-2}_{sc} vs. potential are used to determine the flat band potential, U_{fb}, and the doping density N_d.

2.4.2 Semiconductor/Electrolyte Interface under Illumination

When the surface is irradiated with light of energy greater than the band-gap E_g, photons are absorbed and hole-electron pairs are created. Some of these, especially those formed beyond the space charge region, recombine with the evolution of heat. However, the space charge field promotes the separation of electrons and holes. The holes, delivered to the surface at an effective potential equivalent to the valence band edge, can take part in oxidation reactions while the electrons move into the external circuit. Under illumination, a photocurrent flows as long as the potential of the electrode is more positive than E_{fb}, so that electron-hole pair separation can occur. Thus the onset

of the photocurrent is near E_{fb}, although surface recombination processes can move this onset toward more positive values.

The flux of photogenerated holes to the surface will depend on the width of the space charge region, the optical absorption coefficient of the semiconductor and the diffusion length of holes. Holes generated adjacent to the space charge region may reach the edge of the space charge region layer by diffusion. This is accounted for by assuming a diffusion layer of width L, in which electron-hole pair separation is fully effective:

$$L = \sqrt{D\tau_p} = \sqrt{kT\mu_p\tau_p} \tag{2.13}$$

Here D is the diffusion coefficient, μ_p is the corresponding mobility of the hole and τ_p is the recombination time of holes. Electron-hole pairs generated in the neutral bulk region deeper than the diffusion layer (i.e. at $x>d_{sc}+L$) will recombine. This situation is depicted in **Figure 2.6.**

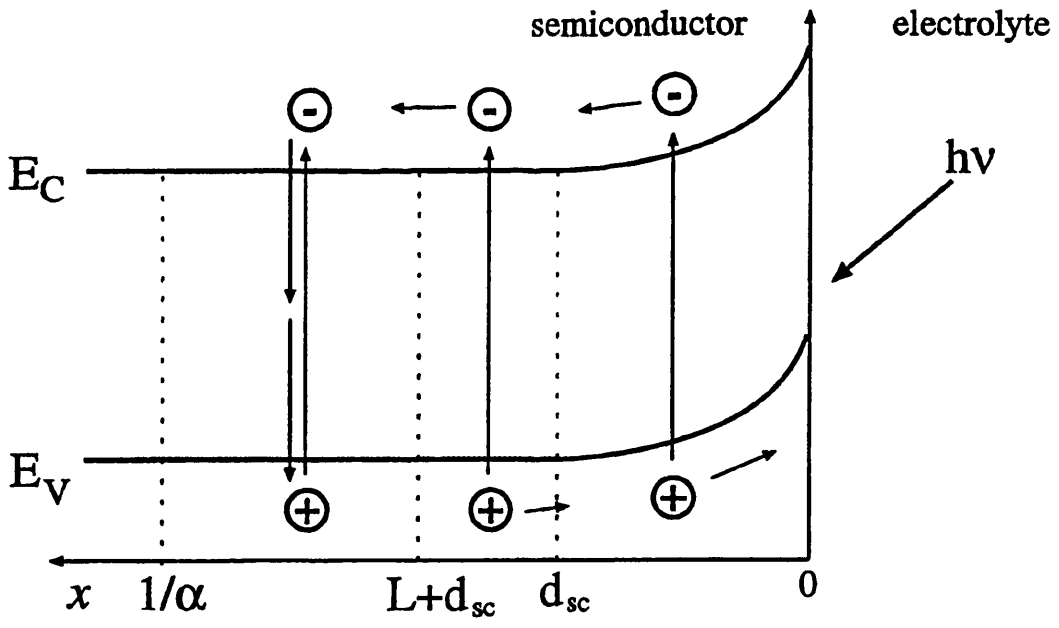

Figure 2.6. An *n*-type semiconductor electrode under depletion conditions illuminated from the electrolyte side. Holes generated in the depletion layer and in the diffusion layer contribute to the photocurrent. The holes generated beyond $L+d_{SC}$ recombine.

Provided that there are no loss mechanisms and the interface acts as an ideal sink for minority carriers, the photocurrent will depend only on generation and collection. The boundary value problem corresponding to this situation was solved by Gärtner [21]. In the steady state, the potential and intensity dependence of the photocurrent j_{photo} is given by:

$$\frac{J_{photo}}{qI_0} = 1 - \frac{e^{-\alpha d_{sc}}}{1+\alpha L} \tag{2.14}$$

Here I_0 is the incident photon flux corrected for reflection loss, α is the absorption coefficient, L is the diffusion length for minority carriers and d_{sc} is the thickness of the space charge region. The ratio J_{photo}/qI_0 is the photocurrent conversion efficiency Φ. The photocurrent quantum efficiency is instead defined by the number of photoinjected electrons over the number of absorbed photons. Plots of $ln(1-\Phi)$ against d_{SC} (which according to the Mott-Schottky relationship is proportional to $(U-U_{fb})^{1/2}$) have been used to determine the absorption coefficient of the light and diffusion length L of the minority carriers.

2.4.3 Interfacial Processes

For a flat semiconductor/electrolyte interface the flux of generated minority carriers close to the semiconductor surface can be predicted provided that the minority carriers are consumed sufficiently rapidly by interfacial electron transfer processes to ensure that their concentration in the depletion layer and at the surface can be neglected. The Gärtner model (equation (2.14)) has been used successfully to explain the photocurrent-potential characteristics of many single crystalline semiconductor electrodes, especially in the potential region where the band bending is relatively large.

However, for lower values of the band bending, the photocurrent quantum yield, i.e. the ratio of the number of photogenerated electrons over the number of photons absorbed, decreases more steeply with decreasing potential than what is predicted by equation (2.14). In fact, it is observed that the photocurrent goes to zero whilst a considerable depletion layer is still present. This suggests that the flux of minority carriers taking part in the electrochemical reactions is smaller than the flux of minority carriers reaching the surface. It follows that the minority carriers recombine at the surface, most of the recombination occurs at the surface and in the near surface region rather than in the bulk [22].

The ratio between charge transfer and surface recombination is then the determining factor behind the energy conversion efficiency of the semiconductor electrolyte interface. The theory of charge transfer proposed by Marcus [23-25]-Gerischer [26,27] considers that the charge transfer rate depends largely on the degree of overlap between the fluctuating energy levels of the redox species and the electron energy band of the solid. The fluctuating energy levels of the redox species are given by the *reorganisation energy* λ. This energy accounts for changes in the inner and outer solvation shells of the hole acceptor species. In principle, if the energy level of the reduced species coincides with the energy of the valence band (E_V), direct transfer of the hole can occur, as shown in **Figure 2.7**. On the other hand if the energy of the reduced species lies above E_V, the hole may be trapped initially in an energy level within the band-gap before being transferred across. It follows that the minority carrier (holes, for an *n*-type semiconductor) transfer can be very slow hence trapping in interfacial band-gap states may compete with charge transfer.

Trapping of a hole can be written as follows:

$$h^+ + X \xrightarrow{\beta_p} X^+ \qquad (2.15)$$

here X/X^+ are respectively a band-gap state occupied and unoccupied by an electron, β_p

is the hole trapping rate. β_p for bulky localized states is given by the product of the capture cross section and the thermal velocity [28-32]. The rate of hole trapping per state is then given by $\beta_p p(0) f(E)$, where $p(0)$ is the concentration of free holes at the surface and $f(E)$ is the density of states in the band-gap. Thermal excitation can release the minority carrier from the band-gap states into the valence band. The rate of this process depends exponentially on the distance between the band-gap state occupied and the valence band edge, according to: $\beta_p N_V exp[-(E-E_V)/kT](1-f(E))$. This represents the rate at energy E.

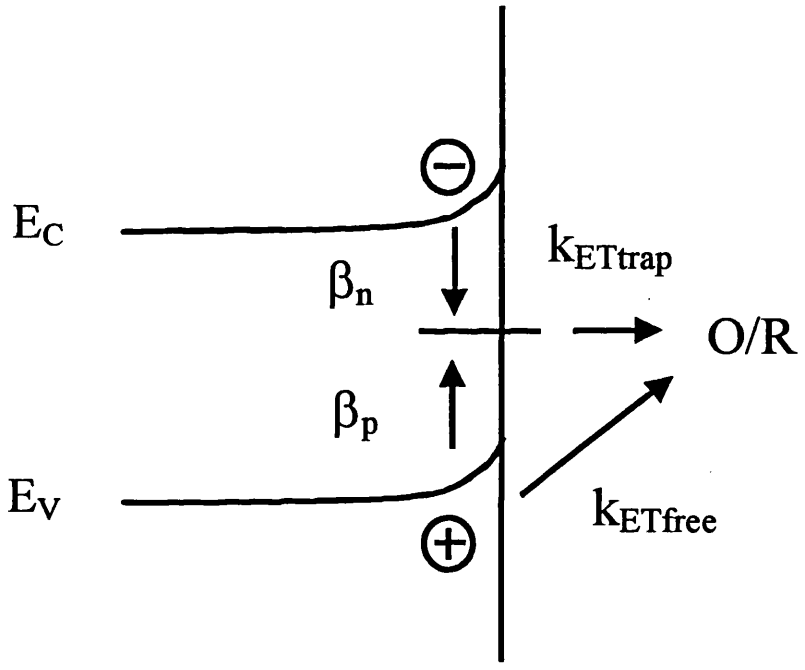

Figure 2.7. Schematic representation of a hole transfer directly from the valence band and via the surface traps.

Once a hole has been trapped, two processes can occur at the interface: either electron donation from the reducing agent in solution or capture of a free electron. The two processes can be written as follows:

$$X^+ + Red \xrightarrow{k_{ETtrap}} X + Ox \qquad (2.16)$$

$$X^+ + e^- \xrightarrow{\beta_n} X \qquad (2.17)$$

In order for the first process to occur, isoenergetic electron tunneling is involved from a non-equilibrium state of the reducing agent at a given energy. The rate of the second process, i.e. the electron capture rate, is given by $\beta_n n(0)(1-f(E))$, where $n(0)$ is the concentration of free electrons at the surface. Trapped electrons can be released by thermal energy, and as for the holes, this rate depends exponentially on the energy difference in between the energy of the band-gap state and the edge of the conduction band. It can be expressed as $\beta_n N_C exp[-(E-E_C)/kT]f(E)$. The *demarcation level* [33,34] then defines the energy level where the rate of thermal release and recombination are the same. For example electrons above the demarcation level of electrons are excited into the conduction band, whilst the ones below recombine. Analogously for holes, the ones above the demarcation level of holes recombine and the ones below are excited into the valence band.

2.5 Porous Electrodes

2.5.1 Porous Semiconductor Electrodes

Networks of interconnected semiconducting particles of dimension in the nanometer range are currently being investigated for their interesting properties. Nanoporous electrodes can be used in several new devices such as dye-sensitized photovoltaic cells [11], photonic crystals [35] and electrochromic windows [36].

These nanostructures are very interesting from a scientific point of view because of their large surface/volume (A/V) ratio, this means that for a dye-sensitized solar cells the light harvesting by the monolayer of the dye adsorbed on the surface of the nanostructure is enhanced. For a structure built up from hexagonally close packed spheres of radius r the fraction volume occupancy is 0.73, the corresponding surface/volume ratio is given by 0.73×3/r. For a radius of 15 nm the A/V obtained is of

10^6 cm^{-1}, it follows that for a 1 cm^2 film of 10 μm thickness the internal surface area is of 1000 cm^2. This is an upper limit as the fractional volume occupancy is normally less than 0.73 and the necks illustrated in **Figure 2.8** in between the nanoparticles have been neglected. This feature of interconnected nanoparticles means that a monolayer of dye adsorbed onto the internal area of the film will absorb almost all the incident light at the wavelength corresponding to its absorption spectrum. On the other hand, for a flat electrode the dye will normally absorb only 0.1% of the incident light. Another consequence of the large *A/V* in porous electrodes is the increase of the density of surface states. In fact, normally for a flat electrode the density of surface states is 10^{12}-$10^{13}cm^{-2}$, whilst for a porous electrode it becomes 10^{18}-$10^{19}cm^{-2}$. These high densities of traps enhance light absorption by electrons in the surface states. This effect is usually responsible for large photocurrent quantum yields for sub-band-gap light measurements, which have been carried out for nanoporous GaP, SiC and TiO_2 [37-39].

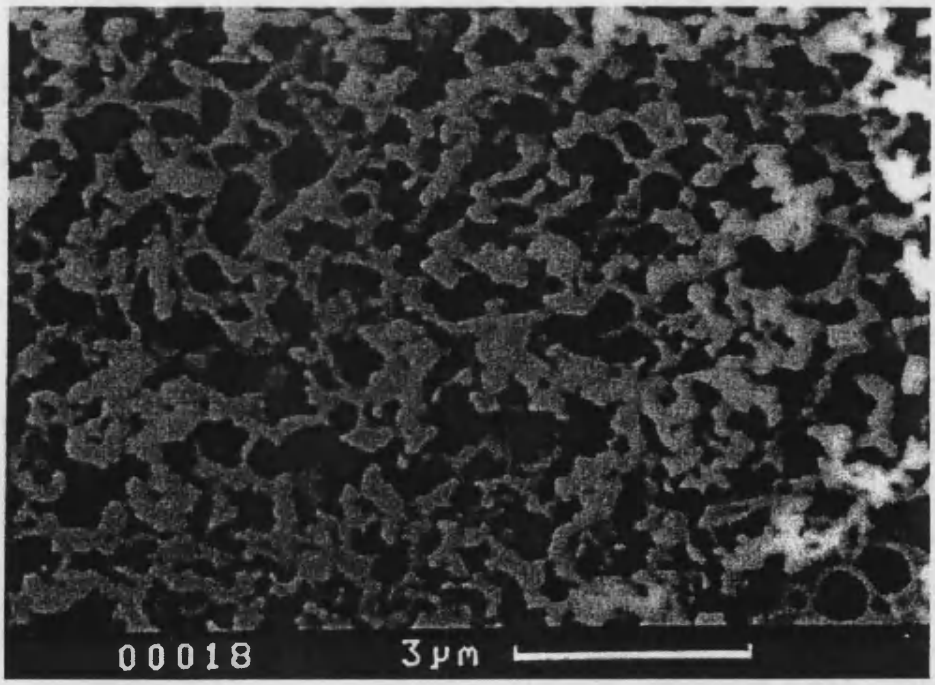

Figure 2.8. SEM photograph of a nanoporous GaP network. The white areas are GaP and the dark areas are pores [41].

Finally another difference between flat and porous electrodes is the fact that for the latter the space charge region can no longer be defined. The width of the depletion region for a bulk semiconductor with doping density of $10^{17}cm^{-3}$ is of the order of 100nm. It follows that for particles smaller than 100nm the space charge region becomes meaningless. If the pores are of the same dimensions as the particles which form the network, then an internal Helmholtz double layer is formed. As a consequence of the large internal area of the network, the electrode behaves like a 'supercapacitor' under accumulation conditions.

2.5.2 Porous Semiconductor Electrodes under Illumination

Charge generation in a nanocrystalline electrode can occur in two different ways. The first mechanism involves electron-hole generation due to the absorption of light by the semiconducting electrode with subsequent charge transfer at the solid/electrolyte interface. Alternatively the charge generation can occur by absorption of the light by an adsorbed dye, followed by injection into the conduction band of the semiconducting network. The dye is then regenerated by electron transfer from I^- in solution. For both mechanisms the electrons are collected at the back contact and measured as photocurrent. Both mechanisms are shown in **Figure 2.9**.

In the dark, the Fermi level of the semiconductor electrode is in equilibrium with E_{redox} of the electrolyte and is independent of the spatial co-ordinate x. Under illumination a non-equilibrium steady state situation is established which can be described by the quasi-Fermi levels for electrons and holes, $E_{F,n}$ and $E_{F,p}$. The expressions for $E_{F,n}$ and $E_{F,p}$ are the same as the ones in equations (2.2) and (2.3) except that now the concentrations of electrons and holes are given by: $n=n_0+\Delta n$ and $p=p_0+\Delta p$. Here n_0 and p_0 are respectively the electron and hole concentrations in the

dark and Δn and Δp are the excess electron and hole concentrations generated by illumination. The holes will quickly reach the surface of the nanostructured network and they react with the *Red* generating *Ox*. This means that $E_{F,p}$ is close to E_{redox} as shown in **Figure 2.10**. The electrons instead react much more slowly than holes at the surface.

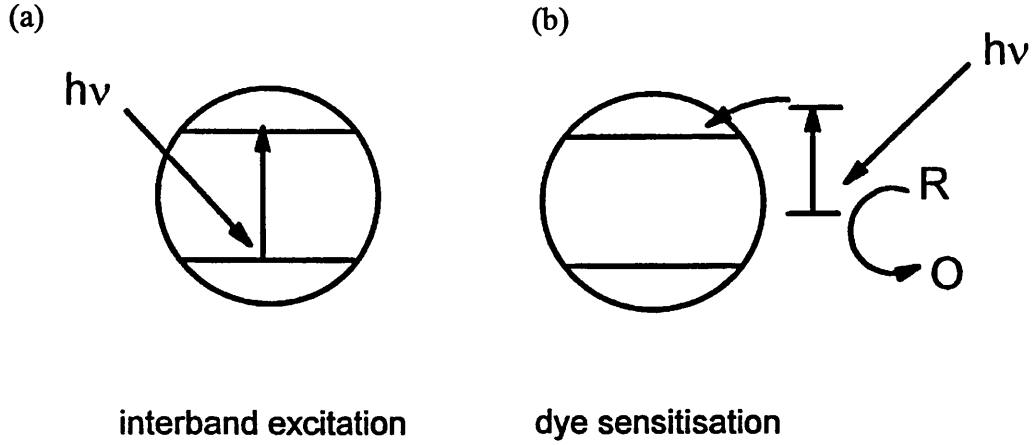

Figure 2.9. Charge generation with light absorption from the semiconducting network (a) and from the dye (b), followed by injection into the semiconductor.

The reason is not clear at present but it is the prerequisite for the observation of photocurrent. The flux of electrons at the back contact is proportional to the gradient of the quasi-Fermi level. The nature of this force, which drives electrons toward the back contact, is not well understood, but it can be due to diffusion and migration. A general expression for the gradient of the quasi-Fermi level is given by:

$$-\frac{1}{e}\frac{\partial E_{F,n}(x,t)}{\partial x}=\frac{\partial \varphi(x,t)}{\partial x}-\frac{kT}{e}\frac{1}{n(x,t)}\frac{\partial n(x,t)}{\partial x} \tag{2.18}$$

The first term on the right hand side accounts for migration, the second for diffusion. Most works on electron transport in nanostructured films assume that the driving force of the majority carriers to the back contact is due to diffusion. However it can be shown [14] that the potential drop across the Helmholtz double layer, responsible for

migration, can actually depend on distance forming a gradient of the quasi-Fermi level of electrons. Under short circuit conditions, for typical levels of solar irradiance, the electron concentration at the substrate is zero and at the other end of the film is about $10^{18}cm^{-3}$. Since the volume of particles with a radius of 20nm is $3\times10^{-17}cm^{3}$, the electron density of $10^{18}cm^{-3}$ corresponds to about 30 electrons per particle and to a surface charge of $10^{-7}Ccm^{-2}$. The change in the potential drop across the Helmholtz layer is around 10mV if the Helmholtz capacitance is $10\mu Fcm^{-2}$. For a ten micron thick film this corresponds to average electric field of $10Vcm^{-1}$. Comparison of the average magnitude of the two terms in equation (2.18) shows that the contribution of the electric field to electron transport, although relatively small, cannot be neglected at very high light intensity. A more detailed treatment of the driving force for electron transport in nanocrystalline films has been given recently by de Jongh and Vanmaekelbergh [12]. However there is no complete study which takes into account both diffusion and migration, although some attempts have been made within the framework of statistical mechanics [40]. Therefore all the work on electron transport in nanoparticulate films are based on the assumption that the driving force is either diffusion or migration. In the present work, it is assumed that diffusion is the dominating form of transport [41,42].

Several experiments have been performed to measure the diffusion coefficient of majority carriers in TiO_2 porous electrodes. It has been found [42,43] that the diffusion coefficient is several orders of magnitude smaller than the one of a flat electrode. The reason for such a difference of the diffusion coefficient is not clear at present. One hypothesis is that the transport is slowed down by the effect of trapping and detrapping which is enhanced in porous electrodes given the high density of surface states (10^{18}-$10^{19}cm^{-3}$). Electrons get temporarily localized in the deepest unoccupied traps, i.e. near the demarcation level ($f(E)\approx 1$).

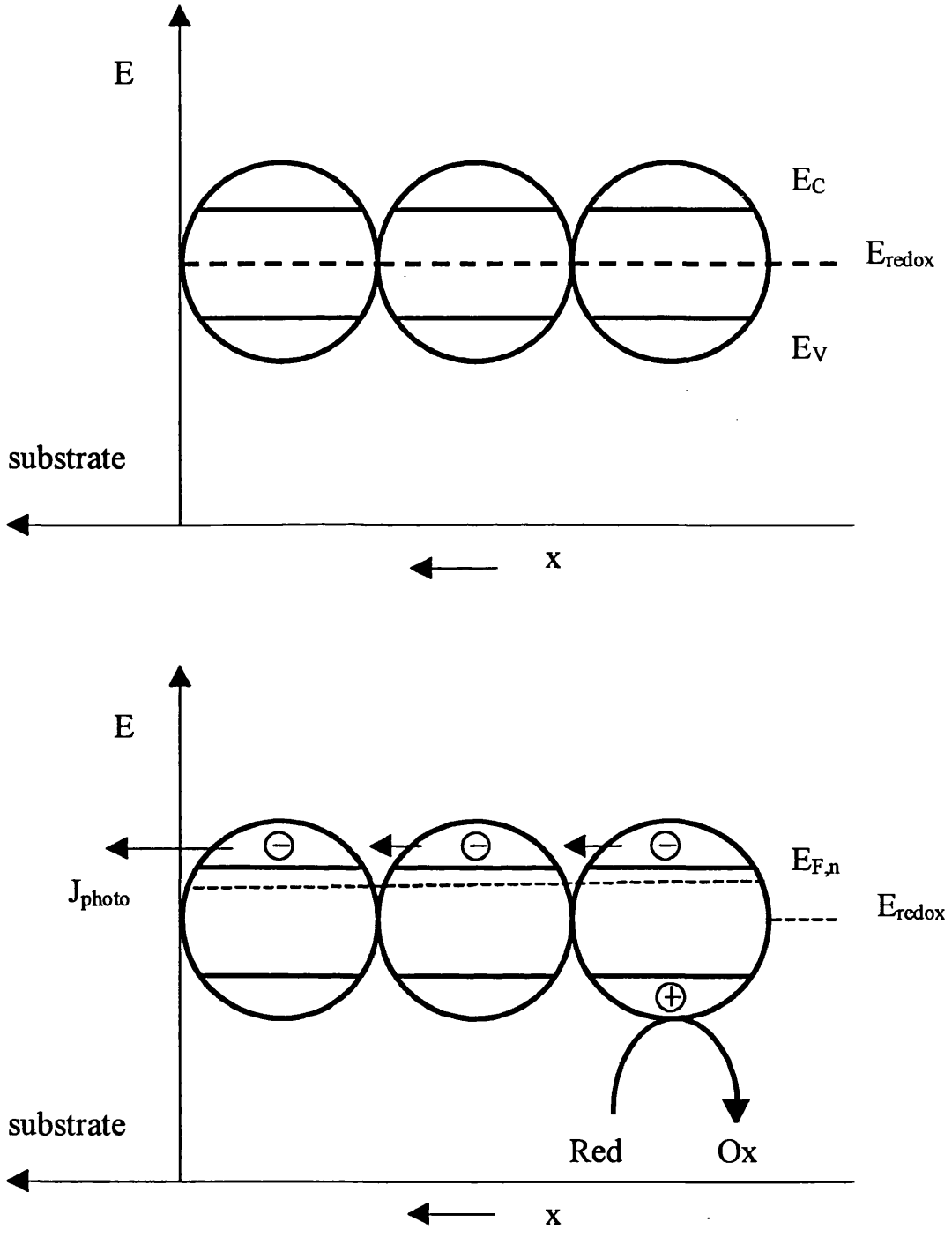

Figure 2.10. Schematic representation of a semiconducting nanoparticulate network (a) in the dark, (b) under illumination. It can be noted that in the dark the $E_{F,n}$ does not depend on x and is equal to E_{redox}. Under illumination $E_{F,p}$ is equal to E_{redox}, whilst a gradient of $E_{F,n}$ along x is formed.

Södergen et al. [44] have developed a model to analyze electron transport in porous electrodes. This model is based on the assumption that electron transport occurs via diffusion. The possibility that electrons react with I_3^- is also considered, hence an electron lifetime is defined which is longer than the diffusion time for high collection efficiency. The electron concentration as function of the time and the spatial co-ordinate x can then be found from the following equation:

$$\frac{\partial n(x,t)}{\partial t} = \eta \alpha I_0 e^{-\alpha x} + D\frac{\partial^2 n(x,t)}{\partial x^2} - \frac{n(x,t) - n_0}{\tau} \tag{2.19}$$

For dye-sensitised porous TiO_2 electrodes the first term represents the local rate of electron creation by the photosensitization process. The second one is Fick's second law and takes into account diffusion of electrons through the nanoporous TiO_2 network. The third one considers the fact that photoinjected electrons may react with tri-iodide ions before they reach the substrate, τ is therefore the inverse of the pseudo-first order rate constant for electron/I_3^- reaction, and $n(x)$-n_0 is the excess of electron concentration. Here D is the diffusion coefficient of electrons, n_0 is the electron density in the dark, τ is the pseudo-first order lifetime of electrons determined by the back reaction with tri-iodide ions in solution, α is the effective absorption coefficient of the dye-sensitised TiO_2 (determined by the absorption cross section and surface coverage of the dye), I_0 is the incident photon flux corrected for reflection losses and η is the net efficiency of electron injection, i.e. takes into account that electrons in TiO_2 can react with the oxidised state of the dye.

This model is also appropriate for bare TiO_2 electrodes, in which case the first term of equation (2.19) represents the hole-electron pair generation. α is the absorption coefficient of porous TiO_2 determined by the product of the absorption coefficient of TiO_2 and the porosity of the film. For bare TiO_2 the net injection efficiency, η, is determined by the hole-electron recombination rate.

This approach does not take into account the fact that the diffusion coefficient depends on trapping and detrapping, which means that D is function of n and consequently of x. In section 3.5.2 the effective diffusion coefficient is introduced, which, even if in a simplified view, considers the effect of trapping and detrapping. Similarly the electron lifetime τ depends on trapping and detrapping and therefore on n and x, the effective lifetime is introduced in section 3.5.2 as well. The net injection efficiency, η, for dye-sensitised electrodes, is also affected by the electron density as it represents the possibility that free electrons can back react with the oxidised state of the dye. Ideally, the dye should be regenerated by the capture of an electron from iodide, but under strong accumulation condition, electrons can instead be captured from the TiO_2, so that η becomes dependent on the total electron density [45,46]. For dye-free TiO_2 electrodes the net injection efficiency, η, is determined by the hole-electron recombination rate and it is not only dependent on the electron density but also on the film porosity. In fact, in the regions where the film is not very porous there is little interpenetration between the solid and the liquid phase, reducing the probability that the hole left in the valence band of TiO_2 captures an electron from iodide in solution. Concluding equation (2.19) is the core of the modelling developed in the present work, it is solved for steady and periodic light illumination and modification due to the effect of trapping/detrapping and the distance dependence of the parameters is introduced.

2.6 Conclusion

A brief overview of the processes occurring in flat and porous semiconductor electrodes has been given. In the present work, TiO_2 porous electrodes, with and without dye sensitisation, have been studied using light modulated techniques. The results obtained with light modulated techniques are modelled using equation (2.19) as

shown in section 3.6. Chapter V introduces the distance dependence of the absorption coefficient and the net injection efficiency in order to obtain a satisfactory fitting of the experimental IMPS data. The effect of trapping and detrapping is also introduced, however the model is restricted to the case of single-trap. It is proved that this is the main limitation of the model developed in the present work.

2.7 References

[1] A. Heller, Acc. Chem. Res., 14, 154, (1981).

[2] A. Heller, Solar Energy, 29, 153, (1982).

[3] G. Hodes, S. J. Fonash, A. Heller and B. Miller, Adv. Electrochem. Electrochem. Eng., 13, 113, (1984).

[4] H. Gerischer, Pure. Appl. Chem., 52, 2649, (1980).

[5] A. J. Bard, J. Phys. Chem., 86, 172, (1982).

[6] A. J. Bard, J. Electroanal. Chem., 168, 5, (1984).

[7] Y. V. Pleskov, Prog. Surf. Sci., 15, 401, (1984).

[8] R. Memming, Topics in Current Chemistry, 153, 79, (1988).

[9] N. S. Lewis, Nature, 345, 293, (1990).

[10] Y. V. Pleskov, 'Solar Energy Conversion-a photoelectrochemical approach', Springer, Berlin, (1990).

[11] B. O' Regan and M. Grätzel, Nature, 353, 737, (1991).

[12] P. E. de Jongh and D. Vanmaekelbergh, J. Phys. Chem., 103, 747, (1999).

[13] L. M. Peter, E. A. Ponomarev, G. Franco and N. J. Shaw, Electrochim. Acta, submitted for publication.

[14] A. Zaban, A. Meier and B. A Gregg, J. Phys. Chem., 101, 7985, (1997).

[15] S. R. Morrison, 'Electrochemistry at Semiconductor and Oxidised Metal

Electrodes', SRI International, Plenum Press, (1981).

[16] M. Hofman-Perez and H Gerischer, Z. Elektrochem., 65, 771, (1961).

[17] S. R. Morrison, 'Surface Phenomena Associated with the Semiconductor/Electrolyte Interface', Prog. Surf. Sci., 1, 106, (1971).

[18] T. Freund and S.R. Morrison, Surf. Sci., 9, 119, (1968).

[19] S. R. Morrison and T. Freund, Electrochim. Acta, 13, 1343, (1968).

[20] R. R. Dogonadze, A. M. Kuznetsov, and Yu. A. Chizmadzhev, Russ. J. Phys. Chem., 38, 652, (1964).

[21] W. W. Gärtner, Phys. Rev., 116, 84, (1959).

[22] J. Li, R. Peat and L. M. Peter, J. Electroanal. Chem., 165, 41, (1984).

[23] R. A. Marcus, J. Chem. Phys., 24, 966, (1956).

[24] R. A. Marcus, Can. J. Chem., 37, 155, (1959).

[25] R. A. Marcus, J. Chem.Phys., 43, 679, (1965).

[26] H. Gerischer, Z. Phys. Chem. N. F., 26, 233, (1960).

[27] H. Gerischer, Z. Phys. Chem. N. F., 27, 40, (1961).

[28] W. Shockley and W. T. Read, Phys. Rev, 87, 835, (1952).

[29] R. N. Hall, Phys. Rev., 87, 387, (1952).

[30] A. Rose, Prog. In Semicond., 2, 211, (1956).

[31] R. H. Bube and F. Cardon, J. Appl. Phys., 35, 2712, (1964).

[32] G. Simmons and G. W. Taylor, Phys. Rev. B, 4, 502, (1971).

[33] R. H. Bube, 'Photoelectric Properties of Semiconductors', Cambridge University Press, (1992).

[34] L. M. Peter and D. Vanmaekelbergh, Adv. Electrochem. Sci. and Eng., Ed., R. C. Alkire and D. M. Kolb, 6, 77, (1999).

[35] J. D. Joannopoulos, P. R. Villeneuve and S. Fan, Nature, 386, 143 (1997) and references therein.

[36] C. G. Granquist, 'Handbook of Inorganic Electrochromic Materials', Elsevier, Amsterdam, (1995).

[37] D. Vanmaekelbergh, B. H. Erné, C. W. Cheung and R. W. Tjekstra, Electrochim. Acta, 40, 689, (1995).

[38] B. H. Erné, D. Vanmaekelbergh and J. J. Kelly, Adv. Mater., 7, 739, (1995).

[39] P. E. de Jongh and D. Vanmaekelbergh, J. Phys. Chem. B, 101, 2716, (1997).

[40] A. J. Bard, J. Electroanal. Chem., 168, 5, (1984).

[41] D. Vanmaekelbergh, F. Iranzo Marín and J. van de Lagmaat, Ber. Bunsenges. Phys. Chem., 100, 616, (1996).

[42] L. Dloczik, O. Ileperuma, I. Lauermann, L. M. Peter, E. A. Ponomarev, G. Redmond, N. J. Shaw and I. Uhlendorf, J. Phys. Chem. B, 101, 10281, (1997).

[43] F. Cao, G. Oskam, G. J. Meyer and P. C. Searson, J. Phys. Chem., 100, 17021, (1996).

[44] S. Södergen, A. Hagfeldt, J. Olsson, S. -E. Lindquist, J. Phys. Chem., 98, 5552, (1994).

[45] S. Y. Huang, G. Schlichthörl, A. J. Nozik, M. Grätzel and A. J. Frank, J. Phys. Chem. B, 101, 2576, (1997).

[46] G. Schlichthörl, N. G. Park and A. J. Frank, J. Phys. Chem. B, 103, 782, (1999).

CHAPTER III

THEORY

3.1 Introduction

The most established frequency-resolved technique in electrochemistry is electrochemical impedance spectroscopy (EIS) [1-3], which analyses the response of electrochemical systems to periodic perturbations of voltage or current. EIS can be used to study semiconductor electrodes not only in the dark but also under conditions of steady illumination, in which case the term photoelectrochemical impedance spectroscopy applies (PEIS) [4-9]. Another common frequency-resolved method is intensity modulated photocurrent spectroscopy (IMPS) [10-12] which involves modulation of the intensity of illumination incident on an electrode and measurement of the magnitude and phase shift of the resulting photocurrent relative to the periodic illumination. Another method closely related to IMPS is intensity modulated photovoltage spectroscopy (IMVS) [13-15] which involves modulation of the light intensity and measurement of the modulated photovoltage. The present work has resulted in the development of a novel frequency-resolved technique, i.e. photomodulated infrared transmittance spectroscopy (PITS) [16]. These techniques have been applied to porous TiO_2 systems with and without dye sensitisation, and they have proved to be a powerful approach to the investigation of these systems.

3.2 Ac Techniques

A sinusoidal voltage can be expressed using the complex notation, as follows:

$$\hat{V}_{IN} = |V_{IN}|e^{i\omega t} \tag{3.1}$$

where $|V_{IN}|$ is the amplitude (volts), ω is 2π times the frequency (Hertz), t is the time (seconds) and $i=\sqrt{-1}$. For a linear system, for example a resistor and a capacitor in series, the output voltage across the capacitor (**Figure 3.1**) is a sinusoidal signal at the same frequency as the input voltage but shifted by a phase angle ϕ and with different amplitude. It can be written as:

$$\hat{V}_{OUT} = |V_{OUT}|e^{i(\omega t+\phi)} \tag{3.2}$$

here $|V_{OUT}|$ is the amplitude of the output sinusoidal voltage (volts) and ϕ is the phase angle, as shown in **Figure 3.2(a)**. The phase and the amplitude of a sinusoidal signal can also be represented in the complex plot as shown in **Figure3.2(b)**.

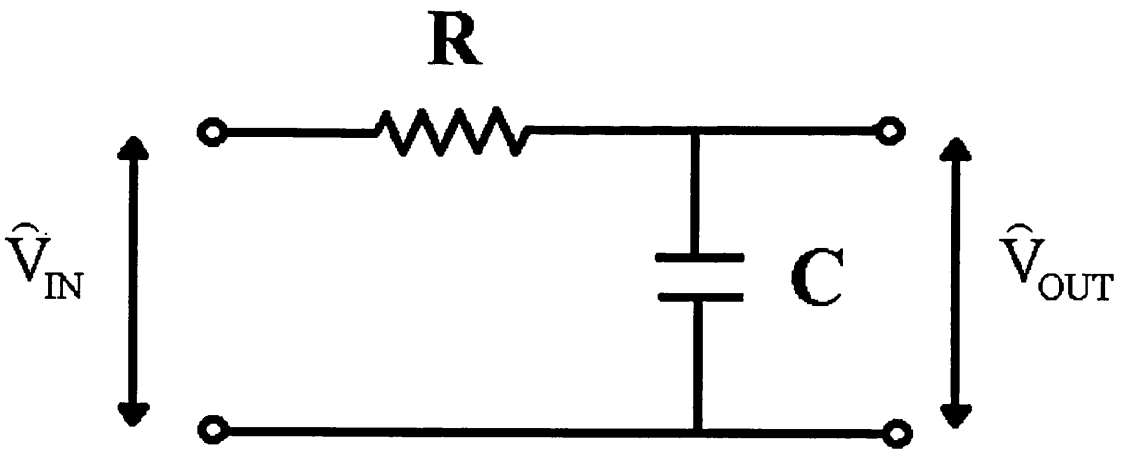

Figure 3.1. *RC* series circuit. The gain $G(\omega)$ is given by $\hat{V}_{OUT}$, the voltage across the capacitor, over $\hat{V}_{IN}$.

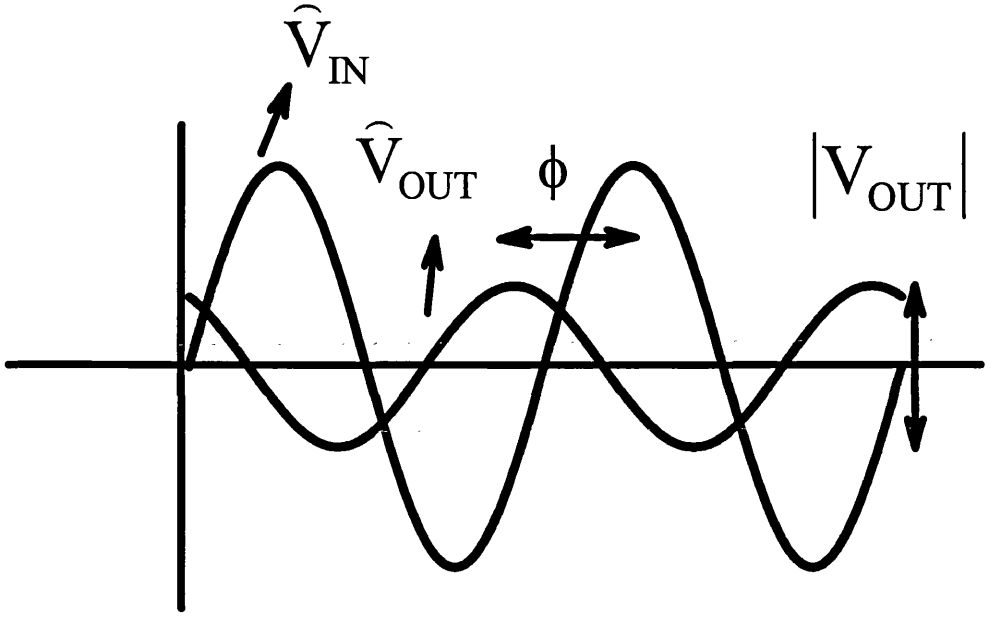

Figure 3.2(a). Diagram showing the relationship between the sinusoidal input and output voltages at frequency $\omega/2\pi$ shifted by the phase angle ϕ.

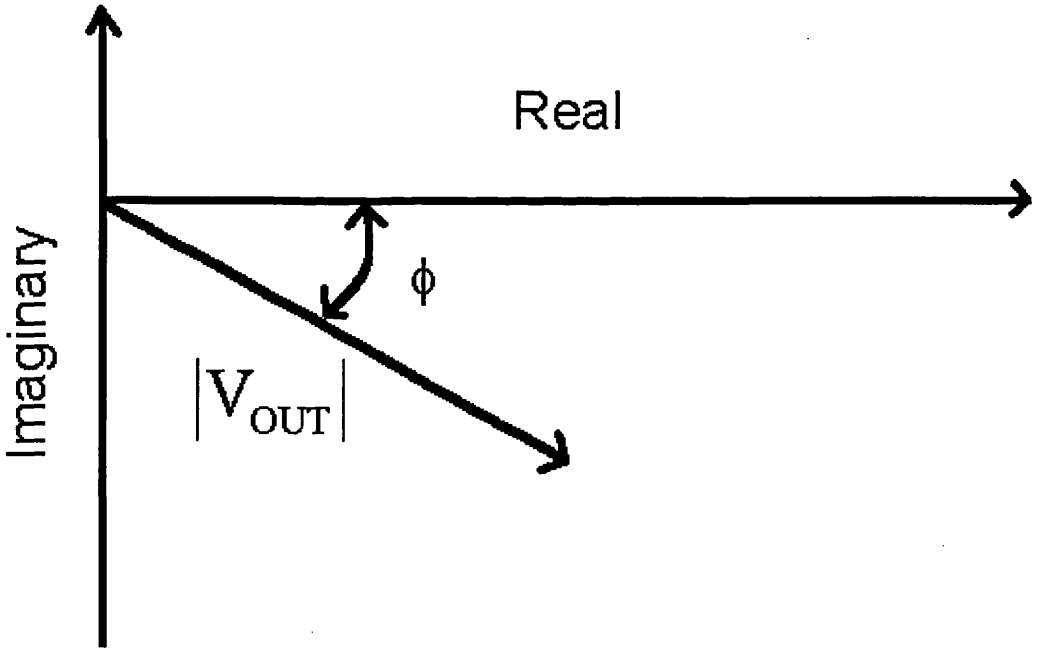

Figure 3.2(b). Complex plane representation of the magnitude $|V_{OUT}|$ and the phase ϕ.

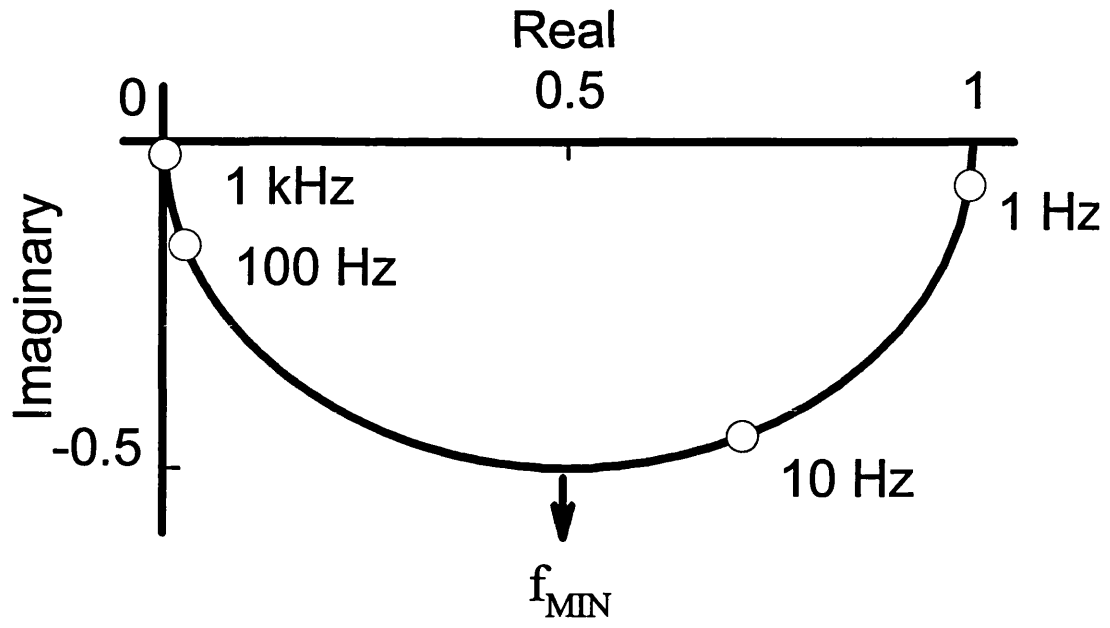

Figure 3.3(a). Complex plane plot of the gain $G(\omega)$ for the circuit in **Figure 3.1** with R=1kΩ and C=10μF. The minimum of the semicircle is obtained for frequency $f_{min}=1/(2\pi RC)$=16Hz.

The ratio of the two voltages, the voltage gain G, can be written as:

$$G = \frac{\hat{V}_{OUT}}{\hat{V}_{IN}} = \frac{|V_{OUT}|}{|V_{IN}|} e^{i\phi} \tag{3.3}$$

The gain can be measured over a range of frequencies. For the series connection of a resistor and a capacitor, shown in **Figure 3.1**, the gain in the frequency domain is given by:

$$G(\omega) = \frac{1}{1 + i\omega RC} \tag{3.4}$$

The result is normally shown as a complex plane plot like **Figure 3.3(a)**. In the complex plane plot $G(\omega)$ forms a semicircle in the 4th quadrant. At low frequencies, $G(\omega)$ is equal to 1, at high frequencies it tends to 0 and the imaginary component reaches a minimum for $\omega=(RC)^{-1}$. **Figure 3.3(a)** shows the gain in the complex plot for R=1kΩ and C=10μF. The Bode plots are alternative to the complex plane plots, as shown in **Figure 3.3(b)**. In the Bode plots, the phase angle and the logarithm of the magnitude of

the complex transfer function are plotted against the logarithm of the frequency. The magnitude of the gain is given by $|G| = \sqrt{(Re(G(\omega)))^2 + (Im(G(\omega)))^2}$ and the phase is given by $\phi = arctan(Im(G(\omega))/Re(G(\omega)))$. It can be noted that at f_{min} the magnitude is 0.5 and the phase shift is 45^0.

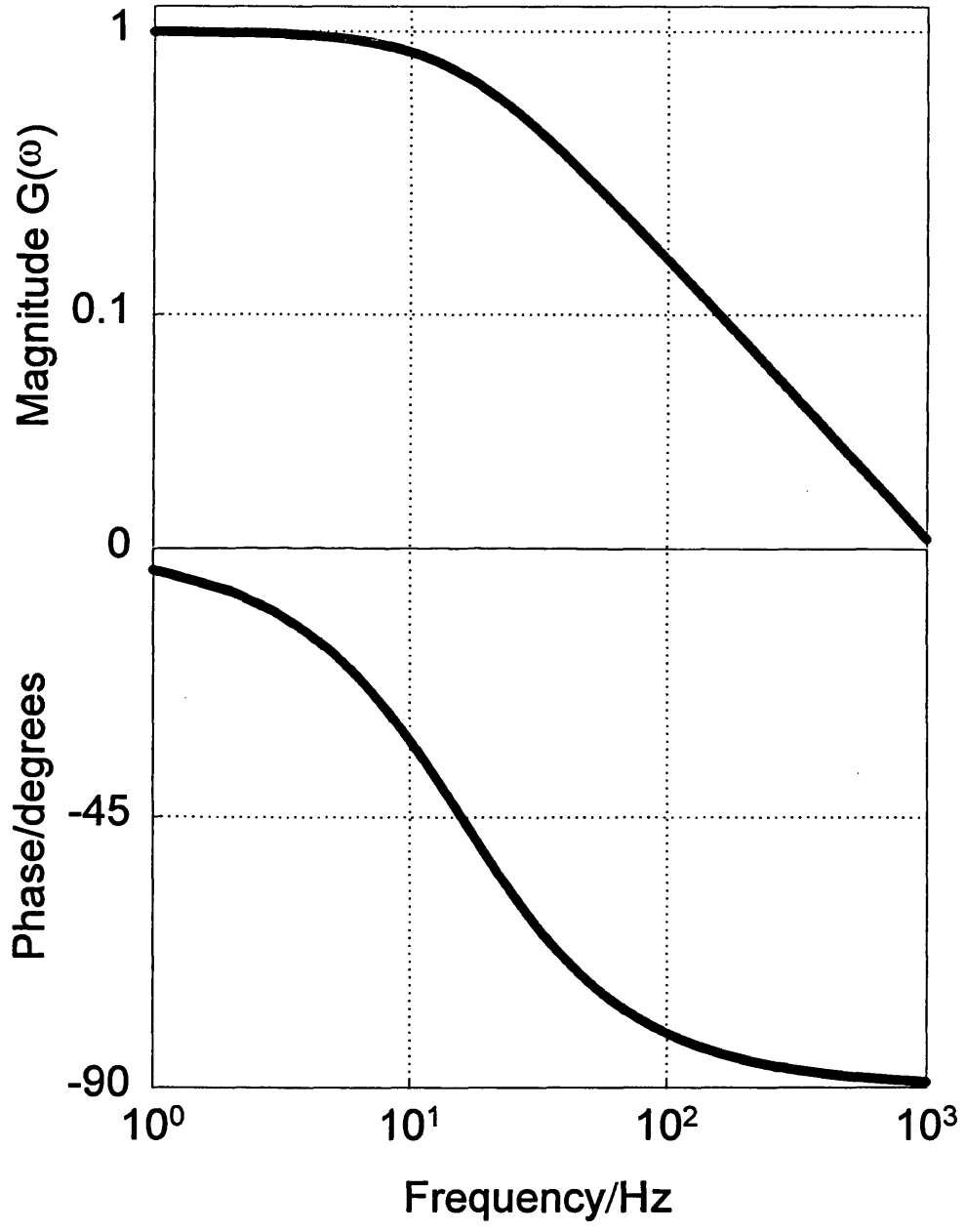

Figure 3.3(b). Bode plots of the magnitude and phase shift of $G(\omega)$. The magnitude is given by $|G| = \sqrt{(Re(G(\omega)))^2 + (Im(G(\omega)))^2}$ and the phase is given by $\phi = arctan(Im(G(\omega))/Re(G(\omega)))$. At f_{min} the magnitude is 0.5 and the phase shift is 45^0.

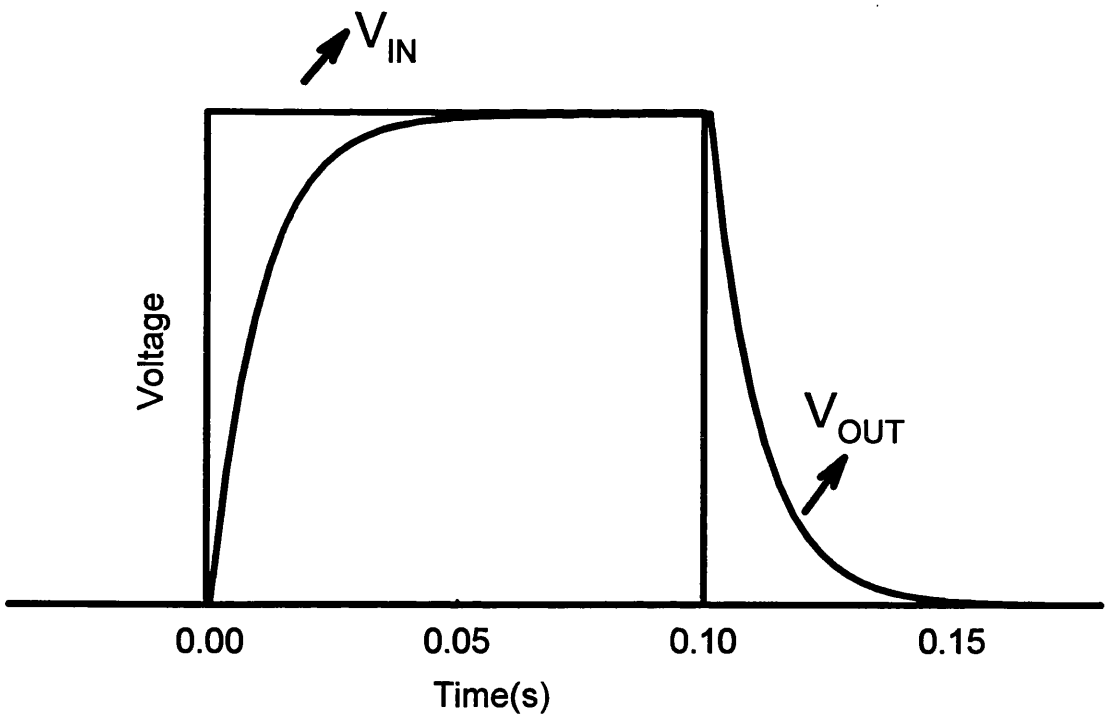

Figure 3.4. V_{OUT} response when a potential step is applied at the circuit shown in **Figure 3.1.** The time response of the circuit, τ, is equal to RC.

Experiments in the time domain can be performed by applying a potential step and measuring the output voltage. For the series of a resistor and a capacitor it can be shown that when the voltage is switched on V_{OUT}/V_{IN} as function of time is given by:

$$\frac{V_{OUT}}{V_{IN}}(t) = 1 - e^{-\frac{t}{RC}} \tag{3.5}$$

when the potential is switched off V_{OUT}/V_{IN}, for a 0.1 s potential step, becomes:

$$\frac{V_{OUT}}{V_{IN}}(t) = e^{-\frac{(t-0.1)}{RC}} \tag{3.6}$$

Figure 3.4 shows the response of the circuit to a potential step. The two domains, frequency and time, mathematically can be related to each other by Fourier transformation. This definition of ac measurements can be extended to other physical quantities. Usually the input functions are either light or voltage; the output functions can be current, charge, optical absorbance/transmittance or microwave reflectivity.

When the input function is an intensive quantity and the output is an extensive quantity, their ratio is normally referred to as impedance, for example Z=Voltage(intensive)/Current(extensive). For the inverse situation it becomes admittance. If the input and output functions are of the same type, then their ratio is referred to as gain. In table 3.1 it is showed a variety of input and output functions with the corresponding ratio.

Table 3.1

Sinusoidal Perturbation	**Sinusoidal Response**	**Type of transfer function**
Voltage V	Voltage V	Gain V/V (dimensionless)
Current I	Voltage V	Admittance I/V ($VA^{-1}=\Omega^{-1}$)
Voltage V	Current I	Impedance V/I ($V^{-1}A=\Omega$)
Voltage V	Charge Q	Integrated admittance Q/V ($CV^{-1}=F$)
Voltage V	Absorbance A	Optical transfer function A/V (V^{-1})
Voltage V	Transmittance T	Optical transfer function T/V (V^{-1})
Light flux I_0	Photocurrent J_{photo}	Quantum efficiency j_{photo}/qI_0 (dimensionless)
Light flux I_0	Photovoltage V_{photo}	Photovoltage impedance V_{photo}/qI_0 ($VA^{-1}=\Omega$)
Light flux I_0	Transmittance T	Optical transfer function T/qI_0 (A^{-1})

These ac techniques are finding increasing application to nanocrystalline electrodes. These systems exhibit unusual experimental responses to pulsed or a periodic perturbation of the light intensity. The main feature of the photocurrent of nanoparticulate films to pulsed illumination is their slow response, which is of the order of milliseconds. **Figure 3.5** shows the photocurrent transients reported by Solbrand et al. [17] for a TiO_2 nanocrystalline film excited with pulsed illumination at a wavelength of 308nm in a solution of $0.7moldm^{-3}$ $LiClO_4$ in ethanol. The experiment was repeated for different film thicknesses. It can be noted that the photocurrent transient exhibits a

peak on a timescale of milliseconds. The second feature to be noted is that the time at which the peak occurs varies approximately with the square of the film thickness. As the diffusion time is given by $\tau_D = d^2/D$, where d is the film thickness and D is the diffusion coefficient, the fact that the time at which the peak occurs varies with the square of the film thickness suggests that the electron transport is diffusion controlled. **Figure 3.6** shows photocurrent transients for square pulse illumination of dye-sensitised TiO_2 films by Cao et al. [18], it can be noted that the photocurrent response is non-exponential. These results also show that the photocurrent response to illumination step is faster when the light intensity is higher. **Figure 3.7** shows the semilogarithmic plot of the photocurrent response to a single step (see equation (3.5)) and the non-exponential behaviour becomes evident.

This non-exponential response of photocurrent transients to light pulsed illumination of nanoparticulate films suggests using small amplitude perturbations in order to permit linearisation. This is achieved by superimposing a small modulation on top of a much larger dc illumination intensity. For impedance measurements, linearisation is achieved by superimposing a small sinusoidal perturbation on top of a dc potential.

In the present work, a variety of ac techniques has been applied such as intensity modulated photocurrent spectroscopy (IMPS) [12,19], intensity modulated photovoltage spectroscopy (IMVS) [20], impedance and measurements of photomodulated infrared transmittance spectroscopy (PITS) [16].

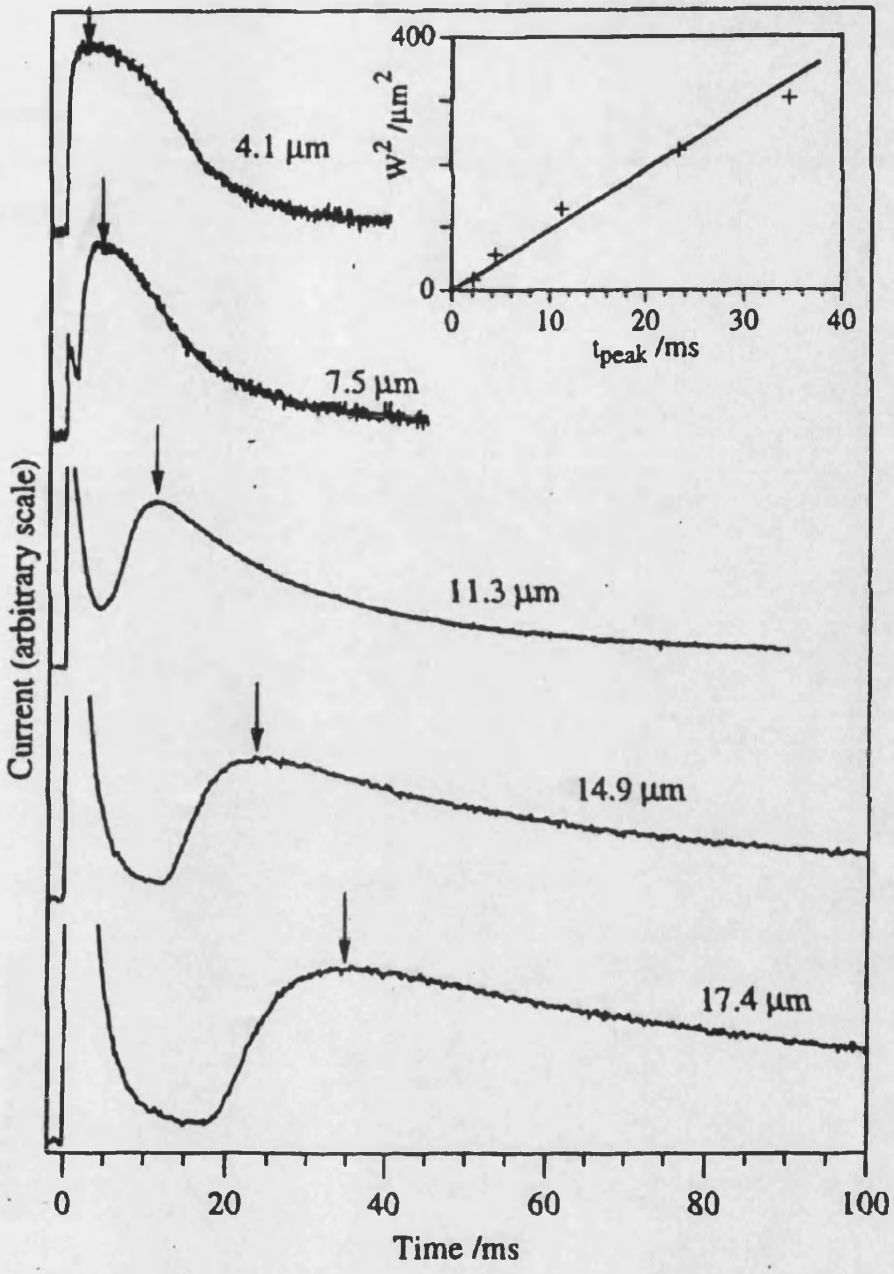

Figure 3.5. Experimental photocurrent transients for pulsed laser excitation of nanocrystalline TiO_2 electrodes with different thicknesses [17]. The experiment is performed with illumination from the electrolyte side (200 mJ, 30 ns, 308 nm) in 0.7 mol dm^{-4} $LiClO_4$ in ethanol. The inset shows that t_{peak}, the time at which the current peak occurs, depends on the square of the film thickness W.

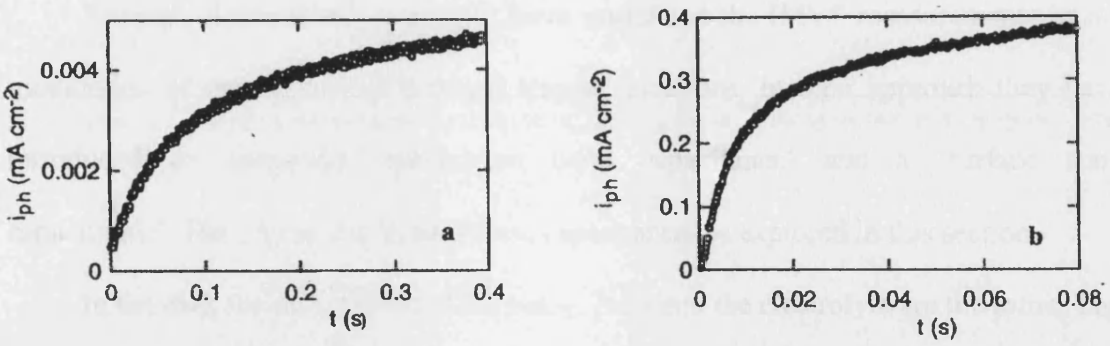

Figure 3.6. Transient short circuit photocurrent response of dye-sensitised TiO_2 solar cells to light step excitation at 514nm with an intensity of 0.05mWcm^{-2}(a) and 4mWcm^{-2}(b) [18]. The current rises more rapidly at higher light intensity.

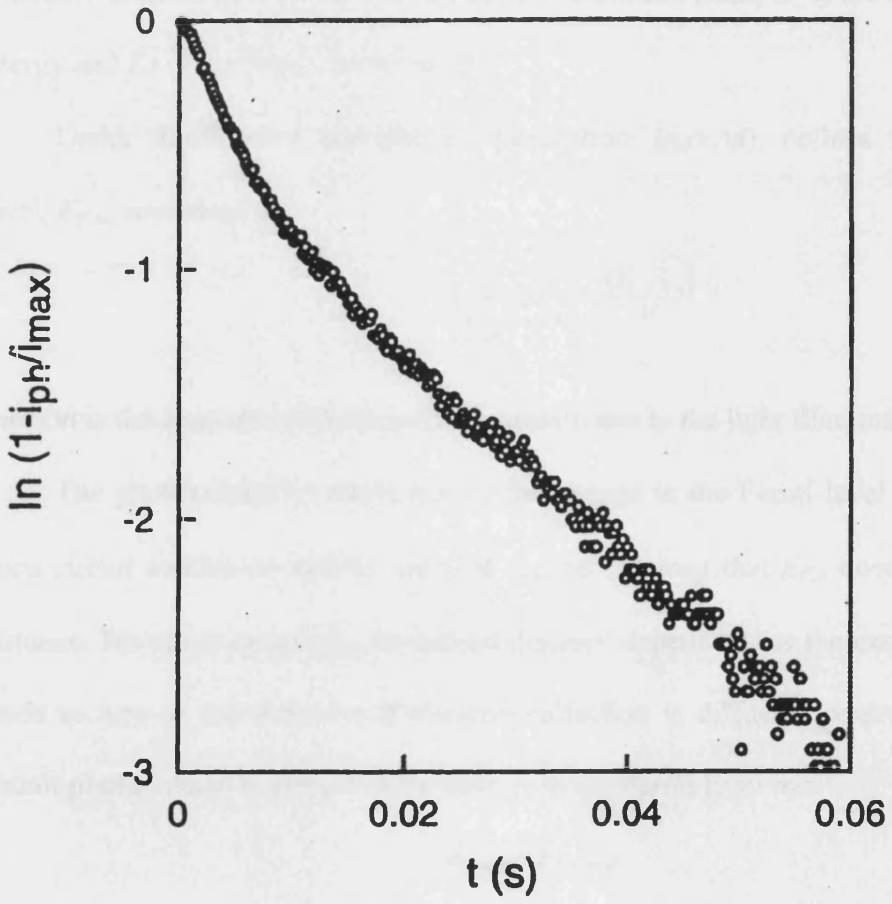

Figure 3.7. Semilogarithmic plot of the photocurrent transients shown in **Figure 3.6(b)** [18].

3.3 Intensity Modulated Photovoltage Spectroscopy

Recently Schlichthörl et al. [20] have associated the IMVS measurements to the modulation of the density of free and trapped electrons. In their approach they have introduced an empirical 'conduction band capacitance' and a 'surface state capacitance'. The physical origin of these capacitances is explored in this section.

In the dark the Fermi level of the SnO_2, TiO_2 and the electrolyte are the same. The Fermi-Dirac distribution gives the density of electrons in the conduction band in the dark at equilibrium:

$$\frac{n_0}{N_C} = e^{-\frac{(E_C - E_F)}{kT}} \tag{3.7}$$

where N_C is the total number of states in the conduction band, E_C is the conduction band energy and E_F is the Fermi level energy.

Under illumination the electron population, $(n_0+\Delta n)$, defines the quasi-Fermi level, $E_{F,n}$, according to:

$$\frac{n_0 + \Delta n}{N_C} = e^{-\frac{(E_C - E_{F,n})}{kT}} \tag{3.8}$$

here Δn is the increase in electron concentration due to the light illumination.

The photovoltage is a measure of the change in the Fermi level in the TiO_2. At open circuit conditions and for $\alpha d \approx 1$ it can be assumed that $E_{F,n}$ does not depend on distance. For short circuit $E_{F,n}$ is instead distance dependent, as the excess of electrons tends to zero at the substrate if electron collection is diffusion controlled. The open circuit photovoltage is related to the change in the Fermi level by:

$$qU_{photo} = E_{F,n} - E_F \tag{3.9}$$

Equation (3.8) then can be rewritten in the form:

$$\frac{n_0 + \Delta n}{N_C} = e^{-\frac{(E_C - E_F - qU_{photo})}{kT}} = e^{-\left(\frac{E_C - E_F}{kT}\right)} e^{\frac{qU_{photo}}{kT}} \tag{3.10}$$

If a small periodic intensity modulation is superimposed on the dc background, equation (3.10) becomes:

$$\frac{n_0 + \Delta n + \delta n}{N_C} = e^{-\left(\frac{E_C - E_F}{kT}\right)} e^{\frac{qU_{photo}}{kT}} e^{\frac{q\delta U_{photo}}{kT}} \tag{3.11}$$

here δn is the periodic component of the excess of electron density and δU_{photo} is the periodic photovoltage. Linearising the last term in equation (3.11) it follows:

$$\frac{\delta n}{N_C} = e^{-\left(\frac{E_C - E_F}{kT}\right)} e^{\frac{qU_{photo}}{kT}} \frac{q\delta U_{photo}}{kT} \tag{3.12}$$

The modulation of the conduction band electron density per unit area (δQ_{cb}) in a film of thickness d is therefore given by:

$$\delta Q_{cb} = qd\delta n = \frac{q^2 N_C d}{kT} e^{-\left(\frac{E_C - E_F}{kT}\right)} e^{\frac{qU_{photo}}{kT}} \delta U_{photo} \tag{3.13}$$

The 'conduction band capacitance' is then obtained to relate the modulated photovoltage to the modulated free charge:

$$C_{cb} = \frac{q^2 N_C d}{kT} e^{-\left(\frac{E_C - E_F}{kT}\right)} e^{\frac{qU_{photo}}{kT}} \tag{3.14}$$

The preceding treatment does not give any information about trapped electrons. In the dark at equilibrium, the trapped electrons density is given by:

$$n_t^0 = \int_{E_V}^{E_C} N(E) f(E) dE \approx \int_{E_V}^{E_F} N(E) dE \tag{3.15}$$

here $N(E)$ is the density of state function for traps in the band-gap and $f(E)$ is the Fermi-Dirac function.

Under illumination, the trapped electron density is determined by the quasi-Fermi level $E_{F,n}$, which can be considered independent of distance at open circuit, according to:

$$n_t = \int_{E_V}^{E_{F,n}} N(E) dE \tag{3.16}$$

It can be shown that the change in electron density δn_t arising from a small additional optical perturbation of the electron quasi-Fermi level is:

$$\delta n_t = N(E_{F,n})\delta E_{F,n} = N(E_{F,n})q\delta U_{photo} \tag{3.17}$$

here $N(E_{F,n})$ is the density of electron traps at the quasi-Fermi level. The modulated trapped charge per unit area in a film of thickness d is then given by:

$$qd\delta n_t = q^2 N(E_{F,n})d\delta U_{photo} \tag{3.18}$$

The 'surface state capacitance' can then be defined according to:

$$C_t = dq^2 N(E_{F,n}) \tag{3.19}$$

In this way the modulated photovoltage can be related to the perturbation of the trapped charge density.

It follows that the total photomodulated charge in the nanocrystalline electrode is given by:

$$\delta Q_{tot} = (C_{cb} + C_t)\delta U_{photo} = C_{total}\delta U_{photo} \tag{3.20}$$

where C_{total} is the total capacitance of the nanocrystalline electrode under illumination, i.e. the sum of C_{cb} and C_t.

The low frequency value of the total modulated charge can be related to the pseudo-first order electron lifetime, τ, and the rate of electron injection, η. If all injected electrons are collected at short circuit, the injection rate is given by the short circuit current density j_{photo} so that:

$$\delta Q_{tot} = \eta(U_{photo})j_{photo}\tau \tag{3.21}$$

here τ is the electron lifetime determined by the back reaction with I_3^-, j_{photo} is the short circuit current and $\eta(U_{photo})$ is the rate of injection, which is assumed to be equal to unity under short circuit conditions. $\eta(U_{photo})$ takes into account the fact that injected electrons can not only react with I_3^- but also with the oxidised state of the dye, D^+. The rate of this process depends on the electron concentration. Under short circuit

conditions, it is close to unity, but it is reported to occur on ns timescale under conditions of strong accumulation [21]. Therefore under open circuit conditions $\eta(U_{photo})$ is less than unity as the reaction of the injected electrons with the oxidised state of the dye can no longer be neglected.

$\eta(U_{photo})$, at open circuit, can be calculated from the equations which describe the competition between the dye regeneration by I^- and the back reaction of electrons with D^+:

$$\frac{\partial[D^+]}{\partial t} = \alpha I_0 e^{-\alpha x} - k_{reg}[I^-][D^+] - k_{back} n[D^+] \tag{3.22}$$

$$\frac{\partial n}{\partial t} = D\frac{\partial^2 n}{\partial x^2} - k_{back} n[D^+] - k_{rec} n[I_3^-] + \alpha I_0 e^{-\alpha x} \tag{3.23}$$

where α is the absorption coefficient, k_{reg} is the rate of the regeneration of the dye, k_{back} is the rate of recombination of the injected electrons with the dye, D is the diffusion coefficient and $k_{rec}=1/(\tau[I_3^-])$ is the rate of recombination of the electrons with I_3^-. Since the regeneration and the back reaction processes involving D^+ are on a much shorter timescale (ns) than the reaction of electrons with I_3^- (ms), steady state can be assumed for equation (3.22):

$$[D^+] = \frac{\alpha I_0 e^{-\alpha x}}{k_{reg}[I^-] + k_{back} n} \tag{3.24}$$

Equation (3.23) can be rewritten as:

$$\frac{\partial n}{\partial t} = D\frac{\partial^2 n}{\partial x^2} - \frac{n}{\tau} + \alpha I_0 e^{-\alpha x}\left[\frac{k_{reg}[I^-]}{k_{back} n + k_{reg}[I^-]}\right] \tag{3.25}$$

It follows that the net injection efficiency can be defined as:

$$\eta = \left[\frac{k_{reg}[I^-]}{k_{back} n + k_{reg}[I^-]}\right] \tag{3.26}$$

where k_{reg} and k_{back} are the second-order rate constants for regeneration and back reactions respectively.

Schlichthörl et al. [20] have used equation (3.21) to calculate the modulated charge and hence the photocapacitance of a dye-sensitised electrode and they have assumed that $\eta(U_{photo})$ is equal to unity. In the present approach the photocapacitance is calculated from impedance measurements and $\eta(U_{photo})$ evaluated from equation (3.21).

3.4 Photoelectrochemical Impedance Spectroscopy

In electrochemical impedance spectroscopy (EIS) the potential is perturbed resulting in the modulation of the current. The electrochemical impedance response is then determined by the ratio of the perturbing ac voltage to the ac component of the total current. Photoelectrochemical impedance spectroscopy (PEIS) is similar to EIS except that the electrode is kept under constant light illumination intensity whilst the potential is perturbed. Photoelectrochemical impedance spectroscopy has been widely used to study photoelectrochemical reactions in semiconductors [1-9]. The impedance response of an electrochemical system can be modelled using equivalent circuit elements, such as resistors and capacitors. As discussed in section 3.3 a porous electrode can be represented by two capacitances in parallel: the 'conduction band capacitance' (C_{cb}) and the 'surface state capacitance' (C_t). Therefore the total capacitance is given by:

$$C_{tot}=C_{cb}+C_t \tag{3.27}$$

In the case of the Grätzel cell electrons can also recombine with I_3^- in solution or with the oxidised state of the dye. For a dye-free system only the former mechanism applies. In general the photocurrent as function of the voltage is non–linear and it can be written:

$$j_{photo}=f(U, I_0) \tag{3.28}$$

here j_{photo} is the photocurrent, U is the voltage and I_0 is the light illumination intensity. The system can be linearised for small potential perturbation using the Taylor series expansion, so the differential charge transfer resistance (or Faradaic resistance) can be defined and it is given by:

$$R_{ct} = \left(\frac{\partial U}{\partial j_{photo}} \right)\Bigg|_{U=U_0, I_0} \tag{3.29}$$

R_{ct} is the differential resistance calculated at the dc voltage U_0 and the light illumination intensity I_0. Therefore the equivalent circuit of a porous electrode, as illustrated in **Figure 3.8**, is given by the parallel of C_{tot} and R_{ct} with a serial resistance R_s which represents the resistance of the working electrode and the solution.

A more sophisticated model would take into account the distributed sheet resistance of the tin oxide electrode, which is connected via the impedance of the film to the distributed resistance of the electrolyte solution [22,23]. This means that the circuit shown in **Figure 3.8** is repeated n or infinite times as illustrated in **Figure 3.9.** The impedance of the system depicted in **Figure 3.9** is given by:

$$Z(\omega) = \sqrt{R_{sheet}\left(R_{el} + \frac{R_{ct}}{1 + i\omega C_{tot} R_{ct}} \right)}\, coth \frac{l R_{sheet}}{\sqrt{R_{sheet}\left(R_{el} + \frac{R_{ct}}{1 + i\omega C_{tot} R_{ct}} \right)}} \tag{3.30}$$

where R_{sheet} is the sheet resistance of the tin oxide sheet per unit length, R_{el} is the electrolyte resistance and l is the length of the electrode. For a long electrode ($l \to \infty$) equation (3.30) becomes:

$$Z(\omega) = \sqrt{R_{sheet}\left(R_{el+} \frac{R_{ct}}{1 + i\omega C_{tot} R_{ct}} \right)} \tag{3.31}$$

However, a satisfactory approximation is obtained using the lumped element approach, the impedance is therefore given by:

$$Z(\omega) = \frac{R_{ct}}{1 + i\omega C_{tot} R_{ct}} + R_{sheet} + R_{el} \tag{3.32}$$

The serial resistance of the dye-sensitised and dye-free systems presented in this work, $R_s = R_{sheet} + R_{el}$, is dominated by the resistance of the tin oxide sheet.

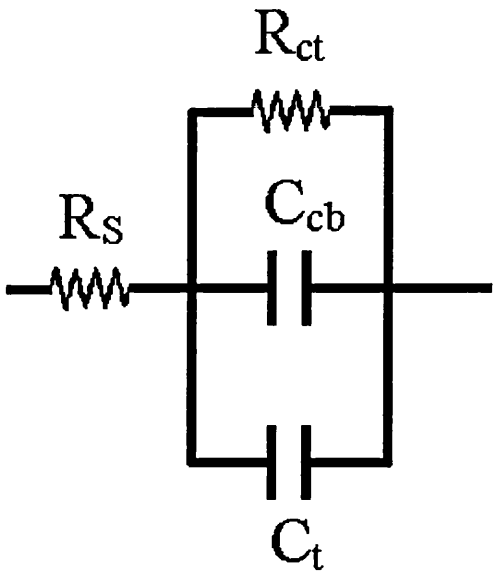

Figure 3.8. Equivalent circuit of a photoelectrochemical cell, R_S is the sum of the sheet and solution resistance, R_{ct} is the charge transfer resistance, C_t is the 'surface state capacitance' and C_{cb} is the 'conduction band capacitance'.

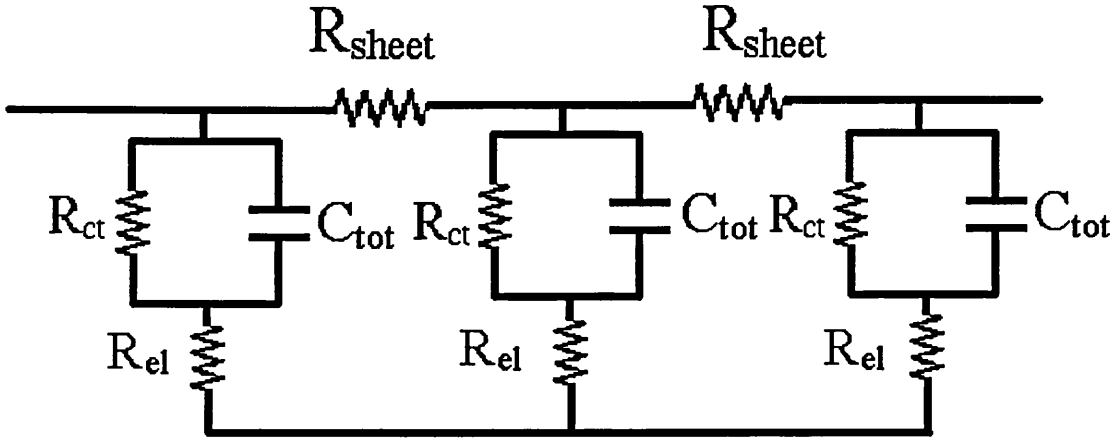

Figure 3.9. The equivalent circuit for a distributed resistance of the tin oxide sheet. It is obtained repeating *n*-times the circuit shown in **Figure 3.8.**

In conclusion, impedance measurements may be used to obtain the sheet resistance, the charge transfer resistance and the total capacitance can be evaluated. Replacing the value of the capacitance in equation (3.20), the photomodulated charge can be calculated and then related to transmission experiments as shown in chapter VI.

3.5 Intensity Modulated Photocurrent Spectroscopy

3.5.1 The Generation/Collection Problem: Steady State and Periodic Solutions

Chapter II introduced the generation/collection equation used by Södergen et al. [24], and its solution has been obtained by assuming that collection is diffusion controlled. Södergen et al. have provided steady state solutions of the problem for illumination from either side of the film. Numerical solutions for transient and periodic conditions have been given by Cao et al. [18]. More recently Dloczik et al. [12] have extended the model by Södergen et al. by introducing the kinetics of electron extraction into the boundary conditions. The generation/collection equation is given by:

$$\frac{\partial n(x,t)}{\partial t} = \eta\alpha I_0 e^{-\alpha x} + D\frac{\partial^2 n(x,t)}{\partial x^2} - \frac{n(x,t)-n_0}{\tau} \qquad (3.33)$$

A detailed description of all the terms in this equation is given in section 2.5.2. The first term represents the electron injection or hole-electron pairs generation for illumination from the substrate side, $x=0$. For illumination from the electrolyte side, in the exponent x must be replaced by d-x, where d is the thickness of the cell.

Before introducing the boundary conditions, it is important to consider the influence of the SnO_2/TiO_2 interface. Although the SnO_2/TiO_2 interface is not well understood the electrons may experience a potential dependent activation barrier in the contact region, so that the rate constants for electron extraction, k_{ext}, and injection, k_{inj}, may change with potential. The diffusion limited case is obtained when k_{ext} becomes

very large, on the other hand if k_{ext} is small the kinetically (or recombination) limit is obtained. Analogously it is assumed that the injection of electrons from the degenerate SnO_2 substrate also occurs across the energy barrier with a voltage dependent rate constant.

It is assumed that the rate constants for forward and reverse reactions can be described by the expressions:

$$k_{ext} = k_{ext}^{0} e^{\frac{-q\beta V}{kT}} \tag{3.34}$$

and

$$k_{inj} = k_{inj}^{0} e^{\frac{q(1-\beta)V}{kT}} \tag{3.35}$$

where V is the cell voltage and β is a symmetry factor that reflects the way in which changes in the potential at the interface affect the rate constants for forward and reverse electron transfer.

In order to obtain a steady sate and time dependent solutions of equation (3.33) it is necessary to introduce two boundary conditions. The first boundary condition is obtained from the fact that electrons can only be extracted on the substrate side of the film, therefore the electron flux, proportional to $\partial n / \partial x$, must be zero for $x \to d$, where d is the thickness of the film and $x=0$ is the substrate. The second boundary condition is that the flux of electrons at the substrate ($x=0$) must be equal to the rate of electron extraction, $k_{ext}n(0,t)$, that for the general case can be considered a first-order heterogeneous rate constant.

$$\left.\frac{\partial n}{\partial x}\right|_{x=d} = 0 \tag{3.36}$$

$$k_{ext} n(0,t) = D\left(\frac{\partial n}{\partial x}\right)\Bigg|_{x=0} \tag{3.37}$$

Equation (3.33) then becomes for the steady state case:

$$n(x)'' = \frac{n(x)}{\tau D} - \frac{\alpha I_0}{D} e^{-\alpha x} \tag{3.38}$$

with boundary conditions:

$$n'(d)=0 \tag{3.39}$$

$$Dn'(0)=k_{ext}n(0) \tag{3.40}$$

The steady state solution is then given by:

$$n(x) = Ae^{\gamma x} + Be^{-\gamma x} + Ce^{-\alpha x} \tag{3.41}$$

where

$$\gamma = \sqrt{\frac{1}{D\tau}} = \frac{1}{L_d} \tag{3.42}$$

and L_d is the diffusion length of electrons. The coefficients A, B, and C are given by:

$$C = \frac{\alpha I_0 / D}{\gamma^2 - \alpha^2} \tag{3.43}$$

$$A = C\frac{\alpha e^{-\alpha d}\left(k_{ext} + \gamma D\right) - \gamma e^{-\gamma d}\left(k_{ext} + \alpha D\right)}{\gamma\left(k_{ext}\left(e^{\gamma d} + e^{-\gamma d}\right) + D\gamma\left(e^{\gamma d} - e^{-\gamma d}\right)\right)} \tag{3.44}$$

$$B = -C\frac{\alpha e^{-\alpha d}\left(k_{ext} - \gamma D\right) + \gamma e^{-\gamma d}\left(k_{ext} + \alpha D\right)}{\gamma\left(k_{ext}\left(e^{\gamma d} + e^{-\gamma d}\right) + D\gamma\left(e^{\gamma d} - e^{-\gamma d}\right)\right)} \tag{3.45}$$

From this expression the electron density profile can be calculated at open (k_{ext}=0) and short circuit (large k_{ext}). **Figure 3.10** shows these two limiting cases.

The diffusion to the back contact and the back reaction with tri-iodide are the two competing processes for the collection of electrons at the back contact. The physical quantity which expresses this competition is the diffusion length, $L_d=(D\tau)^{1/2}=\gamma^{-1}$. For a cell to be efficient its thickness must be at the same time smaller than the diffusion length and bigger than the light penetration depth. **Figure 3.11** shows the effect of L_d on the electron density profile, $n(x)$, as function of the diffusion length. The electron profile exhibits a maximum for values of the diffusion length smaller than the film

thickness. This means that all the electrons generated beyond L_d recombine with the tri-iodide in solution.

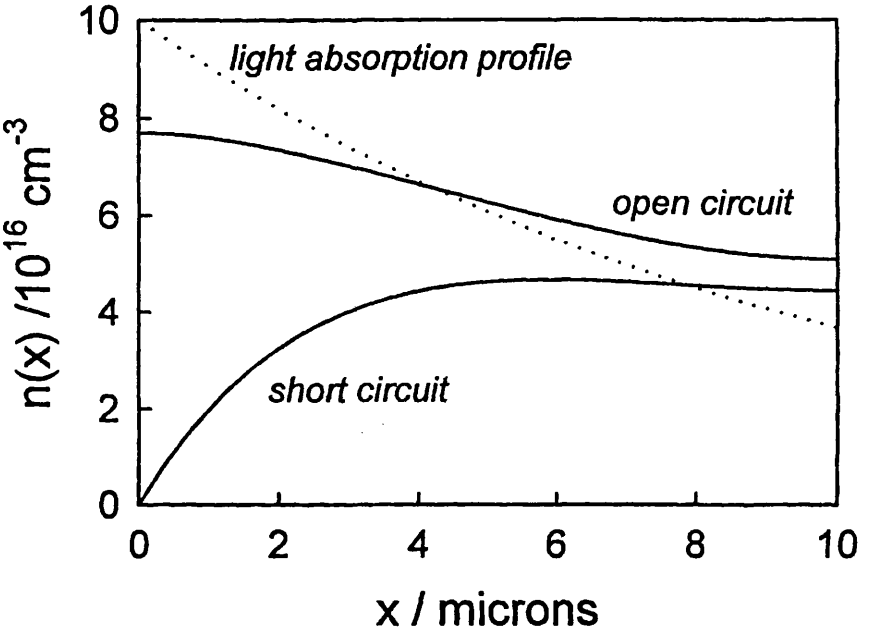

Figure 3.10. Steady state electron concentration profiles calculated from equations (3.41), (3.43), (3.44), and (3.45) at $\omega=0$ for $k_{ext}=0$ (open circuit) and for large k_{ext} (short circuit) for illumination from the substrate side for $\alpha=10^3 cm^{-1}$, $D=10^{-5} cm^2 s^{-1}$, $\tau=10ms$ and $I_0=10^{16} cm^{-2} s^{-1}$ [25].

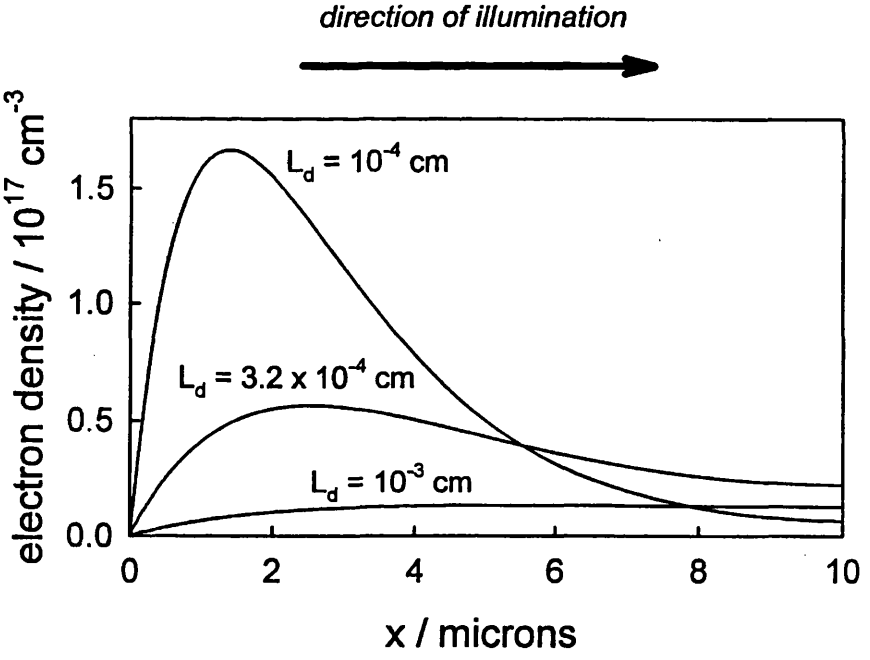

Figure 3.11. Electron density profiles as function of the diffusion length $L_d=(D\tau)^{1/2}$ for $\alpha=10^3 cm^{-1}$and $I_0=10^{16} cm^{-2} s^{-1}$. Note that the normalised steady state photocurrent falls as diffusion length decreases [25].

The solution of the generation/collection problem can be reformulated for periodic illumination; i.e. a small sinusoidal amplitude is superimposed on a constant background [12]:

$$I(t) = I_0 + \delta I_0 e^{i\omega t} \tag{3.46}$$

Here I_0 and δI_0 are respectively the photon flux of the constant and modulated light source. The time dependent electron concentration is of the form:

$$n(x,t) = u(x)e^{i\omega t} \tag{3.47}$$

The solutions of equation (3.33) for the periodic case are the same as the steady state case, equations (3.43), (3.44) and (3.45) apply, except that γ is now given by:

$$\gamma = \sqrt{\frac{1}{D\tau} + i\frac{\omega}{D}} \tag{3.48}$$

where ω is 2π the frequency, D is the diffusion coefficient and τ is the electron lifetime. The ac component of the photocurrent is given by:

$$j_{photo}(\omega) = D\left(\frac{\partial u}{\partial x}\right)\Big|_{x=0} = D(A\gamma - B\gamma - C\alpha) \tag{3.49}$$

The ac photocurrent conversion efficiency, $\Phi(\omega)$, for illumination from the substrate side is then given by:

$$\Phi(\omega) = \frac{J_{photo}(\omega)}{q\delta I_0} = \frac{\alpha}{\alpha+\gamma} \frac{e^{\gamma d} - e^{-\gamma d} + 2\alpha \dfrac{e^{-\alpha d} - e^{-\gamma d}}{\gamma - \alpha}}{e^{\gamma d} + e^{-\gamma d} + \dfrac{D\gamma}{k_{ext}}\left(e^{\gamma d} - e^{-\gamma d}\right)} \tag{3.50}$$

For the diffusion controlled case k_{ext} becomes very large, hence $\Phi(\omega)$ is given by:

$$\Phi(\omega) = \frac{\alpha}{\alpha+\gamma} \frac{e^{\gamma d} - e^{-\gamma d} + 2\alpha \dfrac{e^{-\alpha d} - e^{-\gamma d}}{\gamma - \alpha}}{e^{\gamma d} + e^{-\gamma d}} \tag{3.51}$$

An analogous treatment for illumination from the electrolyte side with appropriate boundary conditions gives:

$$u(x) = Ae^{\gamma x} + Be^{-\gamma x} + Ce^{\alpha x} \tag{3.52}$$

$$C = \frac{\alpha I_0 e^{-\alpha d} / D}{\gamma^2 - \alpha^2} \tag{3.53}$$

$$A = -C\frac{\alpha e^{-\alpha d}\left(k_{ext} + \gamma D\right) + \gamma e^{-\gamma d}\left(k_{ext} - \alpha D\right)}{\gamma\left(k_{ext}\left(e^{\gamma d} + e^{-\gamma d}\right) + D\gamma\left(e^{\gamma d} - e^{-\gamma d}\right)\right)} \tag{3.54}$$

$$B = C\frac{\alpha e^{\alpha d}\left(k_{ext} - \gamma D\right) + \gamma e^{\gamma d}\left(-k_{ext} + \alpha D\right)}{\gamma\left(k_{ext}\left(e^{\gamma d} + e^{-\gamma d}\right) + D\gamma\left(e^{\gamma d} - e^{-\gamma d}\right)\right)} \tag{3.55}$$

It follows that the photocurrent conversion efficiency is given by:

$$\Phi(\omega) = \frac{\alpha}{\alpha+\gamma}\frac{e^{(\gamma-\alpha)d} - e^{-(\alpha+\gamma)d} + 2\alpha\dfrac{e^{(\gamma-\alpha)d} - 1}{\gamma-\alpha}}{e^{\gamma d} + e^{-\gamma d} + \dfrac{D\gamma}{k_{ext}}\left(e^{\gamma d} - e^{-\gamma d}\right)} \tag{3.56}$$

The diffusion-controlled case is obtained for large values of k_{ext}, and then the conversion efficiency for illumination from the electrolyte side becomes:

$$\Phi(\omega) = \frac{\alpha}{\alpha+\gamma}\frac{e^{(\gamma-\alpha)d} - e^{-(\alpha+\gamma)d} + 2\alpha\dfrac{e^{(\gamma-\alpha)d} - 1}{\gamma-\alpha}}{e^{\gamma d} + e^{-\gamma d}} \tag{3.57}$$

In the diffusion-controlled limit the dc solution can be derived from equations (3.51) and (3.57) by setting ω=0, the expressions found are identical to the ones obtained by Södergen et al. [24].

Plotting equations (3.51) and (3.57) in the complex plane, as shown in **Figure 3.12, 3.13** and **3.14**, it appears that the IMPS response is in the 4th quadrant (positive real + negative imaginary). This means that the photocurrent lags behind the illumination, this is due to the time the electrons take to diffuse to the substrate. ω_{MIN}^{-1} is a good estimate of the transit time for electrons to reach the substrate. IMPS plots can be related to the photocurrent transients by performing the Fast Fourier Transform of equations (3.51) and (3.57) [25].

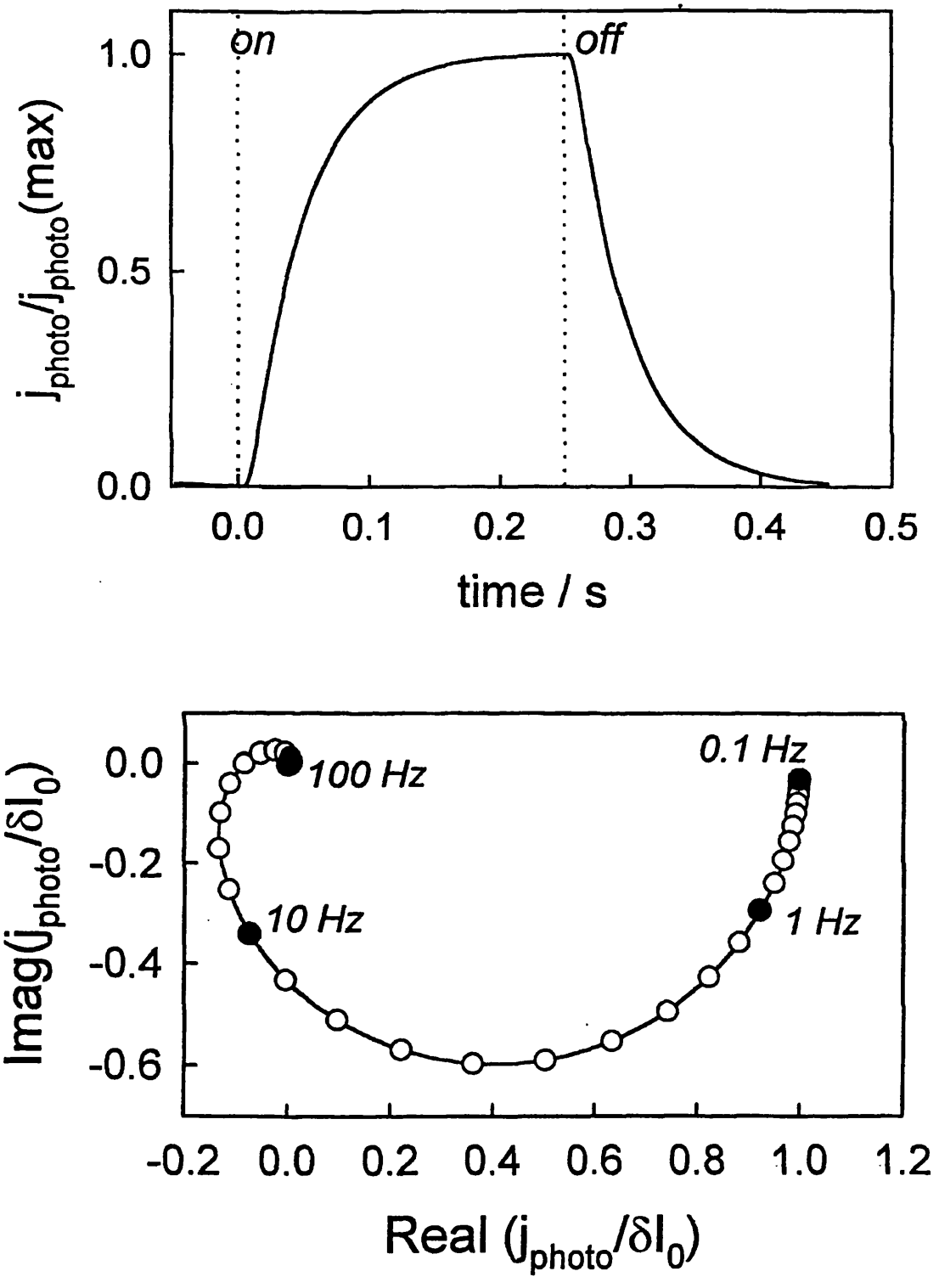

Figure 3.12. IMPS and photocurrent transients for illumination from the electrolyte side for $\alpha=10^5 cm^{-1}$, $d=10^{-3}$cm, $D=10^{-5}cm^2s^{-1}$ and $\tau\rightarrow\infty$ [25].

Figure 3.12 shows the quantum efficiency for illumination from the electrolyte side derived from equation (3.57) and the corresponding response to chopped illumination. It can be noted, in both the time and frequency domain, that the photocurrent strongly lags behind the absorbed light. In the time domain the time lag is evident, whilst in the frequency domain it is represented by the spiral approach to the origin at high frequencies. Experimentally this would be observed only for small absorption depths, i.e. high absorption coefficients, generally found for band to band excitation of electron-hole pairs rather than for electron injection in dye-sensitised cells. As the electron lifetime has been taken to be larger than the transit time, all the photoinjected electrons are collected at the substrate, i.e. $j_{photo}/q\delta I_0 \rightarrow 1$. The minimum occurs at 4 Hz, i.e. ω_{MIN}=25 s^{-1}, and this value is determined by the electron diffusion coefficient and the film thickness.

On the other hand if the electron lifetime is shorter than the transit time d^2/D (here d is the film thickness and D the diffusion coefficient), a fraction of the photogenerated electrons will be lost in the transit. The effect of the back reaction on the transient and IMPS responses is evident in **Figure 3.13** where the electron lifetime (τ=10ms) is shorter than the transit time d^2/D=100 ms. The rise-time of the photocurrent is now shorter, as the transit distance has been reduced from the film thickness (10^{-3}cm) to the electron diffusion length $L_d=(D\tau)^{1/2}\approx 3\times10^{-4}$ cm. Electrons generated beyond L_d from the substrate are lost by back reaction with I_3^-. The effect of the decrease in the transit time is then twofold. Firstly the IMPS response shifts to higher frequencies (ω_{MIN}= 100s^{-1}), secondly the low frequency limit of $j_{photo}/q\delta I_0$ has decreased from 1.0 to 0.08. The spiral associated with the transit time is still evident.

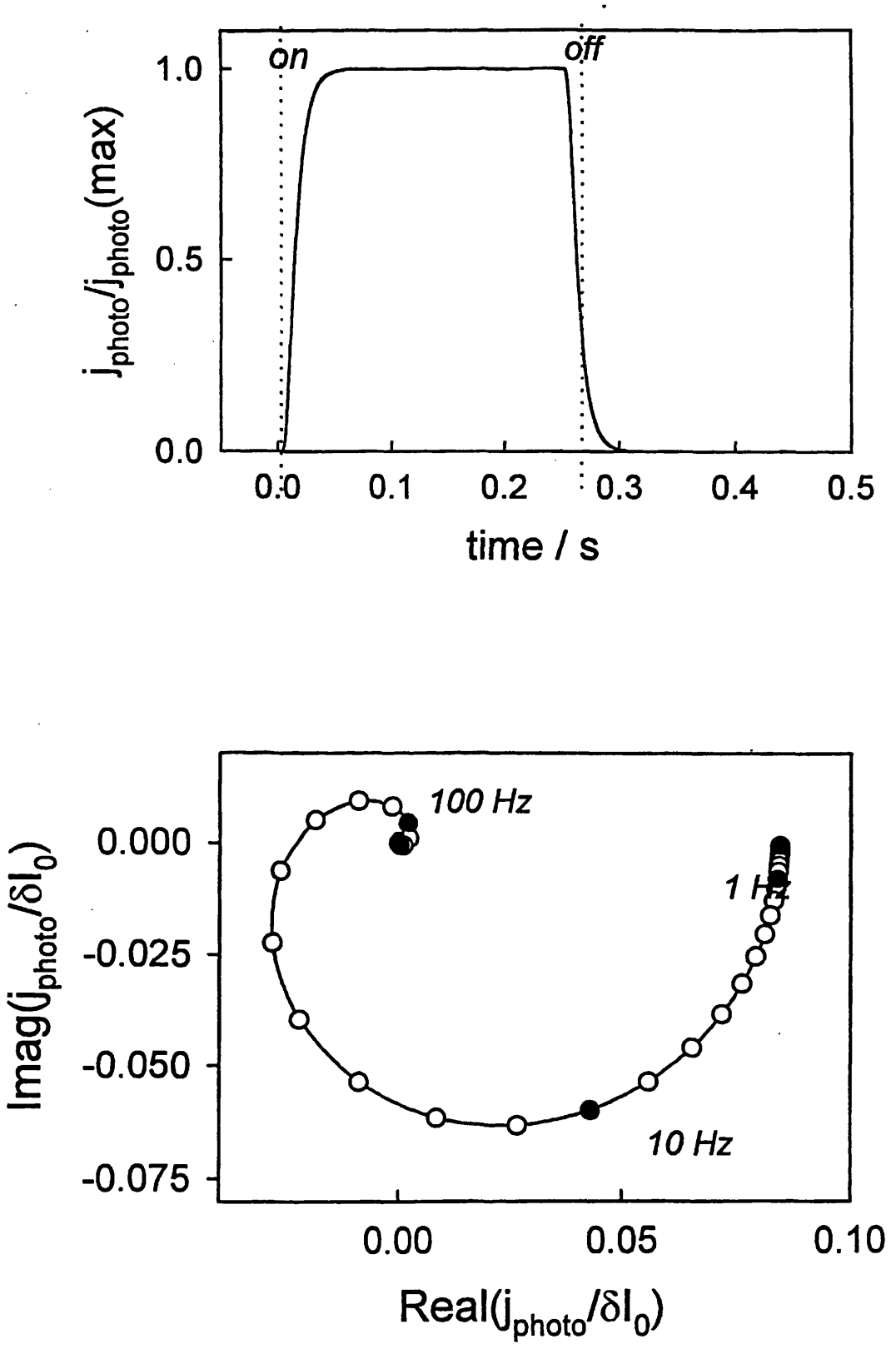

Figure 3.13. IMPS and photocurrent transients for illumination from the electrolyte side for α=10^5cm^{-1}, d=10^{-3}cm, D=10^{-5}cm^{2}s^{-1} and τ=10ms [25].

Consider the case of illumination from the substrate side for strongly absorbed light, i.e. band to band excitation of electron-hole pairs. In this case the electrons are generated close to the substrate, so that the transit distance becomes much smaller since now is of the order of $1/\alpha$ instead of L_d, the diffusion length. **Figure 3.14** shows the IMPS and transient response for illumination from the substrate side for the same values of the diffusion coefficient and electron lifetime as in **Figure 3.13**. The first feature to note in the IMPS plot is the absence of the high frequency spiral, meaning that there is no time lag. ω_{MIN} is now much higher as the electrons have a short distance to travel to reach the substrate. Such a big difference appears in between illumination from the electrolyte and substrate side because a high value of the absorption coefficient has been considered $10^5 cm^{-1}$. For smaller values of the absorption coefficient, the difference is no longer so evident as the thickness becomes comparable with the penetration depth.

The present discussion has neglected the RC time constant of the electrode, which can interfere with the IMPS response. In fact, the frequency dependent photocurrent measured in the external circuit is attenuated by the parallel combination of the electrode capacitance and the resistance. In general, the measured IMPS response Φ_{ext} takes the form:

$$\Phi_{ext}(\omega)=\Phi_{int}(\omega)A(\omega) \tag{3.58}$$

where

$$A(\omega)=\frac{1-i\omega RC}{1+\omega^2R^2C^2} \tag{3.59}$$

is the RC attenuation factor and $\Phi_{int}(\omega)$ is the photocurrent conversion efficiency defined by equations (3.51) and (3.57).

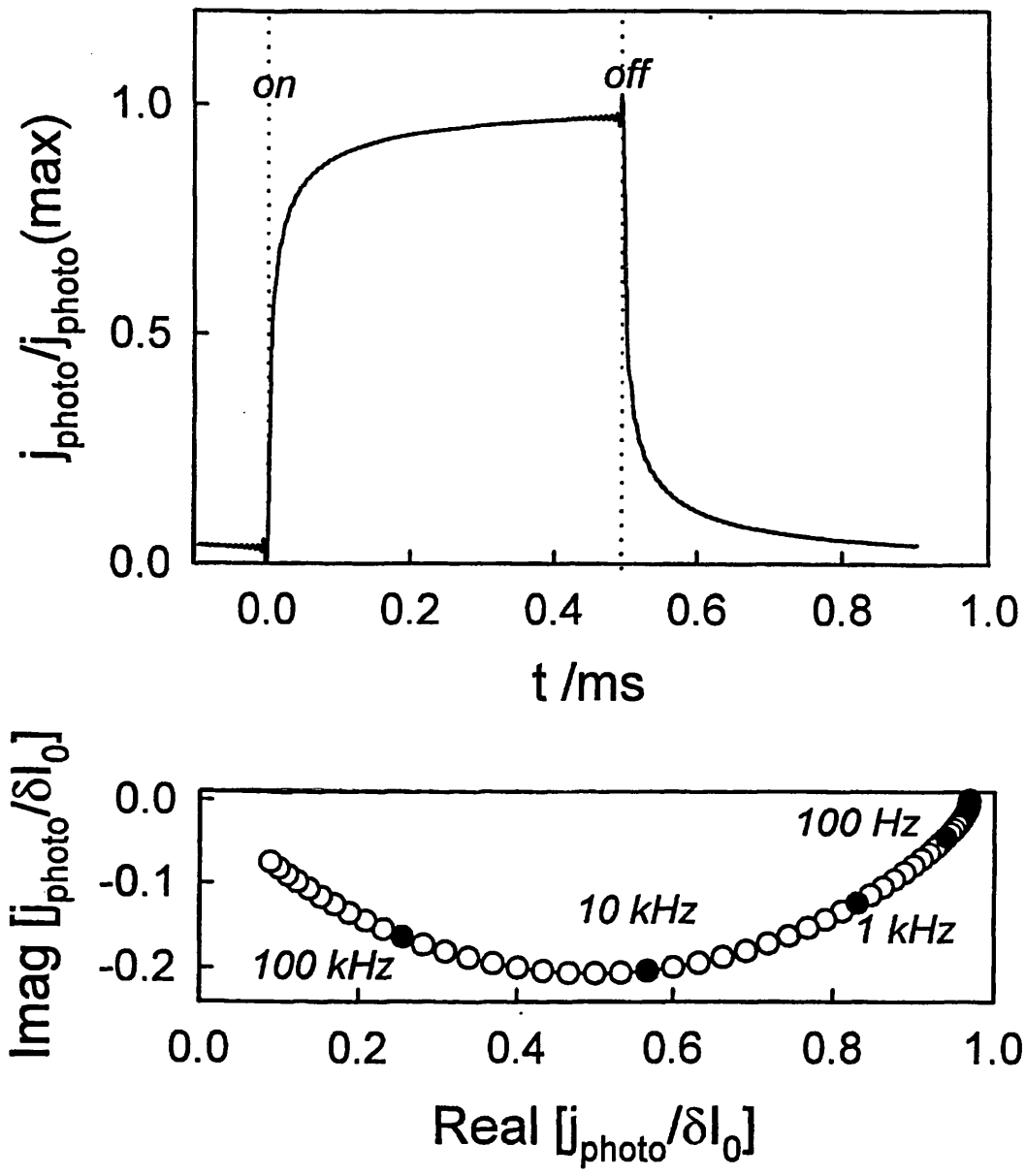

Figure 3.14. IMPS and photocurrent transients for illumination from the substrate side for the same parameters as **Figure 3.13** [25].

3.5.2 The Influence of Electron Trapping and Detrapping

So far the possibility of electron trapping and detrapping has been neglected. Electron trapping is represented by a first-order rate constant k_{trap} that depends on the thermal velocity of electrons as well as the capture cross-section, density and occupation of traps. k_{trap} is then expected to decrease as the electron traps are filled, for example by increasing the illumination intensity. The rate of release from the traps, or detrapping, is also characterised by a first-order rate constant k_{detrap}, which is determined by the trap depth and the temperature. The problem is simplified by considering that k_{trap} and k_{detrap} are not energy dependent [12]. This is a limiting approximation as k_{detrap} depends exponentially on the energy difference in between the energy of the band-gap state and the edge of the conduction band (see section 2.4.3). It is shown that this simplification constitutes a limit to explain some of the experimental results obtained in the present work. In principle k_{trap} and k_{detrap} are also distance-dependent due to the variation of the electron quasi-Fermi level across the film. In the present approach, for the sake of simplicity, k_{trap} and k_{detrap} are not considered to be distance-dependent.

Restricting to the case of illumination from the substrate side, equation (3.33) becomes:

$$\frac{\partial n(x,t)}{\partial t} = D\frac{\partial^2 n(x,t)}{\partial x^2} - \frac{n(x,t)}{\tau} - k_{trap}n(x,t) + k_{detrap}N(x,t) + \alpha I_0 e^{-\alpha x} e^{i\omega t} \quad (3.60)$$

Here $N(x,t)$ is the density of tapped electrons, τ is the lifetime for recombination with I_3^- of free electrons and the other symbols have the same meaning as above. The density of trapped electrons is given by:

$$\frac{\partial N(x,t)}{\partial t} = k_{trap}n(x,t) - k_{detrap}N(x,t) - \frac{N(x,t)}{\tau_{trap}} \quad (3.61)$$

Here τ_{trap} is the lifetime for recombination of trapped electrons with I_3^-.

The time-dependent electron concentration for free and trapped electrons is of the form:

$$n(x,t)=u(x)e^{i\omega t} \tag{3.62}$$

and

$$N(x,t)=v(x)e^{i\omega t} \tag{3.63}$$

Equation (3.61) then becomes:

$$v(x)=\frac{k_{trap}}{i\omega+k_{detrap}+\frac{1}{\tau_{trap}}}u(x) \tag{3.64}$$

Equation (3.60) can be written:

$$u''=\left(i\omega+\frac{1}{\tau}+k_{trap}-\frac{k_{trap}k_{detrap}}{i\omega+k_{detrap}+\frac{1}{\tau_{trap}}}\right)\frac{u(x)}{D}+\alpha I_0 e^{-\alpha x} \tag{3.65}$$

It follows that solutions of equation (3.60) are the same as the ones of equation (3.33) except that γ is now given by:

$$\gamma=\left(i\omega+\frac{1}{\tau}+k_{trap}-\frac{k_{trap}k_{detrap}}{i\omega+k_{detrap}+\frac{1}{\tau_{trap}}}\right)^{1/2} \tag{3.66}$$

Solutions of equation (3.61) can easily be found, as they are the same as equation (3.60) multiplied by the imaginary factor $k_{trap}/\left(i\omega+k_{detrap}+\tau_{trap}^{-1}\right)$.

If $k_{trap}, k_{detrap}>>\omega$, then original expressions are recovered with effective electron lifetime τ_{eff} and effective diffusion coefficient D_{eff} defined by:

$$\frac{1}{\tau_{eff}}=\frac{1}{\tau_{cb}}+\frac{k_{trap}}{1+k_{detrap}k_{trap}} \tag{3.67}$$

$$D_{eff}=\frac{D}{1+\frac{k_{trap}k_{detrap}}{\left(k_{detrap}+\frac{1}{\tau_{trap}}\right)^2}} \tag{3.68}$$

Figure 3.15 shows an IMPS plot where the effect of trapping and detrapping has been introduced. The processes of trapping and detrapping are distinguishable only if the rate constants k_{trap} and k_{detrap} are comparable with the modulation frequency, and in this case the IMPS response resolves into two parts as shown in **Figure 3.15**. At high frequencies the 45^0 slope typical of diffusion controlled transport can be noted.

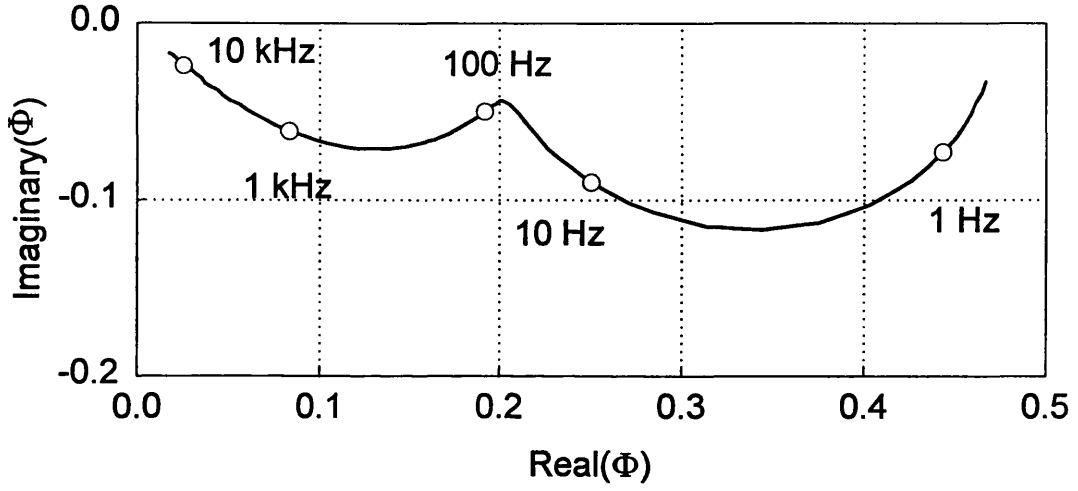

Figure 3.15. IMPS plot calculated from equation (3.60) for $\alpha=10^4 cm^{-1}$, $D=8\times10^{-7}cm^2s^{-1}$, $\tau=10ms$, $\tau_{trap}=\infty$, $d=10\mu m$, $k_{trap}=1000s^{-1}$ and $k_{detrap}=100s^{-1}$.

3.6 Photomodulated Infrared Transmittance Spectroscopy

In the general case the near infrared transmittance, T, detects electrons either in the conduction band or in the traps across the TiO_2 film thickness:

$$T=\frac{I_t}{I_0}=exp\left(-\int_0^d\left(\sigma_f(\lambda)n_f(x,t)+\sigma_t(\lambda)n_t(x,t)\right)dx\right) \tag{3.69}$$

here $n_f(x,t)$ and $n_t(x,t)$ are the position and time dependent densities of respectively free and trapped electrons, and $\sigma_f(\lambda)$ and $\sigma_t(\lambda)$ are the corresponding optical absorption cross sections at the wavelength λ. If the electron concentrations are perturbed from their

photostationary values by modulated illumination superimposed on a larger dc level, it can be shown that the ratio $\Delta T/T$ is given by:

$$\frac{\Delta T}{T} = -\int_0^d \left(\sigma_f(\lambda)\delta n_f(x) + \sigma_t(\lambda)\delta n_t(x)\right)dx \tag{3.70}$$

where $\delta n_f(x)$ and $\delta n_t(x)$ are the photo-induced perturbations of free and trapped electron densities respectively and ΔT is the resulting change in transmittance. The term on the right can be obtained integrating equation (3.52) across the film thickness. Under open circuit conditions, i.e. k_{ext}=0, the total (modulated) number of free electrons is then given by:

$$\int_0^d \delta n_f(x,t)dx = \frac{\eta(V)\delta I_0\left(1-e^{-\alpha d}\right)}{\frac{1}{\tau}+i\omega} \tag{3.71}$$

Under open circuit conditions the total (modulated) number of trapped electrons can be obtained combining equations (3.64) and (3.71), it follows that:

$$\int_0^d \delta n_t(x,t)dx = \frac{\eta(V)\delta I_0\left(1-e^{-\alpha d}\right)}{\frac{1}{\tau}+i\omega}\frac{k_{trap}}{k_{detrap}+\frac{1}{\tau_{trap}}+i\omega} \tag{3.72}$$

Analogous expressions for the total number of modulated electrons can be derived under short circuit conditions, i.e. k_{ext} very large. For free electrons the integral of equation (3.52) for k_{ext} very large is given by:

$$\int_0^d \delta n_f(x,t)dx = \frac{\eta(V)\delta I_0}{D}\frac{1}{\alpha+\gamma}\frac{\gamma-(\alpha+\gamma)e^{-\alpha d}+2\frac{\alpha}{\gamma-\alpha}\frac{\gamma e^{-\gamma d}-\alpha e^{-\alpha d}}{e^{\gamma d}+e^{-\gamma d}}}{\gamma^2} \tag{3.73}$$

The total modulated number of trapped electrons at short circuit is given by:

$$\int_0^d \delta n_t(x,t)dx = \frac{\eta(V)\delta I_0}{D}\frac{1}{\alpha+\gamma}\frac{\gamma-(\alpha+\gamma)e^{-\alpha d}+2\frac{\alpha}{\gamma-\alpha}\frac{\gamma e^{-\gamma d}-\alpha e^{-\alpha d}}{e^{\gamma d}+e^{-\gamma d}}}{\gamma^2}\frac{k_{trap}}{k_{detrap}+\frac{1}{\tau_{trap}}+i\omega} \tag{3.74}$$

Figure 3.16 compares the integrated modulated density responses for free electrons calculated from equations (3.71) and (3.73) for typical values of the electron diffusion coefficient and electron lifetime. Two features can be noted. The first is that the low frequency limit of the integral of electron densities is predicted to be much lower at short than at open circuit. This is expected because the steady state electron density at short circuit is determined by the rates of generation and collection. On the other hand at open circuit the steady state electron density is determined by the rates of generation and back reaction with I_3^-. The difference in the steady state densities then follows from the fact that the electron lifetime, τ, is larger than the diffusion time τ_D. The second feature is that the frequency at which the minima in the plots occur are not identical because the relaxation processes are different in the two cases. Under short circuit conditions, the relaxation occurs by diffusion to the substrate (average time constant τ_D), whereas at open circuit relaxation is dominated by the back reaction with I_3^-. The higher value of the frequency minimum at short circuit shows that the diffusion time is shorter then the electron lifetime, $\tau_D < \tau$.

Figure 3.17 shows the frequency dependence of the integrated densities for free and trapped electrons under short and open circuit conditions (equations (3.71), (3.72), (3.73) and (3.74)). It is worth noting that under short circuit conditions for free electrons the relaxation is due to diffusion.

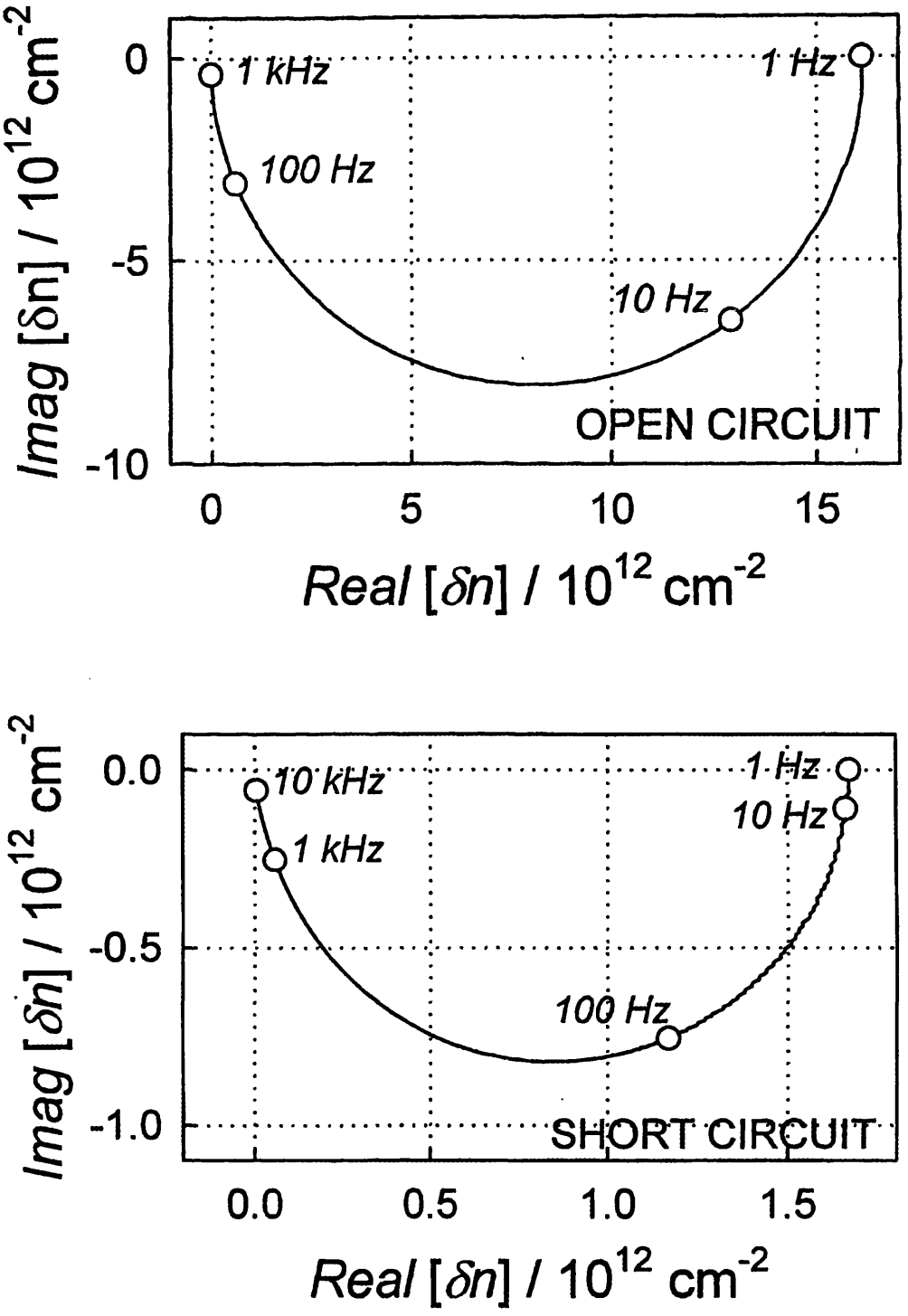

Figure 3.16. Complex plane plots of the integrated density of free electrons calculated from equations (3.71) and (3.73) at open circuit and short circuit I_0=6.5×10^{15}cm^{-2}s^{-1}, α=1375cm^{-1}, d=2.7μm, τ=8ms, D=2.8 ×10^{-5}cm^{2}s^{-1} and $\eta(V_{OC})$=1.

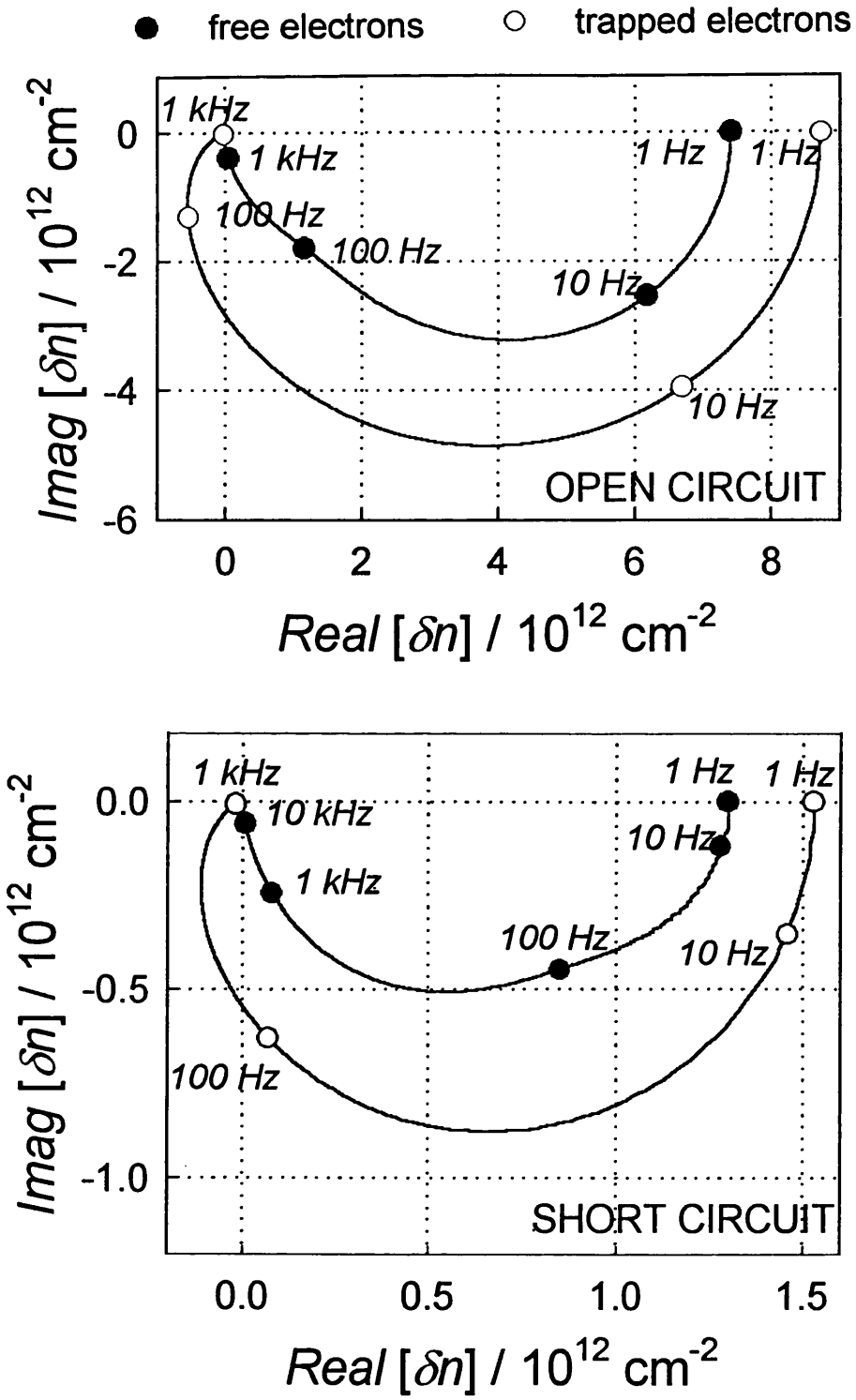

Figure 3.17. Complex plane plots of the integrated density of free and trapped electrons calculated from equations (3.71), (3.72), (3.73) and (3.74) at open circuit and short circuit I_0=6.5×10^{15}cm^{-2}s^{-1}, α=1375cm^{-1}, d=2.7μm, τ=8ms, D=2.8 ×10^{-5}cm^{2}s^{-1}, τ_{trap}=8ms, k_{trap}=300s^{-1}, k_{detrap}=500s^{-1} and $\eta(V_{OC})$=1.

[11] P. E. de Jongh and D. Vanmaekelbergh, J. Phys. Chem. B, 101, 2716, (1997).

[12] L. Dloczik, O. Ileperuma, I. Lauermann, L. M. Peter, E. A. Ponomarev, G. Redmond, N. J. Shaw and I. Uhlendorf, J. Phys. Chem. B, 101, 10281, (1997).

[13] E. Kamieniecki, J. Vac. Sci. Technol., 20, 811, (1982).

[14] E. Kamieniecki, J. Appl. Phys., 54, 6481, (1983).

[15] G. Schlichthörl and H. Tributsch, Electrochim. Acta, 37, 919, (1992).

[16] G. Franco, J. Gehring, L. M. Peter E. A. Ponomarev and I. Uhlendorf, J. Phys. Chem. B, 103, 692, (1999).

[17] A. Solbrand, H. Lindström, H. Rensmo, A. Hagfeldt, S. E. Linquist and S. Södergen, J. Phys. Chem. B, 101, 2514, (1997).

[18] F. Cao, G. Oskam, G. J. Meyer and P. C. Searson, J. Phys. Chem., 100, 17021, (1996).

[19] L. M. Peter, Chem. Rev., 90, 753, (1990).

[20] G. Schlichthörl, S. Y. Huang, J. Sprague and A. J. Frank, J. Phys. Chem. B, 101, 8141, (1997).

[21] S. A. Haque, Y. Tachibana, D. R. Klug and J. R. Durrant, J. Phys. Chem. B, 102, 1745, (1998).

[22] R. de Levie, Electrochim. Acta, 8, 751, (1963).

[23] R. de Levie, Electrochim. Acta, 9, 1231, (1964).

[24] S. Södergren, A. Hagfeldt, J. Olsson and S.-E. Lindquist, J. Phys. Chem., 98, 5552, (1994).

[25] L.M. Peter, E. A. Ponomarev, G. Franco and N. J. Shaw, Electrochim. Acta, submitted for publication.

3.7 Conclusion

Ac techniques have been introduced in this chapter. It has been shown that electrochemical systems are not linear, but they can be made linear using small ac perturbation superimposed on dc backgrounds. IMVS, IMPS and PITS are the modulated response of photovoltage, photocurrent and transmittance when an ac light perturbation is superimposed onto a large dc background. Impedance is determined by the ratio of the perturbing ac voltage superimposed on a larger dc background to the ac component of the total current. It will be shown in subsequent chapters that all these ac techniques are powerful tool for understanding electron transport in dye-sensitised nanocrystalline solar cells and porous electrodes in general.

3.8 References

[1] D. D. MacDonald, 'Transient Techniques in Electrochemistry', Plenum, New York, (1977).

[2] G. Gabrielli, 'Identification of elecrochemical processes by frequency response analysis', Technical report No 004/83. Solatron Instrument, UK, (1980).

[3] J. R. Macdonald (Editor), 'Impedance Spectroscopy emphasising solid materials and systems', Wiley, New York, (1987).

[4] P. Allongue and H. Cachet, J. Electroanal. Chem., 119, 371, (1981).

[5] J. Schefold and H. M. Kühne, J. Electroanal. Chem., 300, 211, (1991).

[6] F. Cardon and D. Vanmaekelbergh, Electrochim. Acta, 37, 837, (1992).

[7] J. Schefold, J. Electrochem. Soc., 142, 850, (1995).

[8] W. P. Gomes and D. Vanmaekelbergh, Electrocim. Acta, 41, 967, (1996).

[9] E. A. Ponomarev and L. M. Peter, J. Electroanal. Chem., 397, 45, (1995).

[10] P. E. de Jongh and D. Vanmaekelbergh, Phys. Rev. Lett., 77, 3427, (1996).

CHAPTER IV

EXPERIMENTAL METHODS

4.1 Introduction

As discussed in chapter II, nanoporous systems have attracted great scientific interest in the last decade. Nanoporous electrodes are finding application in a wide range of novel devices such as dye-sensitised photovoltaic cells [1], photonic crystals [2] and electrochromic windows [3]. In the present work, dye-sensitised and dye-free TiO_2 nanocrystalline electrodes were studied using frequency-resolved techniques. The combination of these techniques is a powerful tool to analyse electron transport in these systems. It has been shown [4,5] that nanocrystalline structures exhibit non-linear photocurrent responses as discussed in section 3.2. This suggests linearisation of the system using small amplitude signals. This is achieved for IMPS [6,7], IMVS [8] and PITS [9] measurements by superimposing a small light modulation on a much larger dc illumination intensity. In the case of impedance measurements, linearisation is obtained by superimposing a small voltage perturbation on a much larger dc voltage.

This chapter presents the methods used to prepare dye-sensitised and dye-free TiO_2 nanocrystalline electrodes. Additionally, frequency-resolved techniques are described, as they are the main tool used in this work to characterise electron transport in nanoporous electrodes.

4.2 Preparation of the Samples

4.2.1 Dye-Sensitised TiO_2 Nanocrystalline Photovoltaic Cells

The dye-sensitised TiO_2 cells [1] used in this study were obtained from the Institut für Angewandte Photovoltaik (INAP). They were prepared following the methods described by Nazeeruddin et al. [10]. The electrolyte was composed of methyl-hexylimidazolium iodide (MHImI), iodine, tert-butylpyridine and acetonitrile. MHImI was prepared according to the method given by Papageorgiou et al. [11]. Iodine was purchased by Fluka and used without further purification. Acetonitrile and *tert*-butylpyridine was also purchased from Fluka and distilled under nitrogen before use.

Nanoporous TiO_2 layers were prepared from a colloidal TiO_2 dispersion obtained by hydrolysis of titanium isopropoxide. The preparation method of O'Regan and Grätzel [1] was modified to yield only anatase. The colloidal dispersions were dried and the powders ground with pine oil until a smooth dispersion was obtained, which was then screen printed on conducting glass plate (TEC 8, fluorine-doped SnO_2 on 3 mm float glass purchased from Libby Owens Ford). The film was fired in air at 450^0C. The TiO_2 films were dipped in a 3×10^{-4}M solution of the ruthenium dye *cis*-di(thiocyanato)-N,N-bis(2,2'-dicarboxylate)ruthenium(II) in ethanol for 2 hours. A sandwich cell was prepared with a second transparent platinum modified conductive glass plate, and both plates were glued together with transparent poly(ethylene) (PE) hot melt. The electrolyte was introduced through holes drilled in the back electrode, and these were subsequently sealed with microscope cover plates and PE hot melt.

The resulting geometry of the cell is illustrated in **Figure 4.1**. The thickness of the TiO_2 layer is typically around 10 microns. The cell is normally illuminated from the substrate side. However, if the platinum counter electrode is transparent, the sample can be illuminated from the electrolyte side.

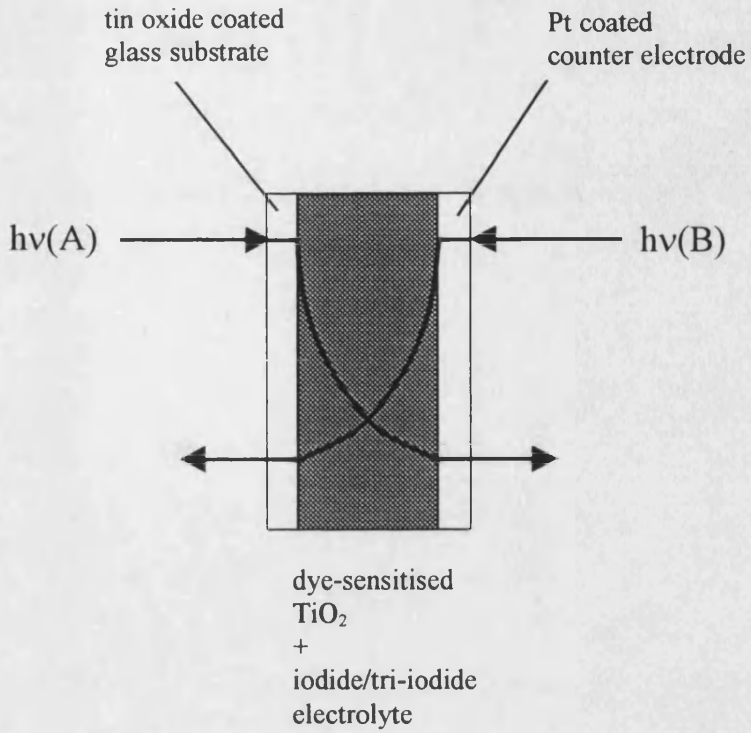

Figure 4.1. Structure of a sealed thin layer dye-sensitised TiO_2 cell. Illumination is normally incident from the substrate. The platinum coated counter electrode can be transparent, allowing illumination from the electrolyte side.

4.2.2 Dye-Free TiO_2 Nanocrystalline Cells

The TiO_2 colloidal suspension was prepared following the method described by Zaban et al. [12]. A volume of 1.5mL of titanium (IV) isopropoxide (Aldrich, 99.9%) in 0.4mL of 2-propanol was added drop-wise into a stirred mixture of 3.2mL glacial acetic acid and 10mL of deionized water at 0^0C. The resulting solution was heated at 80^0C for 8 hours. It was then heated at 230^0C for 12 hours in a titanium autoclave (Parr General purpose acid digestion bomb, Model No.4744). Upon removal from the autoclave, the solution was sonicated for 5 min with a cell disrupter with approximate power of 250 W (KERRY 250 W ultrasonicator). The solution was then concentrated to 150g/L in a rotary evaporator. Finally 0.16g of Carbowax 20000 (Riedel-de-Haen) was added and it

was stirred overnight.

Small conductive glass substrates, $2.0\times1.5cm^2$, (Libby Owens Ford, 10 ohms/square SnO_2) were cleaned by overnight immersion in a solution of KOH in 2-propanol, rinsed with deionized water, and dried in an air stream. The TiO_2 colloid was then spread over the substrate with a glass rod using adhesive tape to define the thickness. The dimension of the TiO_2 film were $0.4\times0.8cm^2$. The films were fired at 450^0C for 45 min in air, resulting in an almost transparent 3μm thick film. In order to reduce the series resistance, the glass surrounding the film was coated with sputter-deposited platinum (Agar Sputter coater). **Figure 4.2** shows an SEM cross section of the film, which was used to evaluate the film thickness (2.9μm).

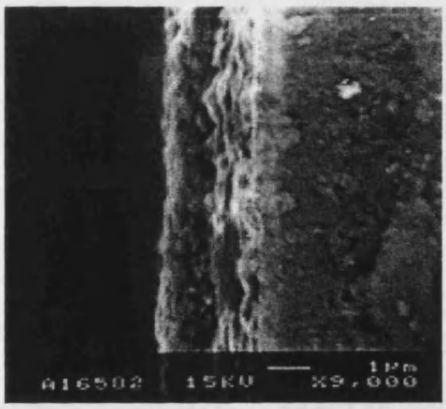

Figure 4.2. SEM image of the cross section of the TiO_2 nanocrystalline film deposited on a conducting glass sheet (on the right). The thickness of the film is 2.9 μm.

The film was sandwiched with another piece of conductive glass, cleaned as above, with a thin transparent layer of sputtered platinum (Agar Sputter coater). The tin oxide and the platinum layers were removed in the middle with a diamond scribe, in order to provide a three-electrode cell, then both plates were glued together with a transparent polyethylene (PE) hot melt. A saturated solution of LiI in acetonitrile was introduced through holes drilled in the back electrode, and these were subsequently

sealed with microscope cover plates and PE hot melt. Traces of I_3^- were present in solution, therefore the redox couple I^-/I_3^- was used as a reference electrode.

4.3 Intensity Modulated Photocurrent Spectroscopy

For IMPS measurements, the sample is illuminated by a dc light source as well as an ac source, such as a light emitting diode (LED) or a laser, that provides a smaller intensity modulated illumination flux. LEDs are very convenient as they can be driven directly by the sinusoidal voltage output of the frequency response generator through an appropriate series resistor. Lasers can also be used in combination with an acousto-optic modulator. Generally the ac component is less than 20% of the dc photon flux in order to linearise the system. The frequency of the modulated component of the light varies over a wide range, typically $1\text{-}10^4$ Hz. The amplitude and the phase shift of the outcoming photocurrent are measured via the frequency-resolved analyser. For dye-sensitised solar cells described in section 4.2.1 the potentiostat is operated in two-electrode mode by shorting the counter and the reference electrode terminals.

In the present work, IMPS measurements have been performed using three different kinds of light sources. Dye-sensitised solar cells were illuminated using a visible source such as a blue light emitting diode (LED) or the 514nm line of the argon ion laser. For dye-free TiO_2 nanocrystalline cells, IMPS measurements were carried out using UV illumination from a cadmium helium laser.

For the results presented in chapter V, low-intensity modulated illumination from a blue light emitting diode (LED: λ_{max} 460 nm) superimposed on constant illumination from a tungsten halogen lamp was used. The intensity of the modulated light was limited to about 1% of the dc light level to ensure linear response. A Solartron 1250 frequency response analyser (FRA) was used to drive the LED and analyse the

photocurrent response. The cell voltage was controlled by a fast potentiostat operating in two-terminal mode [6,13]. Alternatively instead of the LED the 514 nm line of the argon ion laser [9] was used to perform the IMPS measurements presented in chapter VI on dye-sensitised solar cells. The intensity of the laser beam was modulated using an Isomet acousto-optic modulator driven by a Solartron 1250 frequency response analyser [14]. A microscope slide was used as beam splitter and a fast Liconix photodiode was used to provide a reference signal for the FRA. In this way the photocurrent was corrected for the time delay introduced by the acousto-optic modulator. The maximum incident power was 14mW, and the peak to peak modulation depth was 18%. The laser beam was expanded to illuminate an area of $0.8cm^2$.

For dye-free TiO_2 nanocrystalline cells, the light source was the 325nm line of a cadmium helium laser [15]. The intensity of the laser beam was modulated using an Opto-Electronique acousto-optic modulator driven by a Solartron 1250 frequency response analyzer. The cell voltage was controlled by a fast potentiostat operating in three-terminal mode. A quartz sheet beam splitter and a fast Liconix photodiode provided a reference signal for the FRA. The maximum incident power was 0.95mW and the peak to peak modulation depth was 13%. The laser beam was expanded to illuminate an area of $0.3cm^2$.

Figures 4.3(a) and **4.3(b)** show the set-up used for IMPS measurements using both the LED and the laser. With the laser, the acousto-optic modulator and the beam splitter are indispensable. The beam splitter is essential as it corrects for the time delay introduced by the acousto-optic modulator.

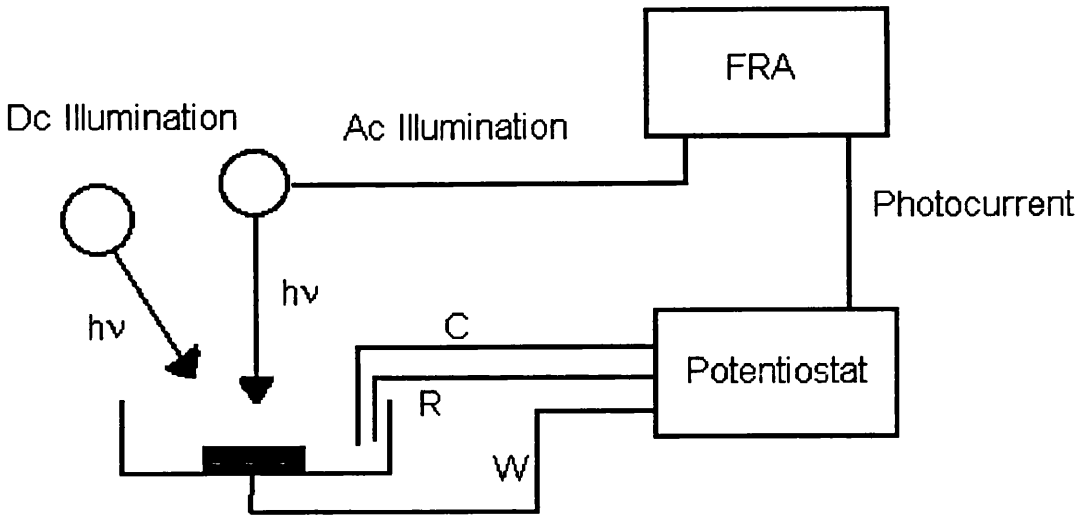

Figure 4.3(a). Experimental arrangement used for IMPS measurements. The light emitting diode (LED) is driven by a sinusoidal current output from the frequency response analyser. A second light source provides constant illumination. The frequency response analyser measures the magnitude and the phase shift in the photocurrent with respect to the modulated illumination.

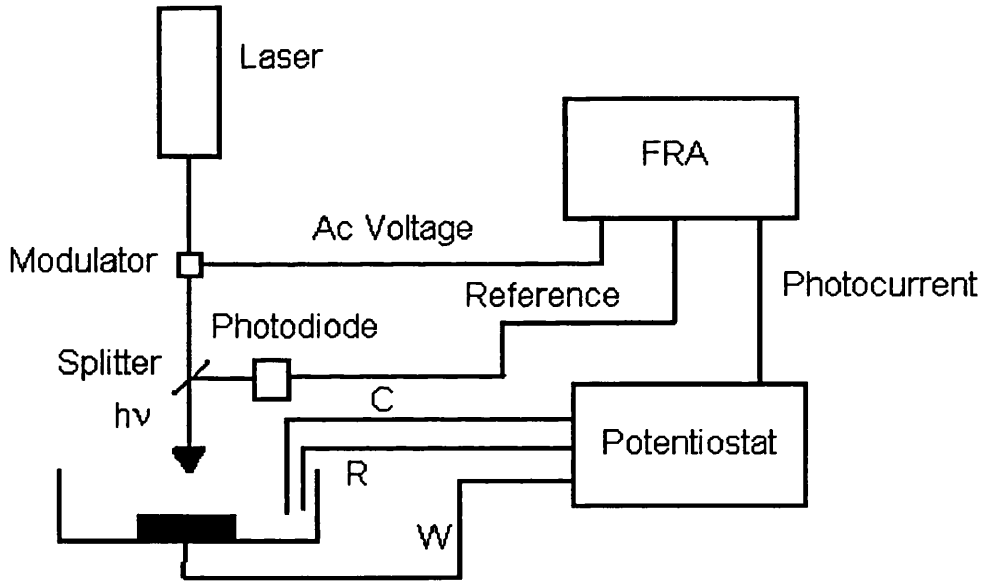

Figure 4.3(b). Experimental arrangement used for IMPS measurements. The light source is a laser whose light intensity is modulated by a modulator. The amplitude of the sinusoidal signal is typically 15% of the constant illumination of the laser. The beam splitter and the photodiode are introduced to correct for the time delay introduced by the acousto-optic modulator.

4.4 Intensity Modulated Photovoltage Spectroscopy

Photovoltage [9] measurements were performed using the same set-up as for IMPS measurements, except that the potentiostat was replaced by a high-impedance low-noise preamplifier (Stanford model SR560). **Figure 4.4** shows a typical photovoltage set-up. The light source is the same as the one used for the related IMPS measurements.

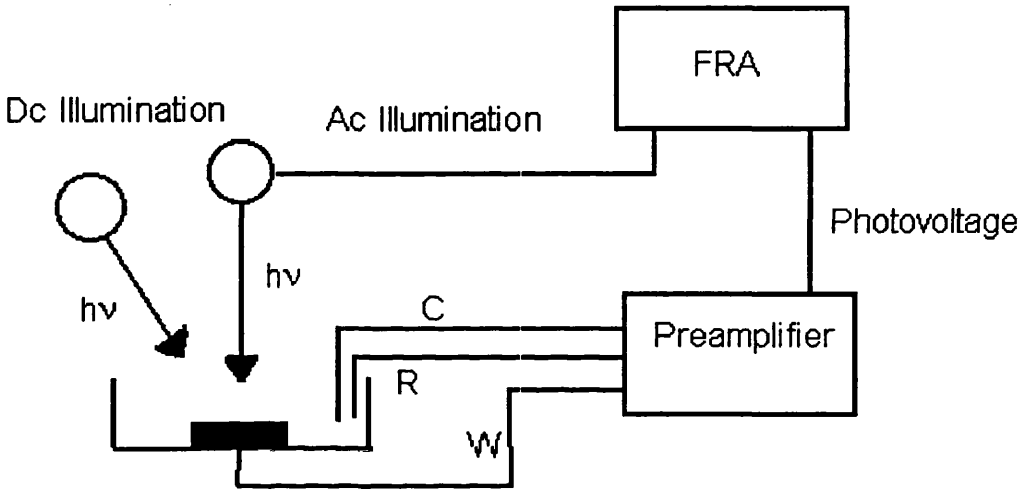

Figure 4.4. Experimental arrangement for IMVS measurements. The light source shown in this figure is an LED with a dc background illumination, however the light source can also be a laser. If the laser is used as illumination source the modulator, the beam splitter and the photodiode must be introduced.

4.5 Photoelectrochemical/Electrochemical Impedance Spectroscopy

To evaluate the attenuation factor [6] introduced in section 3.5.1, the glass sheet resistance, R, and the electrode capacitance, C, are calculated from the short circuit impedance measured using a Solartron 1250 frequency response analyser and a Solartron 1286 interface. Impedance measurements were performed both in the dark and under illumination. In the latter case, the illumination intensity was adjusted to give the

same dc short circuit current as measured in the IMPS experiments. Impedance was measured using a perturbation of 10mV about the open circuit voltage of the cell. **Figure 4.5** illustrates the impedance set-up.

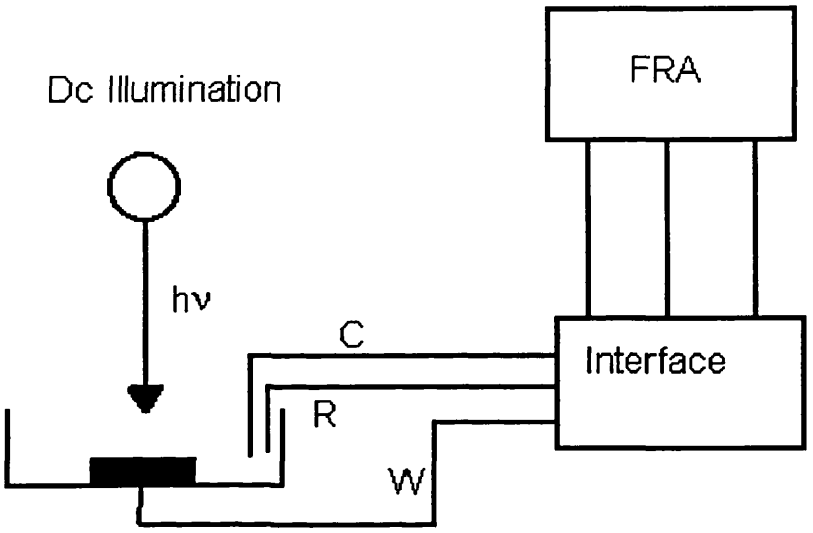

Figure 4.5. Impedance measurements can be performed in the dark and under illumination. Under illumination, impedance measurements are performed under the same light illumination conditions (i.e. same dc short circuit photocurrent) as used in the related experiments such as IMPS, IMVS, etc.

4.6 Photomodulated Infrared Transmittance Spectroscopy

The cell was illuminated from the substrate side with the argon ion laser modulated by an Isomet acousto-optic modulator. The beam splitter and the Liconix fast photodiode provided the reference signal. The transmittance of the cell was measured at 940nm using a Kodenshi GaAs (OPE5594) light emitting diode (LED) source and a Sharp silicon (PD481PI) diode detector with a built-in IR filter that eliminated stray light from the laser beam. The wavelength was chosen to lie beyond the absorption bands of the dye and of I_3^-, as described in section 7.3. The source and detector were

mounted slightly off axis relative to the laser beam, so that the transmittance was measured in the illuminated area. The periodic component of the cell transmittance was measured by the frequency response analyser. For the short circuit modulated transmittance measurements, the voltage of the cell was controlled by a potentiostat operating in two-electrode mode. Open circuit photomodulated transmittance measurements were performed with no external connections to the cell. The measured photomodulated transmittance [9] signal ΔT was divided by the dc transmittance T to give the dimensionless complex quantity $\Delta T/T$, which was plotted in the complex plane. **Figure 4.6** shows the set-up used for photomodulated infrared transmittance measurements.

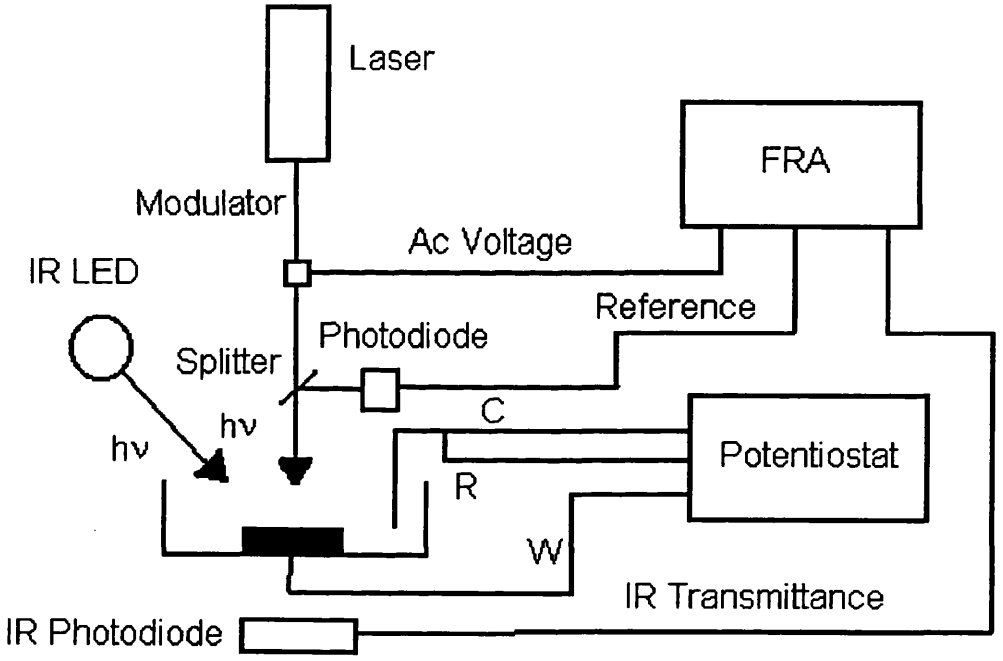

Figure 4.6. Photomodulated infrared transmittance spectroscopy set-up. The potentiostat is used only when performing short circuit measurements. For open circuit measurements the cell is not connected to the potentiostat. Note the beam splitter and photodiode when the laser is used.

4.7 Dc Current-Voltage Measurements

Dc current-voltage measurements were performed on both dye-sensitised nanocrystalline TiO_2 cells and dye-free TiO_2 nanoparticulate cells. For the former cells, the potentiostat was used in two-electrode mode, for the latter in three-electrode mode. The outcoming current was plotted on an X-Y recorder. Dc current-voltage experiments were performed under illumination and in the dark. For measurements under illumination the intensity level used was the same as the related PITS, IMPS,PEIS and IMVS measurements.

4.8 Potential-Modulated Infrared Transmittance

The TiO_2 nanocrystalline cell was connected to a potentiostat operating in three-electrode mode and a modulated voltage was applied using a Solartron 1250 frequency response analyzer. The ac voltage was 25mV and different values of the bias voltage were applied. The transmittance of the cell was measured at 940nm using Kodenshi GaAs (OPE5594) light emitting diode (LED) source and a Sharp silicon (PD481PI) diode detector with a built-in IR filter. The signal was amplified using a high-impedance low-noise preamplifier (Stanford model SR560). The measured transmittance signal ΔT was divided by the dc transmittance to give the dimensionless complex quantity $\Delta T/T$, which was plotted in the complex plane. A typical experimental set-up for potential-modulated infrared transmittance is shown in **Figure 4.7**.

Dc transmittance experiments at 940 nm were also carried out as function of the dc bias. The set-up used was a potentiostat connected to the three-electrode cell and to a PPR1 function generator. The dc transmission was measured as function of the bias applied and the result was plotted on an X-Y recorder.

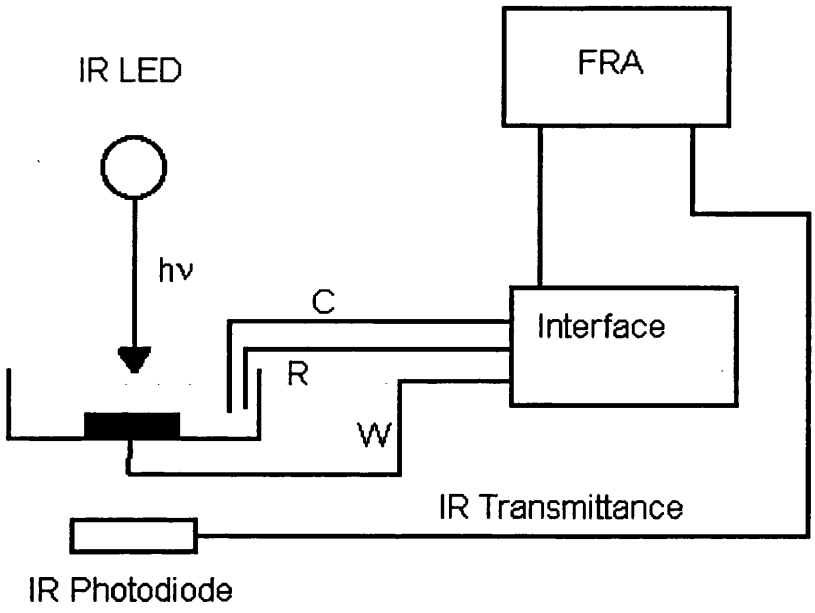

Figure 4.7. Experimental set-up for potential-modulated infrared transmittance in the dark. The experiment was performed in accumulation as function of the dc applied bias.

4.9 References

[1] B. O'Regan and M. Grätzel, Nature, 353, 737, (1991).

[2] J. D. Joannopoulos, P. R. Villeneuve and S. Fan, Nature, 386, 143, (1997) and references therein.

[3] C. G. Granquist, 'Handbook of Inorganic Electrochromic Materials', Elsevier, Amsterdam, (1995).

[4] A. Solbrand, H. Linström, H. Rensmo, A. Hagfeldt, S.-E. Lindquist and S. Södergren, J. Phys. Chem. B, 101, 2514, (1997).

[5] F. Cao, G. Oskam, G. J. Meyer and P. C. Searson, J. Phys. Chem., 100, 17021, (1996).

[6] L. Dloczik, O. Ileperuma, I. Lauermann, L. M. Peter, E. A. Ponomarev, G. Redmond, N. J. Shaw and I.Uhlendorf, J. Phys. Chem. B, 101, 10281, (1997).

[7] P. E. de Jongh and D. Vanmaekelbergh, J. Phys. Chem. B, 101, 2716, (1997).

[8] G. Schlichthörl, S. Y. Huang, J. Sprague and A. Frank, J. Phys. Chem. B, 101, 8141, (1997).

[9] G. Franco, J. Gehring, L. M. Peter, E. A. Ponomarev and I. Uhlendhorf, J. Phys. Chem. B, 103, 692, (1999).

[10] M. K. Nazeeruddin, A. Kay, I. Rodicio, R. Hunphry-Baker, E. Muller, P. Liska, N. Valchopoulos and M. Grätzel, J. Am. Chem. Soc., 115, 6328, (1993).

[11] N. Papageorgiou, Y. Athanassov, M. Armand, P. Bonhote, H. Petterson, A. Azam and M. Grätzel, J. Electrochem. Soc., 143, 3099, (1996).

[12] A. Zaban, S. Ferrere, J. Sprague and B. A. Gregg, J. Phys. Chem., 101, 55, (1997).

[13] G. Franco, L. M. Peter and E. A. Ponomarev, Electrochem. Comm., 1, 61, (1999).

[14] L. M. Peter, Chem. Rev., 90, 753, (1990).

[15] G. Franco, L. M. Peter and K. G. Upul Wijayantha, in preparation.

CHAPTER V

INTENSITY MODULATED PHOTOCURRENT SPECTROSCOPY

5.1 Introduction

As discussed in section 3.5.1, the IMPS response for illumination from the substrate side is expected to lie in the 4th quadrant of the complex plot (positive real + negative imaginary). However the experimental IMPS response of dye-sensitised solar cells for illumination from the substrate side crosses the real axis at high frequencies. This anomaly is also observed in dye-free TiO_2 films for illumination from the substrate side [1,2]. This means that electrons take longer than expected to reach the substrate, introducing a time delay in the IMPS response that results in the crossing of the real axis at high frequency.

It is shown [3] that this time delay can be attributed to the fact that the absorption coefficient, α, and the net injection efficiency, η, in the generation term, $\delta I_0 \eta \alpha e^{-\alpha x}$, in equation (2.19) are distance-dependent. The simplest approximation is to consider that in a portion of the film the generation term is present, and it tends to zero in the remaining part of the film. This new approach to the generation/collection problem is named 'dead layer' model. The nature of the 'dead layer' is different for dye-free and dye-sensitised TiO_2 nanocrystalline electrodes, but their IMPS responses can be analysed with the same theoretical approach.

5.2 Theory

The IMPS response was derived in section 3.5.1. A typical complex plane IMPS plot for illumination from the substrate side is shown in **Figure 5.1**. The attenuation factor, $A(\omega)$, is also considered in order to introduce the RC time constant of the nanocrystalline electrode. The influence of RC is illustrated in **Figure 5.1**.

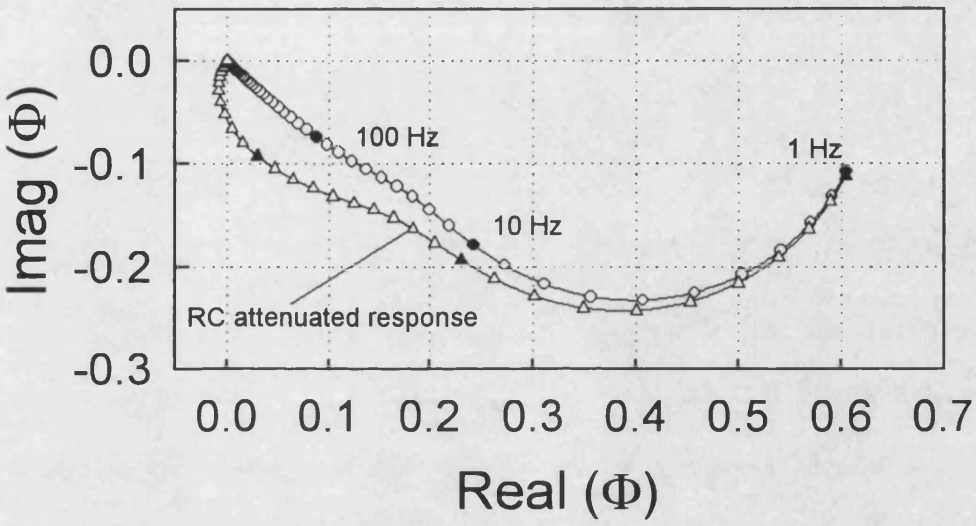

Figure 5.1. Complex plane IMPS plots calculated for homogeneous dye distribution and diffusion controlled electron collection (equation (3.51)) at the substrate under short circuit conditions for d=7.5μm, D=10^{-5}cm^{2}s^{-1}, η=1, τ=50ms and α=3000cm^{-1}. The lower curve illustrates the effect of the RC attenuation at high frequencies (equation (3.59)) for R=10Ω and C=10^{-4}F.

So far IMPS has been modelled assuming that α and η in the generation term of equation (2.19) are not distance-dependent. Now the film is divided in region I and II, one of thickness d_1 where the generation term is zero (α=0 or η=0), and the other of thickness d_2 where photogeneration (or photoinjection) takes place, so that $d_1+d_2=d$ (total film thickness). The presence of the 'dead layer' introduces a delay, d_1^2/D, in the collection of electrons generated in the region $d_1<x<d$. This time delay in the IMPS plot manifests as a frequency dependent phase shift.

Two different generation/collection equations must be considered for region I and II. Continuity of the solutions must obviously be attained at the interface between region

I and II. In the present approach only illumination from the substrate side is considered.

The diffusion equation for the electrons in region I, where no generation takes place, is:

$$\frac{\partial n}{\partial t} = D\frac{\partial^2 n}{\partial x^2} - \frac{n}{\tau} \tag{5.1}$$

here D is the diffusion coefficient and τ is the electron lifetime. The boundary condition for x=0 is:

$$n(0,t)k_{ext} = D\left(\frac{\partial n}{\partial x}\right)\Big|_{x=0} \tag{5.2}$$

where k_{ext} is the rate constant of electron extraction at the interface TiO_2/substrate, as described in section 3.5.1.

Using the same approach as in section 3.5.1, equation (5.1) can be rewritten:

$$u'' = \gamma^2 u \tag{5.3}$$

The solution of equation (5.3) is:

$$u(x) = A\left(e^{\gamma x} - \frac{1-\frac{\gamma D}{k_{ext}}}{1+\frac{\gamma D}{k_{ext}}}e^{-\gamma x}\right) \tag{5.4}$$

The current through the external circuit is then given by:

$$j_{photo} = D\left(\frac{\partial n}{\partial x}\right)\Big|_{x=0} = 2A\gamma D\frac{1}{1+\frac{\gamma D}{k_{ext}}} \tag{5.5}$$

The diffusion equation for electrons in part II is:

$$\frac{\partial n}{\partial t} = D\frac{\partial^2 n}{\partial x^2} - \frac{n}{\tau} + \eta\alpha I_0 e^{-\alpha(x-d_1)}e^{i\omega t} \tag{5.6}$$

Solution of equation (5.6) can be found of the form:

$$u(x) = Ce^{\gamma x} + Ee^{-\gamma x} + Fe^{-\alpha x} \tag{5.7}$$

where:

$$F = \frac{I_0}{D}\frac{\alpha}{\gamma^2 - \alpha^2}e^{\alpha d_1} \tag{5.8}$$

Coefficients A,C, and E can be derived from the following boundary conditions:

$$\left.\frac{\partial u}{\partial x}\right|_{x=d} = 0 \tag{5.9}$$

$n(x=d_1,t)$ and $\frac{\partial n}{\partial x}(x = d_1,t)$ must be the same at the interface of region I and II. The normalised IMPS response is then given by:

$$\Phi(\omega) = \frac{\eta\alpha}{\alpha+\gamma}\frac{e^{\gamma(d-d_1)} + e^{\gamma(d_1-d)} - 2\dfrac{\alpha e^{-\alpha(d-d_1)} - \gamma e^{\gamma(d_1-d)}}{\alpha-\gamma}}{e^{\gamma d} + e^{-\gamma d} + \dfrac{\gamma D}{k_{ext}}\left(e^{\gamma d} - e^{-\gamma d}\right)} \tag{5.10}$$

it follows that the diffusion controlled limit (large k_{ext}) is given by:

$$\Phi(\omega) = \frac{\eta\alpha}{\alpha+\gamma}\frac{e^{\gamma(d-d_1)} + e^{\gamma(d_1-d)} - 2\dfrac{\alpha e^{-\alpha(d-d_1)} - \gamma e^{\gamma(d_1-d)}}{\alpha-\gamma}}{e^{\gamma d} + e^{-\gamma d}} \tag{5.11}$$

If d_1=0 the expression of the photocurrent becomes the same found in equations (3.50) and (3.51).

For illumination from the electrolyte side, the same treatment applies replacing in the exponent of the generation term of equation (5.6) x-d_1 with d-x. However, for illumination from the electrolyte side the 'dead layer' has no effect as it is hidden by the delay electrons already have when travelling from the far end of the film.

Figure 5.2 illustrates the effect that the dead layer is predicted to have on the normalised IMPS response. As the width of the dead layer increases, the IMPS response moves further into the negative real + negative imaginary quadrant at high frequencies. As consequence, the frequency at which the IMPS response crosses the imaginary axis is lower for wider dead layers. These changes reflect the increasing delay in the transfer of electrons from the generation region defined by $d>x>d_1$.

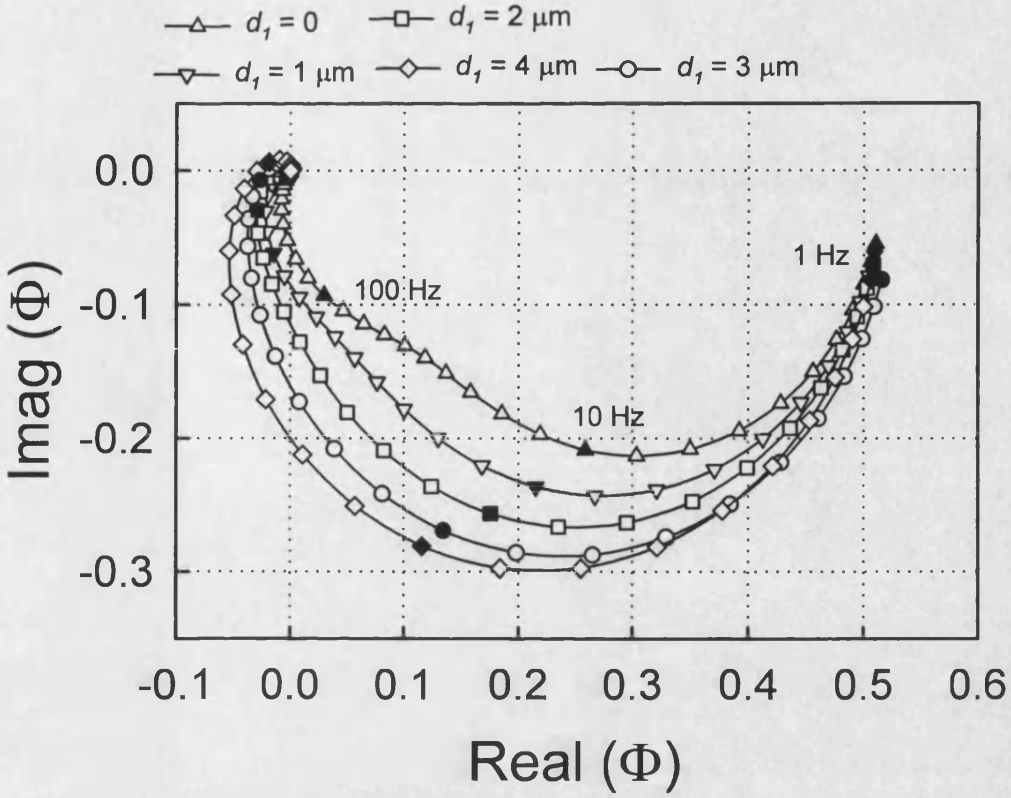

Figure 5.2. Illustration of the effect of the presence of a dye-free layer (equation (5.11)) on the complex plane IMPS response for d=7.5μm, α=10^3cm^{-1}, η=1, $\tau\rightarrow\infty$, D=10^{-5}cm^{2}s^{-1}, R=10 Ω, C=10^{-4} F and d_1 as shown. Note that the introduction of the delay time associated with the transport of electrons across the dead layer causes the plots to cross the imaginary axis and loop back to the origin.

5.3 Experimental Section

5.3.1 Dye-Sensitised Nanocrystalline TiO_2 Cells

The two dye-sensitised TiO_2 cells [4] used in this study were obtained from the Institut für Angewandte Photovoltaik (INAP). They were prepared following the methods described by Nazeeruddin et al. [5]; the cell construction and the electrolyte composition have been described in detail elsewhere [6]. The thickness of the TiO_2 layer of both cells was 7.3 microns with a surface area of 3.3cm^2. The freshly prepared TiO_2 films were dipped in 3×10^{-4}M solution of the ruthenium dye cis-di(thiocyanato)-N,N-bis(2,2'-dicarboxylate)ruthenium(II) in ethanol and either left overnight (cell A) or removed after an hour (cell B). The cells were then assembled as described in section

4.2.1.

IMPS measurements were carried out as described in section 4.3 using a low-intensity modulated illumination from a blue light emitting diode (LED: λ_{max} 460 nm) superimposed on constant illumination from a tungsten halogen lamp.

R and *C* were calculated from the short circuit impedance measured using a Solartron 1250 FRA and 1286 interface. The illumination intensity was adjusted to give the same dc short circuit current as measured in the IMPS experiments. The value of *R* was identical for the two cells; it corresponds to the resistance of the tin oxide. The photocapacitance values of the cells A and B were also identical and correspond to the capacitance of the underlying tin oxide substrate (about $30\mu Fcm^{-2}$). These values were used to calculate the *RC* attenuation using equation (3.59).

5.3.2 Dye-Free Nanocrystalline TiO_2 Cells

The sample used for IMPS measurements was a sandwich cell with a TiO_2 film. The preparation of the TiO_2 was described in section 4.2.2. The dimension of the TiO_2 film were $0.4\times0.8cm^2$ and the film thickness was 2.9μm (**Figure 4.2**).

The cell was illuminated from the electrolyte and substrate side with the 325nm line of a cadmium helium laser. The maximum incident power was 0.95mW. However, after the glass sheet, the light intensity was reduced to 0.11mW for illumination from the substrate side. For illumination from the electrolyte side, because of the thin platinum layer, the light intensity was only 0.08mW. All the experiments were performed at 0V vs. I^-/I_3^- (see **Figure 5.7**), which corresponds to the photocurrent saturation region. The short circuit current of the cell was measured and used to calculate the photocurrent conversion efficiency. The conversion efficiency obtained for illumination from the substrate side was 0.51, whilst for illumination from the

electrolyte side was 0.1. Both values agree with the photocurrent conversion efficiency calculated from the low frequency intercept of the modulated photocurrent response.

Photovoltage measurements were carried by connecting the cell to the frequency response analyzer via a high-impedance low-noise preamplifier (Stanford model SR569). These measurements showed that the electron lifetime is very long, indicating that a low concentration of I_3^- is present in solution.

Impedance measurements were performed under the same illumination conditions as the IMPS using a Solartron 1286 interface and a Solartron 1250 frequency response analyzer. The values obtained for R is 11Ω and for C is 2×10^{-6}F, no difference was observed for R and C for the two different sides of illumination.

5.4 Results and Discussion

5.4.1 Dye-Sensitised Nanocrystalline TiO_2 Cells

If the dye does not penetrate uniformly across the film, the electron generation rate in the region close to the substrate may be much lower than in the bulk. This non-homogeneous dye distribution across the film forms a 'dead layer' which introduces a time delay in the collection of photoinjected electrons. Thus an excursion of the IMPS response into the third quadrant of the complex plot at high frequencies is observed. On the other hand, if the dye load is uniform across the cell the IMPS response lies in the 4^{th} quadrant. To model this non-homogeneous dye distribution the cell should be considered as a series of lamina, each with a different dye concentration. The simplest case is the two-lamina model, i.e. the dye only penetrates partially into the film, leaving a dye-free, 'dead layer', adjacent to the substrate. The two-layer model considers a uniform dye layer of thickness d_1 on top of a dye-free layer of thickness d_2, where $d_1+d_2=d$ (the total film thickness). The dye profile is represented by a step function;

Figure 5.3 shows the dye and the light absorption profiles for the two-lamina model. The model can be extended to multiple layers with different dye loading. In the present section the three-lamina model is also developed but only a marginal improvement is obtained fitting the experimental data.

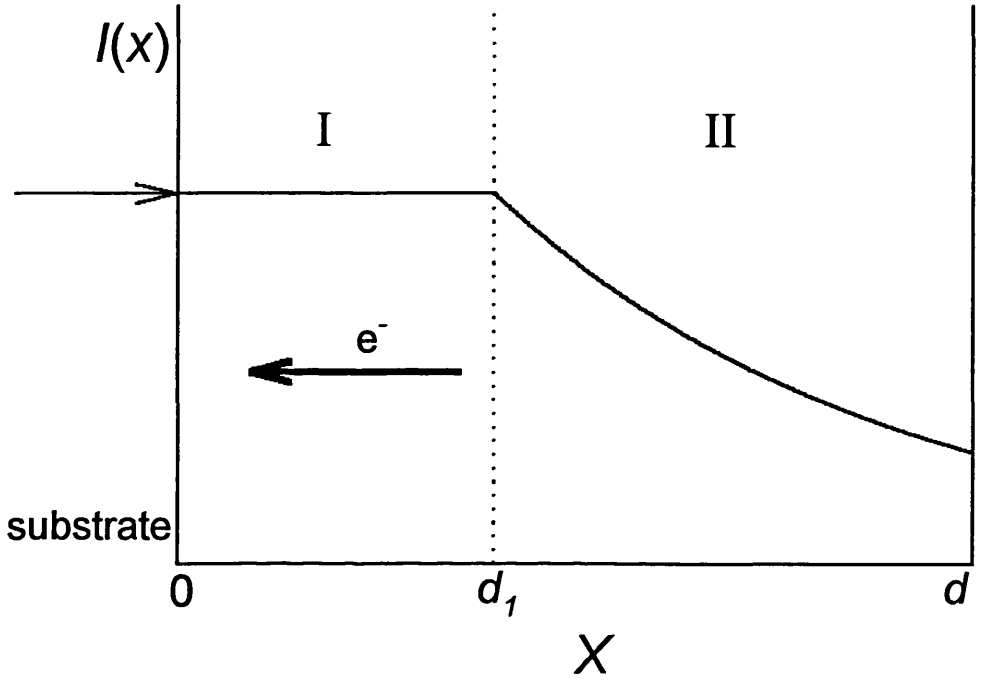

Figure 5.3. Light absorption profile for the two-layer model. For simplicity it is assumed that the dye loading is a step function. Note that electrons generated in the region $d_1<x<d$ experience a time delay in the collection at the substrate since they must diffuse across the dye-free layer. The corresponding transit time is d_1^2/D.

As shown in **Figure 5.3** the dye concentration changes from zero to β:

$$\beta = \alpha \frac{d}{d - d_1} \tag{5.12}$$

where α is the average concentration of the dye across the whole layer. Under this assumption the change of the dead layer size d_1 will not affect the overall absorption of the film. Equations (5.10) and (5.11) then become:

$$\Phi(\omega) = \frac{\eta\beta}{\beta+\gamma} \frac{e^{\gamma(d-d_1)} + e^{\gamma(d_1-d)} - 2\dfrac{\beta e^{-\alpha d} - \gamma e^{\gamma(d_1-d)}}{\beta-\gamma}}{e^{\gamma d} + e^{-\gamma d} + \dfrac{\gamma D}{k_{ext}}\left(e^{\gamma d} - e^{-\gamma d}\right)} \tag{5.13}$$

$$\Phi(\omega)=\frac{\eta\beta}{\beta+\gamma}\frac{e^{\gamma(d-d_1)}+e^{\gamma(d_1-d)}-2\dfrac{\beta e^{-\alpha d}-\gamma e^{\gamma(d_1-d)}}{\beta-\gamma}}{e^{\gamma d}+e^{-\gamma d}} \tag{5.14}$$

If d_1=0 and α=β then equations (5.13) and (5.14) become the same found in section 3.5.1 (equation (3.50) and (3.51)). Under short circuit conditions it is assumed that η is equal to unity.

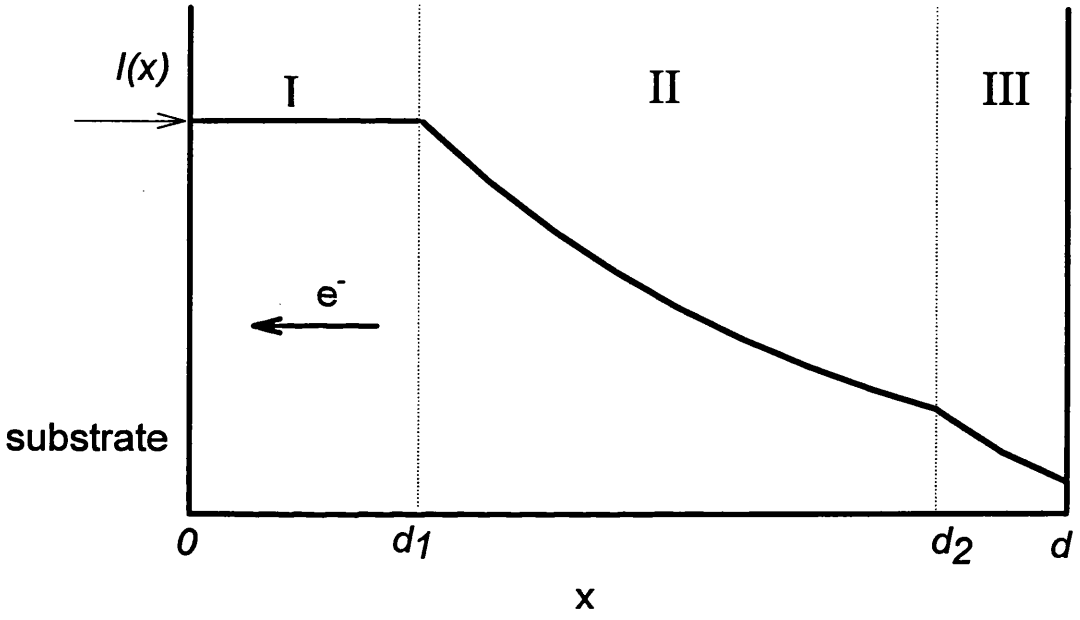

Figure 5.4. Light absorption profile in the three-lamina model, each lamina has a different dye loading, i.e. $\beta_2>\beta_1$. No effective improvement in fitting the IMPS plots was observed with the three-lamina model.

The two-lamina model can be extended to a multiple layer-model, each layer with increasing absorption coefficients $\beta_1<\beta_2<\beta_3$. In **Figure 5.4** it is shown the three-lamina case, where the film is divided in three regions: one with no dye, one with a lower concentration of dye and one with a higher concentration. To solve the three-lamina case the same equations and boundary conditions as above can be used, adding the continuity at the second interface. This means that $n(x=d_2,t)$ and $\frac{\partial n}{\partial x}(x=d_2,t)$ must be the same at the interface of region II and III. As for the two-lamina case the total

absorption of the cell must be invariant and if α is the average concentration then it must be held the equation:

$$\alpha d = \beta_1(d_2 - d_1) + \beta_2(d - d_2) \tag{5.15}$$

here β_1 and β_2 are the absorption coefficients of region II and III and d, d_1 and d_2 are shown in **Figure 5.4**. Although the three-lamina model was developed, no real improvement in fitting the experimental data was observed compared with the two-lamina model.

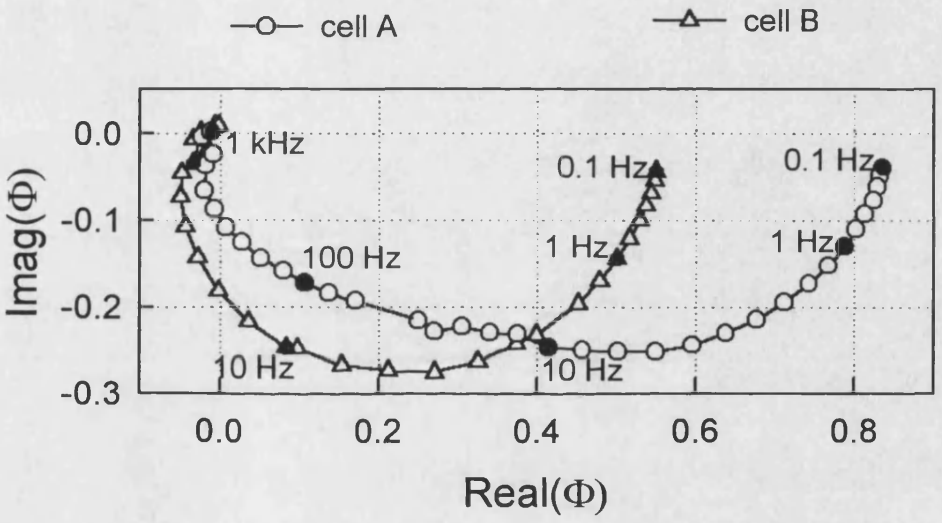

Figure 5.5. Complex plane IMPS plots for cell A (long impregnation) and for cell B (short impregnation). Note that the IMPS plot for cell B crosses the imaginary axis at much lower frequencies than the plot for cell A before curving back to the origin. The dc photocurrent for cell A is 21μAcm^{-2} and for cell B 11.5μAcm^{-2}.

Figure 5.5 compares the IMPS response obtained for cells A (long impregnation) and B (short impregnation). It can be seen that the response of cell B loops much further into the III quadrant (negative real + negative imaginary) of the complex plot. At the same time, the low frequency intercept of the IMPS response is higher for cell A than for cell B, indicating that cell A has a higher incident photon to current conversion efficiency (IPCE). The dc photocurrent for cell A is 21μAcm^{-2} and for cell B is

11.5μAcm^{-2}. The *RC* attenuation does not explain such a substantial difference in the IMPS response of the two cells because the values of *R* and *C* are similar. The fact that the IPCE of cell B is lower than cell A, in spite of the fact that the thickness of the TiO_2 layer is the same, suggests that the dye loading is lower in cell B (short impregnation).

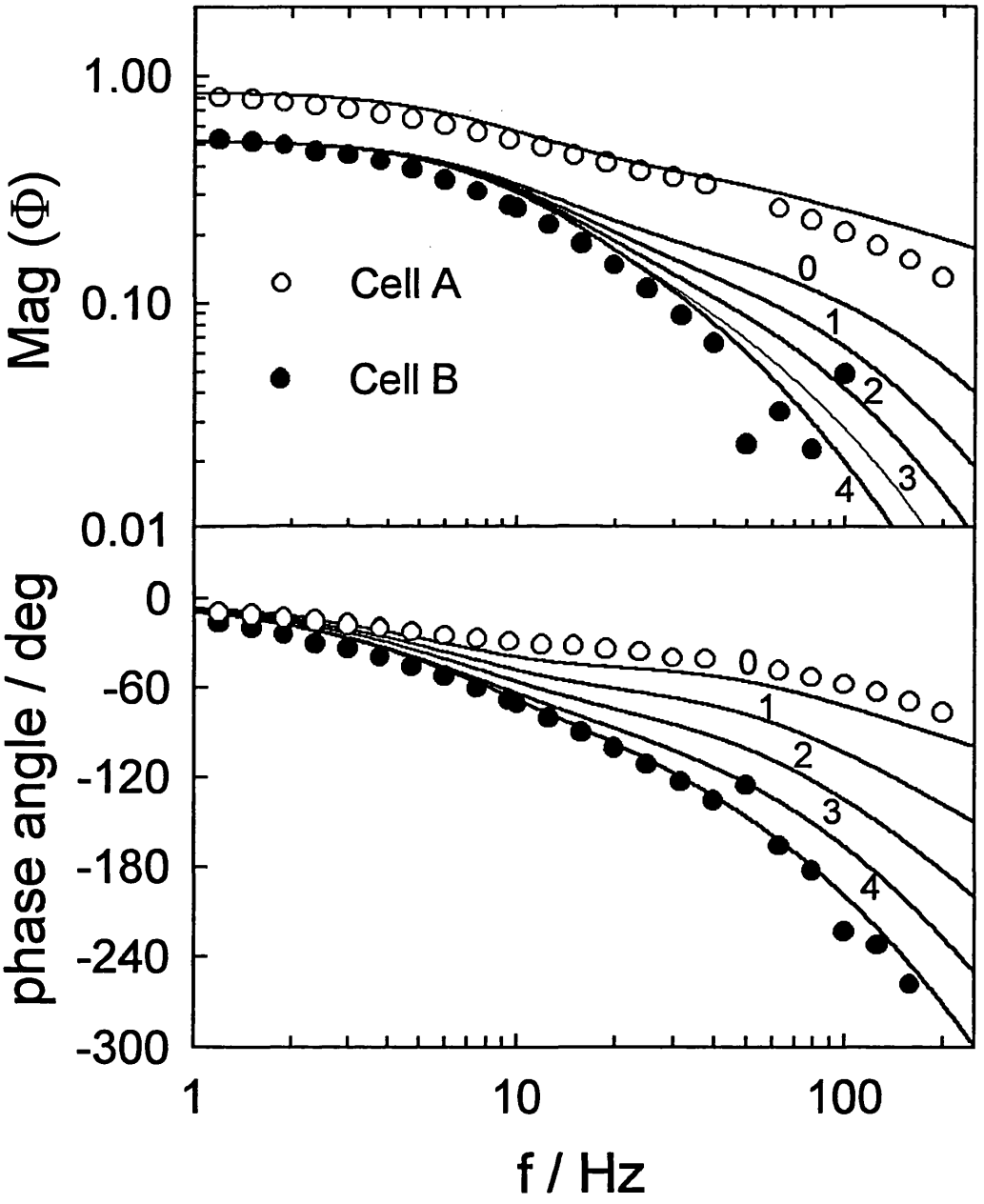

Figure 5.6. Bode plots comparing the IMPS responses of cells A and B with fits to the homogeneous model (cell A) and to the two-layer inhomogeneous model (cell B). Fitting values for cell A: d=7.5μm, α=2.5×10^{3}cm^{-1}, η=1, $\tau\rightarrow\infty$, D=10^{-5}cm^{2}s^{-1}, R=10Ω and C=10^{-4}F. Values used to generate plots for comparison with the results for cell B: d=7.5μm, α=1.2×10^{3}cm^{-1}, η=1, $\tau\rightarrow\infty$, D=10^{-5}cm^2 s^{-1}, R=10Ω, C=10^{-4}F and d_1 as shown. A good fit is obtained for d_1=4μm, indicating that more than half of the TiO_2 film is dye-free. Note the large phase shift for cell B compared with cell A.

The experimental data for cell A was fitted by assuming that the dye distribution was uniform across the cell thickness (equation (3.51)). The response of cell B was instead fitted using the model for inhomogeneous dye distribution, i.e. two-layer model (equation (5.14)). In both cases the *RC* attenuation was calculated using impedance measurements (rounded to 10^{-3} s). The influence of the 'dead layer' becomes apparent in the phase angle bode plot, as illustrated in **Figure 5.6**. For cell B the phase angle reaches higher values than cell A because of the delay introduced by the dead layer. The best fit was obtained for a dead layer thickness of 3.8μm, which is nearly half the film thickness. This result is a clear evidence of the presence of an inhomogeneous dye loading. It is worth noting that for both cells the absorption coefficients obtained from the fittings were in good agreement with the values measured directly by transmission spectroscopy.

5.4.2 Dye-Free Nanocrystalline TiO_2 Cells

Figure 5.7 shows the steady state photocurrent as function of the applied voltage for illumination from the substrate and electrolyte side for a dye-free TiO_2 porous electrode. Up to -0.4V the photocurrent is constant for both illumination from the substrate and electrolyte side. The photocurrent conversion efficiency for illumination from the substrate side is higher compared with illumination from the electrolyte side. This is attributed to the fact that the porosity of the film is not uniform across the film. On the electrolyte side the film is likely to be more porous than it is on the substrate side, therefore the absorption coefficient, which is proportional to the porosity, is not constant across the film thickness. This will obviously affect the photocurrent conversion efficiency shown in **Figure 5.7**.

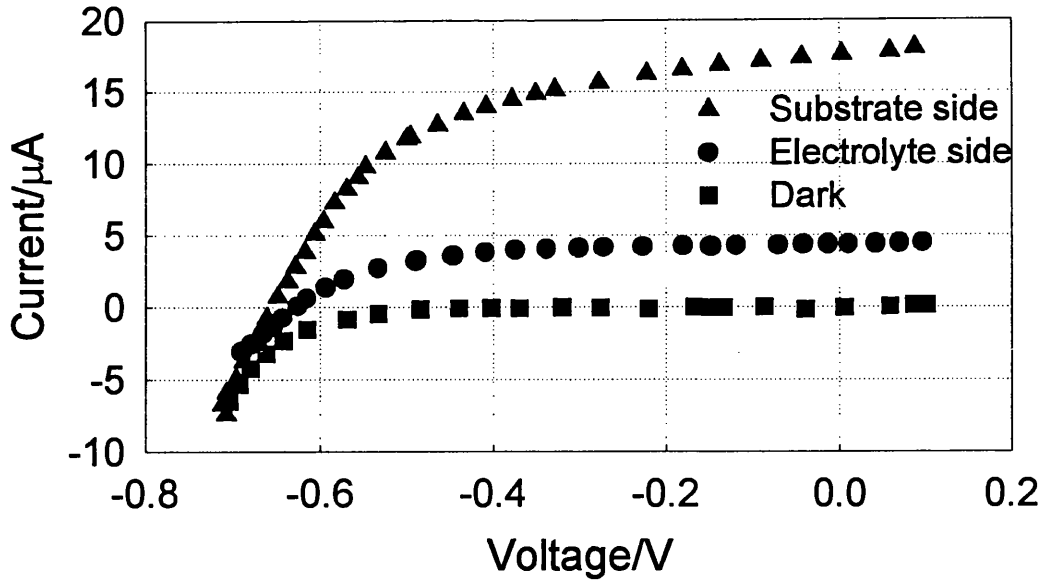

Figure 5.7. Plot of the steady state photocurrent of the particulate TiO_2 electrode as function of the applied potential. The electrode is illuminated from the electrolyte (lower curve) and substrate side (higher curve) with UV light. The difference in the photocurrent conversion efficiency for illumination from the substrate and electrolyte side is attributed to a different morphology of the TiO_2 film.

Section 3.5.1 discusses the simulation of the IMPS response for illumination from the substrate and electrolyte side for high absorption coefficients ($10^5 cm^{-1}$). It was observed in the simulations that for illumination from the substrate side ω_{MIN} in the IMPS response is very high, of the order of 10kHz. This is due to the fact that electrons are generated near the substrate and therefore have a short distance to travel. For illumination from the electrolyte side, the diffusion time is longer. This means that ω_{MIN} in the IMPS plot is expected to be lower, typically about 10 Hz, compared with illumination from the substrate side. The other feature for illumination from the electrolyte side is the spiral at high frequencies typical for a constant time lag, and it arises simply from the transit time required for carriers to move from the front face to the rear contact.

The difference in the IMPS response for illumination from the substrate and electrolyte side is marked only if the penetration depth of the light is smaller than the

film thickness, i.e. $\alpha d>>1$, where α is the absorption coefficient of TiO_2 and d is the film thickness. This condition is held in the present experiment as the absorption coefficient of TiO_2 at 325 nm is 2×10^5 cm^{-1} [7], and assuming an average porosity of 50% it lowers to $10^5 cm^{-1}$, which remains greater than d^{-1}.

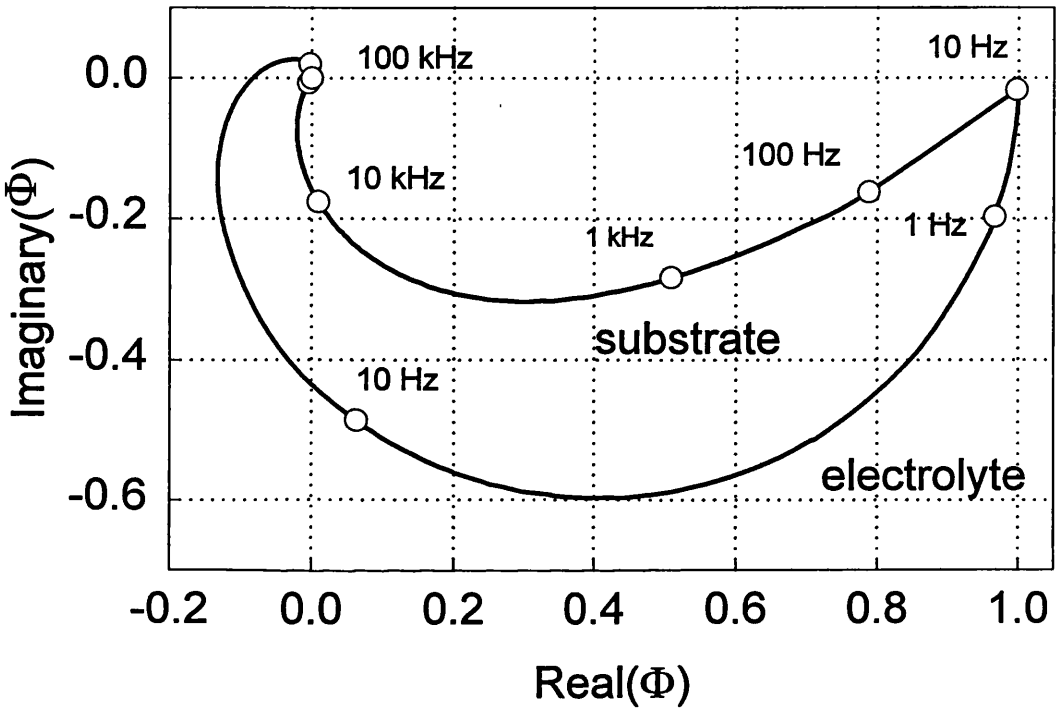

Figure 5.8. IMPS plot calculated from equation (3.51) and (3.57) for illumination from the substrate and electrolyte side for d=2.9μm, $\alpha=10^5 cm^{-1}$, $\tau\rightarrow\infty$, $D=10^{-6}cm^2s^{-1}$, R=11Ω and $C=2\times10^{-6}$F.

Figure 5.8, 5.9(a) and **5.9(b)** show the IMPS responses predicted by equations (3.51) and (3.57) including the *RC* attenuation (equation (3.59)) for illumination from the substrate and electrolyte side for d=2.9μm, $\alpha=10^5 cm^{-1}$, $\tau\rightarrow\infty$, $D=10^{-6}cm^2$ s^{-1}, R=11Ω and $C=2\times10^{-6}$F. For illumination from the substrate side the value found for ω_{MIN} is 17kHz, which is determined by the absorption and the diffusion coefficient. However the *RC* attenuation must be considered therefore the determination of ω_{MIN} is not straight forward. At high frequency the phase angle limiting value is 135^0, which is

given by the sum of the diffusion controlled characteristic slope of 45^0 and the *RC* attenuation limiting value of 90^0. For illumination from the electrolyte side (**Figure 5.8**) ω_{MIN} is about 30Hz and it is determined by the film thickness and the diffusion coefficient. The spiral associated with the transit time hides the effect due to the *RC* attenuation.

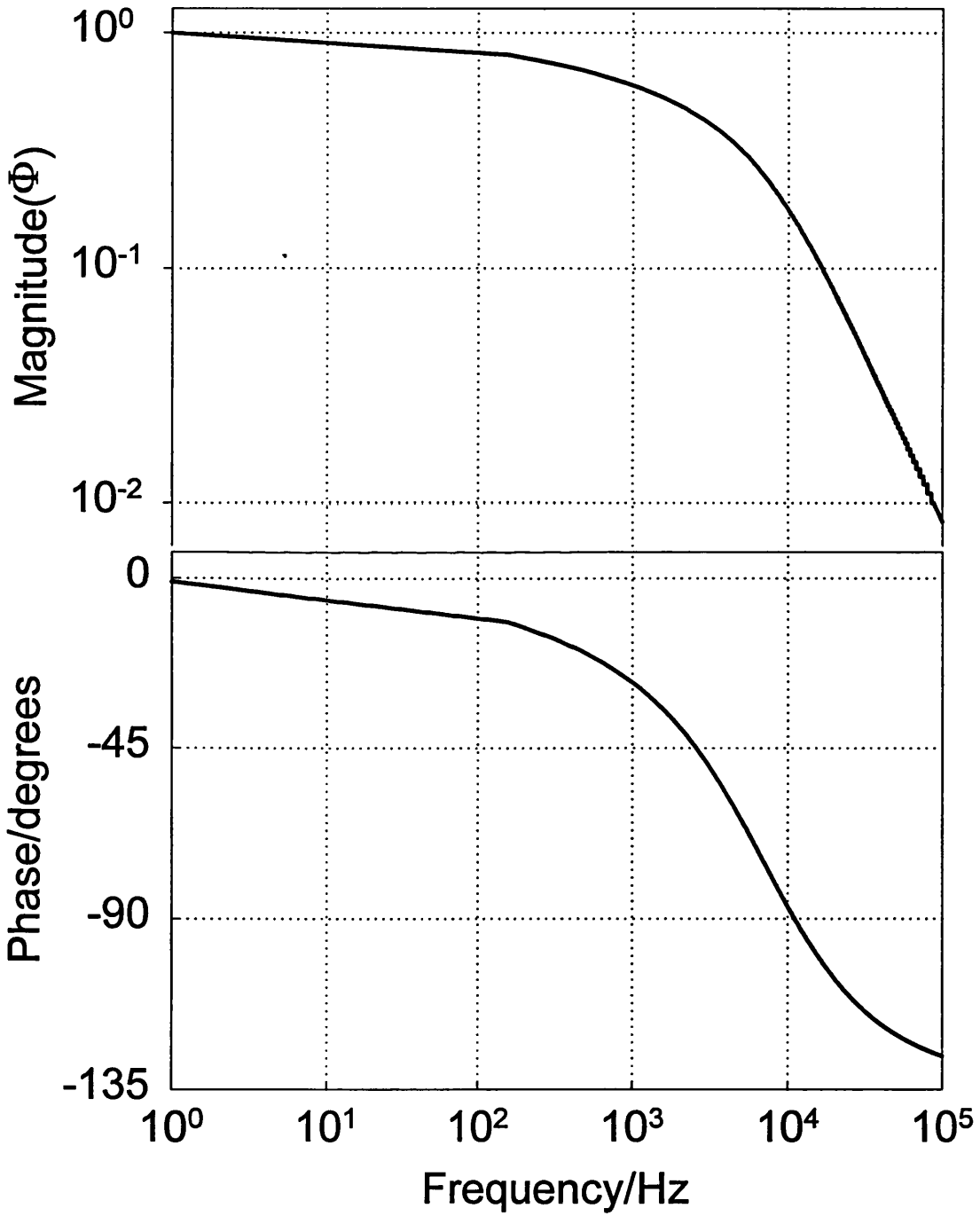

Figure 5.9(a). Bode plots of the IMPS response for illumination from the substrate side for the same parameters as **Figure 5.8.**

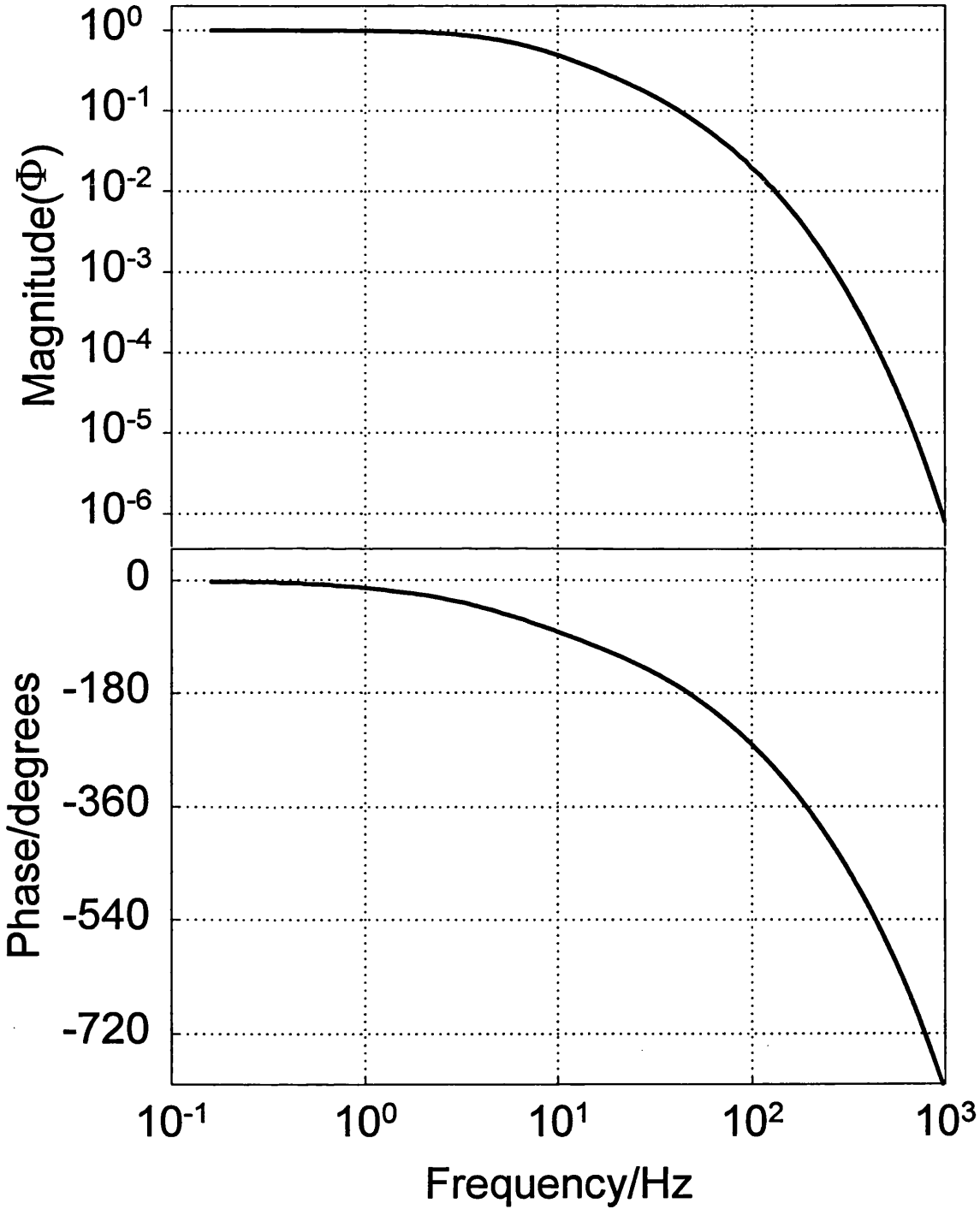

Figure 5.9 (b). Bode plots of the IMPS response for illumination from the electrolyte side for the same parameters as **Figure 5.8**.

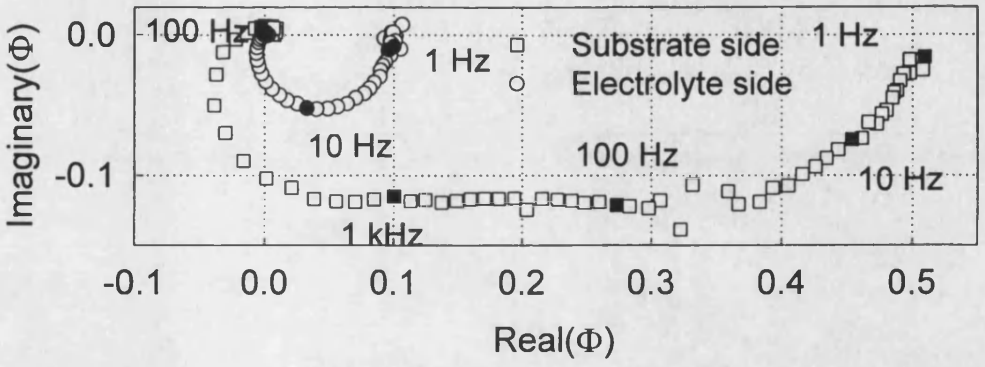

Figure 10. Experimental IMPS plot of the TiO_2 nanoparticulate film for illumination from the electrolyte and substrate side at 0V vs. I^-/I_3^-. Note that the photocurrent conversion efficiency calculated from the low frequency intercept of the IMPS plot is the same as the one of the steady state photocurrent.

Figure 5.10 shows the experimental IMPS plots for illumination from the substrate and electrolyte side. The low frequency intercept corresponds to the steady state photocurrent, within experimental error the values of the dc photocurrent conversion efficiency derived from IMPS and current-voltage measurements are the same. For illumination from the electrolyte side the IMPS plot crosses the imaginary axis, as predicted theoretically, given the long distance electrons have to travel to reach the substrate. ω_{MIN} is equal to 53 Hz which corresponds to a diffusion coefficient of $4\times10^{-6}cm^2s^{-1}$. Good agreement is obtained between the experimental data and equation (3.57) **(Figure 5.11 (a))** for long electron lifetimes, as calculated from photovoltage measurements. The *RC* attenuation factor has also been included, however its effect is not noticeable given the big excursion of the IMPS plot in the 3rd quadrant (real negative + imaginary negative) [8].

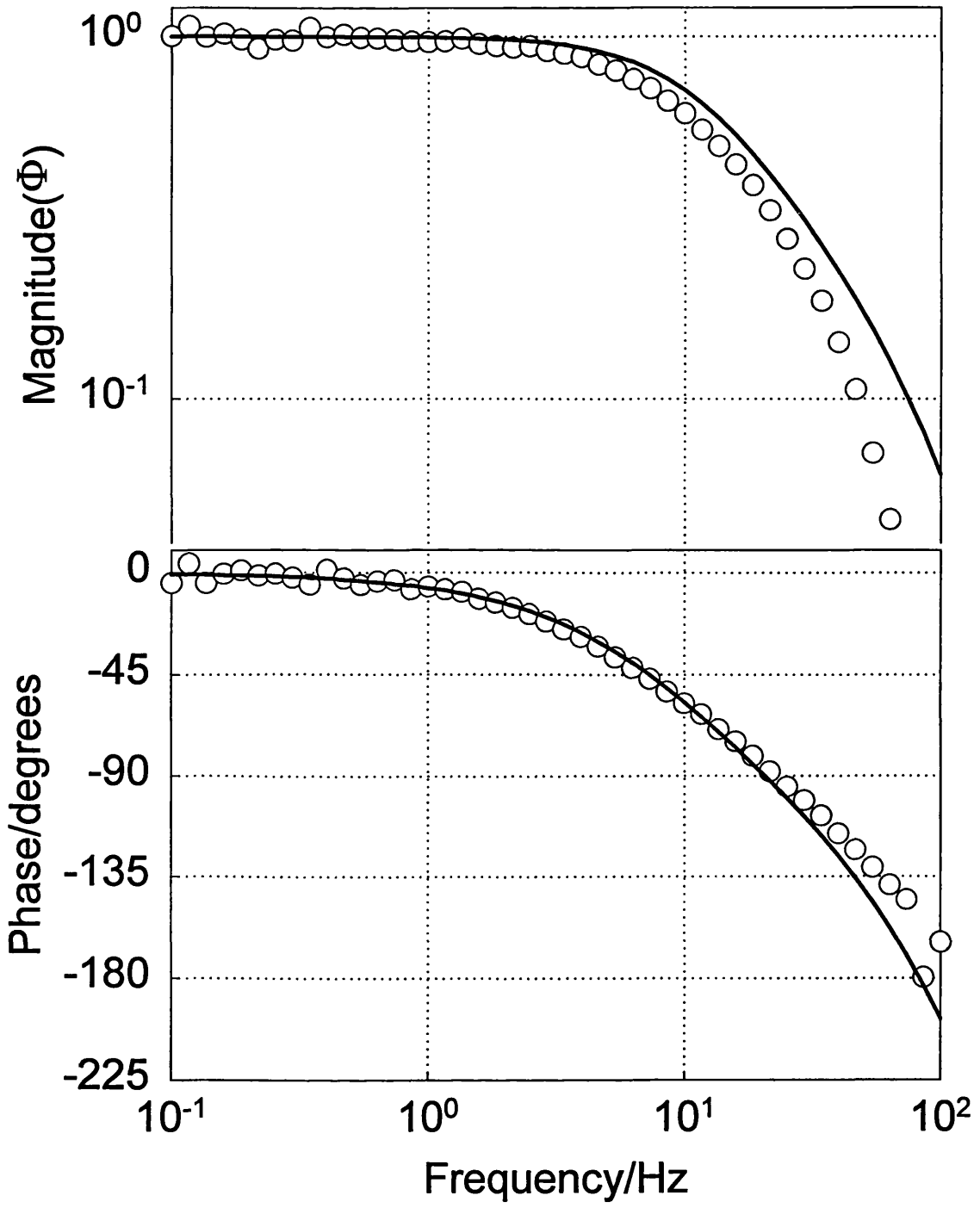

Figure 5.11(a). Normalised Bode plots comparing the IMPS response for illumination from the electrolyte side with simulations obtained from equation (3.57) including the *RC* attenuation factor. The fitting values are: d=2.9μm, α=10^5cm^{-1}, $\tau\rightarrow\infty$, D=2.2×10^{-6}cm^{2}s^{-1}, R=11Ω, η=1 and C=2×10^{-6}F.

For illumination from the substrate side, the difference between the experimental (**Figure 5.10**) and the theoretical (**Figure 5.8** and **5.9(b)**) data is twofold. Firstly the experimental value of ω_{MIN} is not as high as predicted by equation (3.51), secondly the experimental phase angle at high frequency goes beyond the 135^0 limiting value. Both these effects can be attributed to the 'dead layer' that introduces a delay d_1^2/D. The presence of a 'dead layer' effect for TiO_2 nanocrystalline films can be attributed to the non-uniformity of the TiO_2 porosity. This means that near the substrate the film is likely to be very compact, low porosity, and therefore there is very little solid/electrolyte interpenetration. This reduces the hole-electron separation efficiency, thus the net injection efficiency, η, decreases approaching zero near the substrate. η is therefore distance-dependent, the higher the porosity the more efficient the hole-electron separation. To a first approximation the profile of η can be represented by a step function so that η changes from 0 to 1. This means that in a portion of the film the hole-electron pair generation term is zero, therefore the model described in section 5.2 applies and the data can be analysed using equation (5.11). Additionally, the absorption coefficient of the TiO_2 film is proportional to the porosity of the film, in the present approach an average value of the absorption coefficient is considered corresponding to a porosity of 50%. For a more sophisticated model both the absorption coefficient, α, and the net injection efficiency, η, should be considered distance-dependent in equation (5.11), such a treatment is beyond the scope of this work.

The presence of this 'dead layer' explains why ω_{MIN} is not as high as the one predicted by equation (3.51) and why the phase angle loops further than 135^0. **Figure 5.11(b)** shows the fitting of the experimental data for illumination from the substrate side with equation (5.11). In order for the 'dead layer' to be observed it is fundamental that its thickness is less than the light penetration depth. The best fitting value for the 'dead layer' is 0.1μm, as shown in **Figure 5.11(b)**, which is comparable with the light

penetration depth. This value gives an estimate of the portion of the film which is compact, it is quite small compared with the total thickness of the film of 2.9μm. However its effect is quite remarkable especially at high frequencies. The fact that hole and electrons recombine near the substrate is further enhanced by the high density of traps present in nanoparticles. The electrons localise [1,2] whilst reaching the back contact and this increases their probability of recombination with holes, especially near the substrate where I^- is nearly absent.

It has been shown [6,9] that for long lifetimes the diffusion coefficient depends on the light intensity ($D=d^2\omega_{MIN}\propto I^n$, $n<1$), the higher the light intensity the higher the diffusion coefficient. This is due to the fact that for high light intensities the quasi-Fermi level is nearer to the conduction band and therefore the detrapping rate increases. This reduces the localization time of electrons in the surface states increasing the diffusion time. For illumination from the electrolyte side, for short penetration depths, in the region of the film closer to the substrate the light intensity is low. This means that electrons have to travel through a 'dark' region of the film and therefore the average diffusion coefficient is lower compared with illumination from the substrate side. However, from the fitting the values of the diffusion coefficients are nearly the same. This can be explained with the fact that the region near substrate, where the net injection efficiency is zero, can be considered like a 'dark' region. Thus for illumination from the substrate side even if the electrons are generated near the substrate they still have to travel through a 'dark' region, this lowers the average diffusion coefficient making it comparable with the case of illumination from the electrolyte side.

The result that in the dye-free TiO_2 nanoparticles there is a very compact region with low porosity agrees with the fact that for dye-sensitized solar cell the dye penetrates only partially into the film. If the pores are small near the substrate, the dye molecule cannot adsorb onto the TiO_2 nanoparticles. Unfortunately it is not possible to

compare the thicknesses of the dye-free region in dye-sensitized electrodes with the compact region of TiO_2 nanoparticles because the films have been prepared in different laboratories, moreover the size of the dye molecule should be kept into account. This goes beyond the scope of the present work.

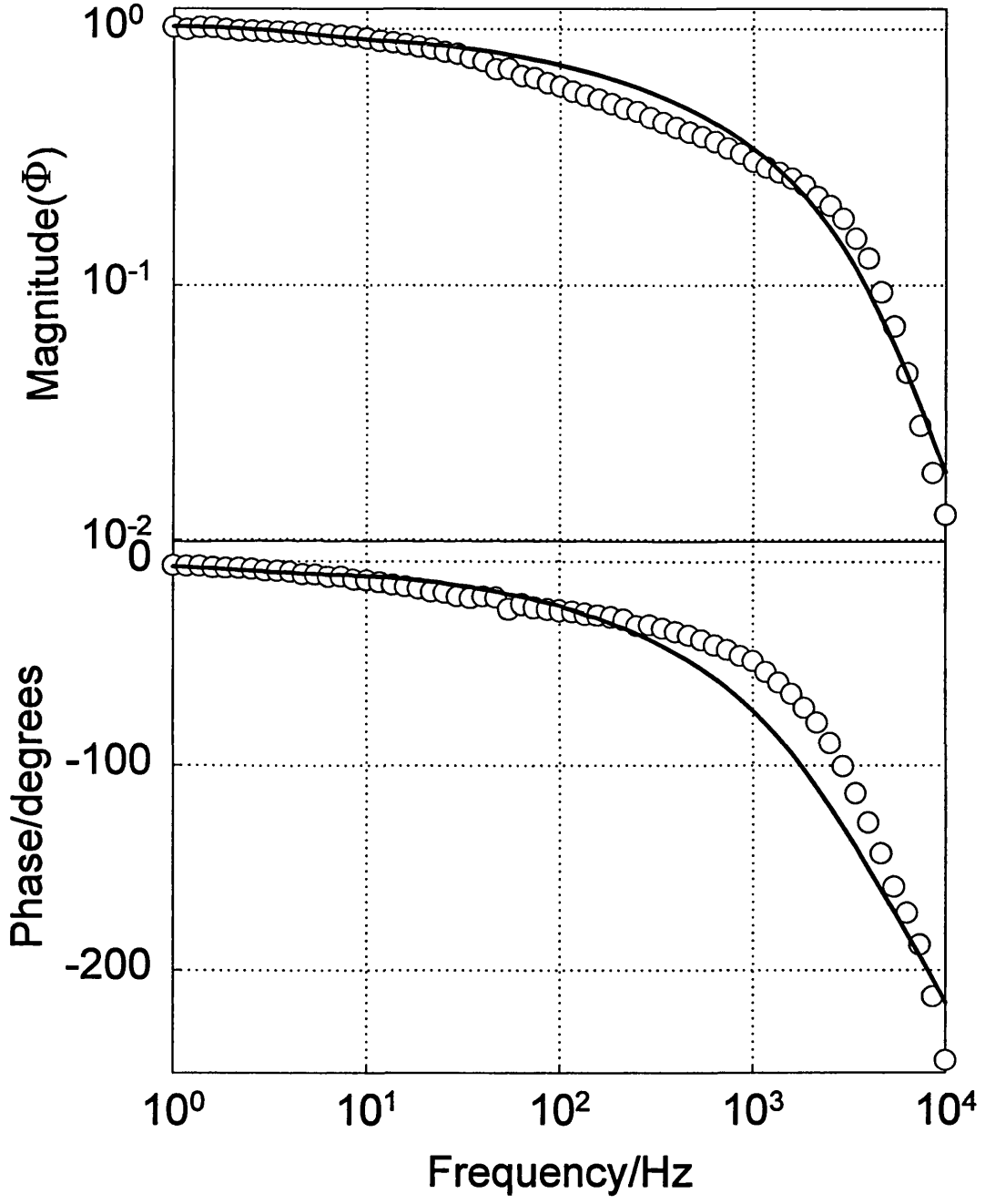

Figure 5.11(b). Normalised Bode plots comparing the IMPS response for illumination from the substrate side with simulations obtained from the 'dead layer' model (equation (5.11)) including the *RC* attenuation factor.The fitting values are:d=2.9μm,d_l=0.1μm,α=10^5cm^{-1},$\tau\rightarrow\infty$,D=2.2×10^{-6}cm^{2}s^{-1}, R=11Ω, η=1 and C=2×10^{-6}F. Note that the low porosity region of the film is of the same thickness as the light penetration depth.

5.5 Conclusion

Complex plane IMPS plots for illumination from the substrate side for dye-sensitised solar cells cross the imaginary axis. This suggests the presence of a dye-free region in the film which adds a delay in the photomodulated current response. Excellent agreement is found between the experimental and the theoretical results after introducing this dye-free region in the collection/generation model.

IMPS measurements were also performed on dye-free TiO_2 nanocrystalline films. Good agreement is found for illumination from the electrolyte side with equation (3.57). On the other hand, for illumination from the substrate side a loop of the phase angle is observed at high frequency which cannot be explained with the simple generation/collection equation, even if the *RC* attenuation time is introduced. This suggests that near the substrate the porosity of the film is very low reducing the efficiency of charge separation. Introducing a 'dead layer' effect, excellent agreement is found between theoretical and experimental data.

5.6 References

[1] P. E. Jongh and D. Vanmaekelbergh, J. Phys. Chem. B, 101, 2716, (1997).

[2] P. E. Jongh and D. Vanmaekelbergh, Phys. Rev. Lett., 77, 3427, (1996).

[3] G. Franco, L. M. Peter and E. A. Ponomarev, Electrochem. Comm., 1, 61, (1999).

[4] B. O'Regan and M. Grätzel, Nature, 353, 737, (1991).

[5] M. K. Nazeeruddin, A. Kay, I. Rodicio, R. Hunphry-Baker, E. Muller, P. Liska, N. Valchopoulos and M. Grätzel, J. Am. Chem. Soc., 115, 6328, (1993).

[6] L. Dloczik, O. Ileperuma, I. Lauermann, L. M. Peter, E. A. Ponomarev, G. Redmond, N. J. Shaw and I. Uhlendorf, J. Phys. Chem. B, 101, 10281, (1997).

[7] D. J. Blackwood, PhD Thesis, 'Anodic oxide films on titanium in acidic media',

School of Chemistry, University of Southampton, U.K., (1986).

[8] G. Franco, L. M. Peter and K. G. Upul Wijayantha, in preparation

[9] F. Cao, G. Oskam, G. J. Meyer and P. C. Searson, J. Phys. Chem., 100, 17021, (1996).

CHAPTER VI

FREQUENCY-RESOLVED OPTICAL DETECTION OF ELECTRONS

6.1 Introduction

This chapter deals with the optical detection of accumulated electrons in dye-sensitised solar cells. The results obtained by optical detection in the near infrared are related to dynamic photocurrent, photovoltage and impedance responses [1]. Accumulation of electrons in nanocrystalline TiO_2 electrodes without dye-sensitisation has been studied previously [2,3] by optical absorption spectroscopy. In these studies, electron accumulation was brought about controlling the potential of the electrode. The present work has established that electron detection can also be achieved in dye-sensitised solar cells provided that a wavelength in the near infrared is chosen beyond the onset of absorption of the dye and I_3^-. Accumulation of photoelectrons in dye-sensitised solar cells was brought about using intensity modulated visible excitation in the absorption band of the dye. The resulting modulation of the near infrared optical transmittance arising from the perturbation of the electron density was measured as function of modulation frequency under open circuit and short circuit conditions. The frequency-resolved normalised modulated transmittance $\Delta T/T$ was compared with the modulated photocurrent, photovoltage and impedance measured with the same illumination intensity. Analysis of these responses confirmed that substantial electron accumulation occurs in nanocrystalline titanium dioxide even under short circuit conditions. The majority of electrons that is detected by modulated transmission appears to be located in the traps.

6.2 Experimental Section

Dye-sensitised TiO_2 cells [4] were prepared following the methods described by Nazeeruddin et al. [5]. The thickness of the cell was limited to 2.7μm in order to obtain a reliable transmission measurement in the near infrared and to minimise the effects due to the *RC* time constant [6]. The total electrode area was 3.5cm^2.

The cell was illuminated with the 514nm line of an argon ion laser. The intensity of the laser beam was modulated using an Isomet acousto-optic modulator driven by a Solartron 1250 frequency response analyser [7]. The maximum incident power was 14mW, and the peak to peak modulation depth was 18%. The laser beam was expanded to illuminate an area of 0.8cm^2. The short circuit current of the cell was measured and used to calculate the photocurrent conversion efficiency (defined as the ratio of electron flux to the incident photon flux, corrected for reflection). The value of the monochromatic conversion efficiency found was of 0.31. This agrees closely with the value calculated from the measured absorbance of the cell at 514 nm by assuming that the quantum efficiency for electron injection ($\eta(V=0)$) is unity, i.e. no back reaction of electrons with the oxidised dye occurs at short circuit. An identical value of 31 % for the photocurrent conversion efficiency was calculated from the low frequency intercept of the modulated photocurrent response.

The transmittance of the cell was measured at 940 nm using a Kodenshi GaAs (OPE5594) light emitting diode (LED) source and Sharp silicon (PD481PI) diode detector with a built-in IR filter that eliminated stray light from the laser beam. The wavelength was chosen to lie beyond the absorption bands of the dye and of I_3^-. For the short circuit photocurrent and modulated transmittance measurements, the voltage of the cell was controlled by a potentiostat operating in two-electrode mode. Open circuit photomodulated transmittance measurements were performed with no external connections to the cell. The measured photomodulated transmittance signal ΔT was

divided by the dc transmittance T to give the dimensionless complex quantity $\Delta T/T$, which was plotted in the complex plane.

Photovoltage measurements were made by connecting the cell to the frequency response analyser via a high-impedance low-noise preamplifier (Stanford model SR560). Impedance measurements were made under white light illumination using a Solartron 1286 interface and a Solartron 1250 frequency response analyser. The illumination intensity was adjusted to give the same short circuit dc photocurrent density as that measured in the photomodulated transmittance measurements. Impedance was measured by perturbing the cell about its open circuit voltage (typically V_{oc}=0.65V).

6.3 Results and Discussion

6.3.1 Calculation of the Optical Absorption Cross Section of Electrons

Figure 6.1 displays the normalised photomodulated near infrared transmittance responses, $\Delta T/T$, measured under open and short circuit conditions respectively. The dc short circuit photocurrent density was 1.8mAcm^{-2} and the low frequency limit of the ac photocurrent density was 0.3mAcm^{-2}. The dc open circuit voltage was 0.63V and the low frequency limit of the modulated photovoltage was 6.6mV, as shown in **Figure 6.2**.

The $\Delta T/T$ plots are semicircular and they can be compared with the theoretical plots shown in section 3.6 for the trap-free case and for the single-trap case. The minima of the experimental plots for the short and open circuit case occur close to 20 Hz. As expected, the low frequency intercept of $\Delta T/T$ is smaller under short circuit conditions because the electrons are extracted at the substrate contact. On the other hand, under open circuit conditions they can relax only by the back reaction with I_3^- or with D^+.

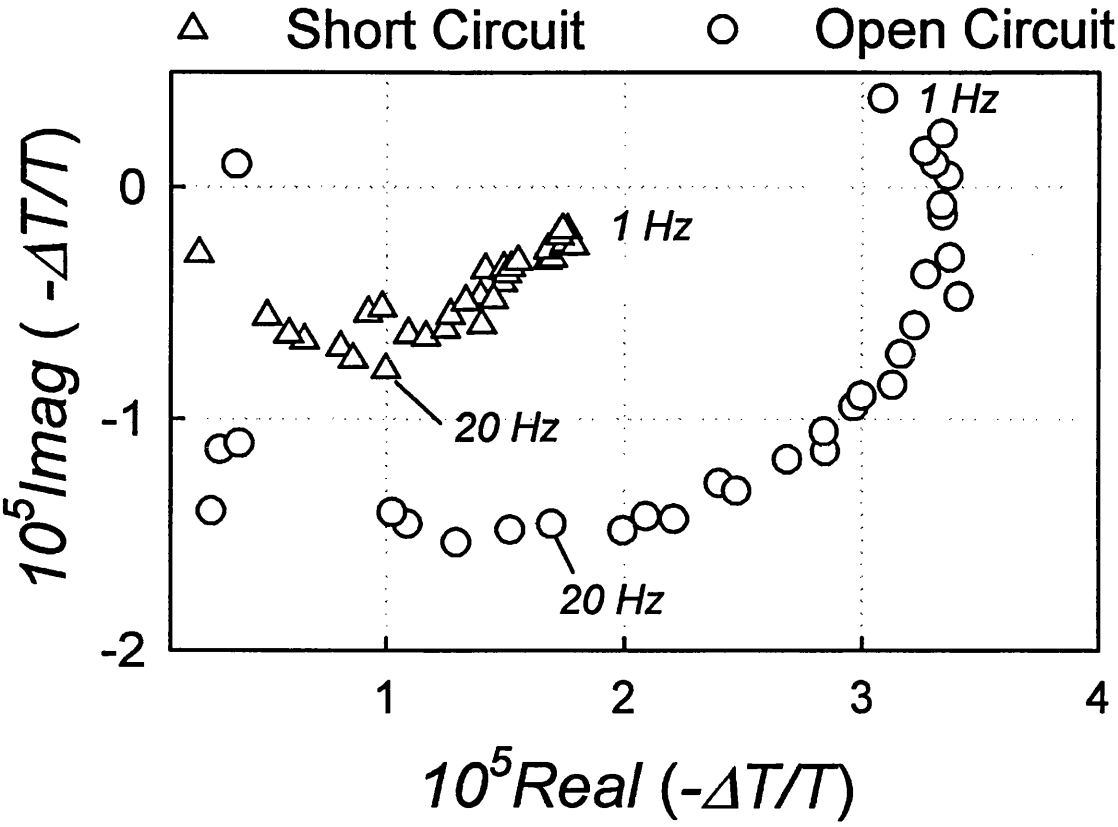

Figure 6.1. Complex plane plots of the photomodulated transmittance ($\Delta T/T$) response of the dye-sensitised solar cell showing accumulation of electrons under conditions of optical injection. The excitation wavelength is 514nm and the detection wavelength is 940nm. Note that the characteristic relaxation frequency ω_{MIN} is the same in both plots.

Figure 6.2 illustrates the intensity modulated photovoltage response measured under the same illumination conditions as those for the photomodulated transmittance. It can be seen that the minima in the photovoltage and transmittance plots occur at the same frequency (20 Hz). The low frequency intercept of the $\Delta T/T$ plots is related to the low frequency intercept of the total modulated charge by:

$$-\left.\frac{\Delta T}{T}\right|_{\omega\to 0} = \frac{\delta Q_{tot}\sigma(\lambda)}{q} = \frac{C_{tot}\sigma(\lambda)\delta U_{photo}}{q} \qquad (6.1)$$

where $\sigma(\lambda)$ is the weighted average absorption cross section for free and trapped electrons, δQ_{tot} is the low frequency intercept of the total modulated charge per unit area, C_{tot} is the total capacitance (C_{cb}+C_t) (as defined in section 3.3) and δU_{photo} is the

low frequency limit of the modulated photovoltage.

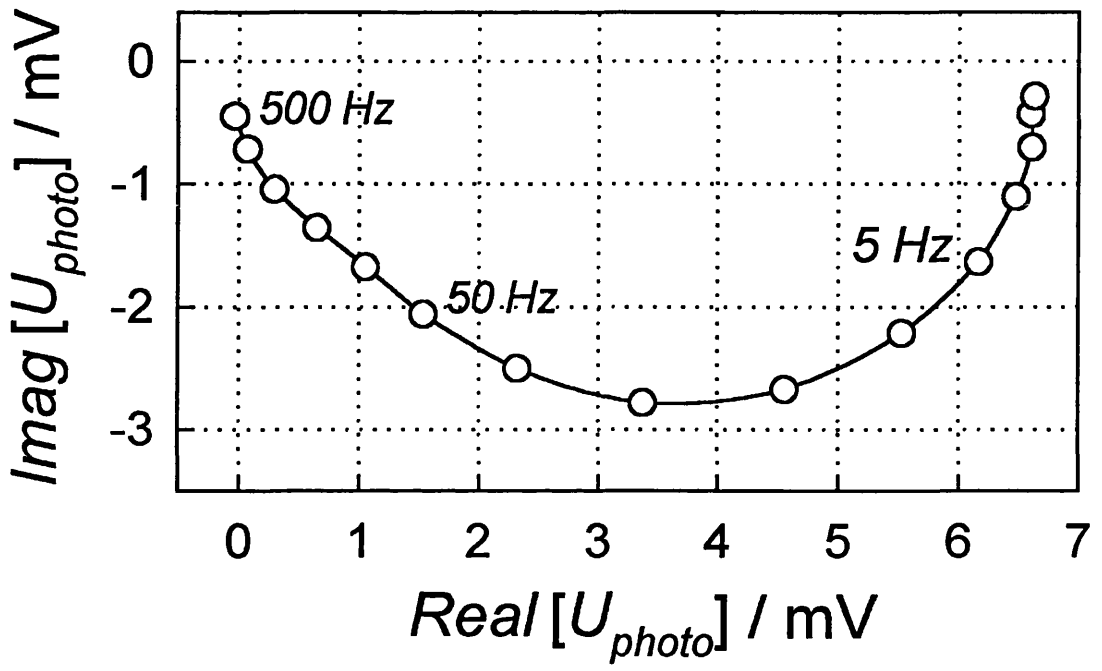

Figure 6.2. Intensity modulated photovoltage response of the dye-sensitised solar cell under the same illumination conditions as those used in **Figure 6.1**. Note that the characteristic frequency ω_{MIN} is the same as that seen in the $\Delta T/T$ responses.

The total capacitance derived from the impedance measurements at open circuit (see **Figure 6.3**) at the same illumination level is 1.12×10^{-4}Fcm^{-2}. The weighted average optical cross section, $\sigma(\lambda)$, can then be evaluated from **Figure 6.1** and **6.2** using equation (6.1). The value found for the weighted average absorption cross section is 7.3×10^{-18}cm^2 at 940nm. This is in good agreement with the optical cross sections calculated for electrons in TiO_2 by Rothenberger et al. [2] (1.3×10^{-18}cm^2 at 780nm). Boschloo and Fitzmaurice [3] have measured the absorbance associated with potential controlled electron accumulation in TiO_2. They showed that for lithium electrolytes the absorption cross section increases with the accumulated charge, providing evidence for lithium intercalation into TiO_2, as discussed in chapter VII. The optical cross sections

calculated by these authors as function of voltage changes from 3×10^{-18} to $1.5\times10^{-17}cm^2$ at 800nm. The absorption cross section found in the present work falls within this range.

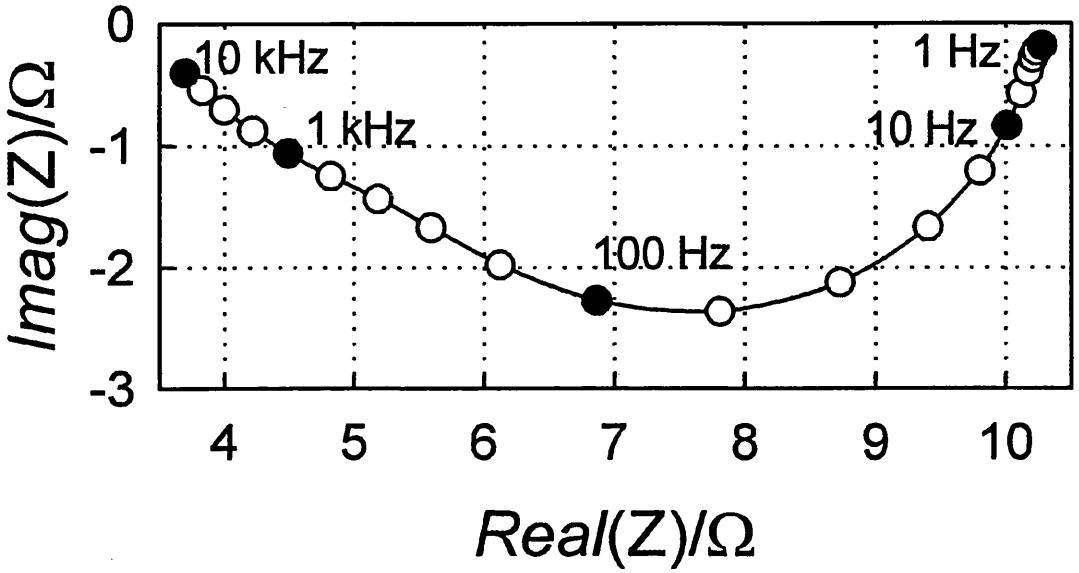

Figure 6.3. Impedance of the dye-sensitised solar cell under illumination at open circuit. The (constant) illumination condition was identical to the level used for the $\Delta T/T$ and the photovoltage measurements (**Figure 6.1** and **6.2**). The fitting parameters for the smaller semicircle (counter electrode impedance) are R=1.7 Ω and C=9.7×10^{-5} F. For the larger semicircle (dye-sensitised electrode impedance) the fit gives R=4.8 Ω and C=3.8×10^{-4} F.

6.3.2 Calculation of the Net Electron Injection Efficiency at Open Circuit

Figure 6.3 illustrates the impedance response of the cell measured under illumination. The results of a detailed impedance study are reported elsewhere [8]. The illumination intensity was adjusted to give the same short circuit dc photocurrent density ($1.8mAcm^{-2}$) as that measured in the photomodulated transmittance and photovoltage measurements. The dc open circuit voltage was measured as 0.63V. The larger of the two semicircles can be attributed to the parallel combination of the recombination resistance with the photocapacitance C_{tot}. The smaller semicircle arises from the Faradaic impedance of the I_3^-/I^- reaction at the transparent counter electrode in

parallel with the counter electrode capacitance. The value found for the capacitance was C_{tot}=1.12×10^{-4}Fcm^{-2}.

The low frequency intercept of the modulated photovoltage (**Figure 6.2**) multiplied by the total photocapacitance gives the total modulated charge. The value found in this way is 7.3×10^{-7}Ccm^{-2}. By contrast, the value found from the product $j_{photo}\tau$ is 2.4×10^{-6}Ccm^{-2}. The net injection efficiency $\eta(U_{photo})$ given by the ratio $C_{tot}\delta U_{photo}(\omega\rightarrow 0)/j_{photo}\tau$ is therefore equal to 0.3. This result suggests that the back reaction of electrons with D^+ contributes significantly to the limitation of the open circuit voltage in dye-sensitised cells. This agrees with the results found by the early work of O'Regan et al. [9] and the more recent work by Haque et al. [10]. The latter authors have shown that the rate of decay of the D^+ state following flash excitation is strongly potential dependent and occurs on a nanosecond timescale at potentials corresponding to V_{oc}.

The work of Haque et al. [10] shows that the reaction of electrons with D^+ under accumulation conditions occurs on a nanosecond time scale. Their data indicate that the half-life for the reaction is reduced to 100ns at a potential that corresponds to open circuit, i.e. 600mV. Haque et al. [10] also studied the rate of D^+/I^- reaction and found a pseudo-first order lifetime of 100ns for 0.3moldm^{-3} KI in propylene carbonate. It follows that the rates of reaction of D^+ with electrons and with I^- at open circuit voltage are very similar, so that $\eta(U_{photo})$ should be less than unity. A rough order of magnitude comparison of the rate reaction of electrons and of iodide ions with D^+ can be made by considering the reactions to be quasi-homogeneous. The concentration of iodide in the cells used in the present study is 0.5mol dm^{-3}. The total open circuit excess of electron density estimated from the product $j_{photo}(dc)\tau\eta(U_{photo})$ is 2.7×10^{13}cm^{-2}, which corresponds to a volume density of 1.7×10^{-4}mol dm^{-3}. Since the diffusion coefficients of electrons and I^- appear to be of the same order of magnitude, the upper diffusion limited

second-order rate constants for the reaction of D^+ with electrons and with iodide ions should be similar. Therefore, in order for electron capture by D^+ to compete with the regeneration reaction, its rate constant must be 10^3 times higher than that of the D^+/I^- reaction. From the data of Haque et al. [10], the second-order rate constant for the D^+/I^- reaction is $3\times10^7 dm^{-3}mol^{-1}s^{-1}$. The second-order rate constant for the reaction of electrons with D^+ is therefore of the order of $3\times10^{10}dm^{-3}mol^{-1}s^{-1}$, suggesting that the process is diffusion controlled.

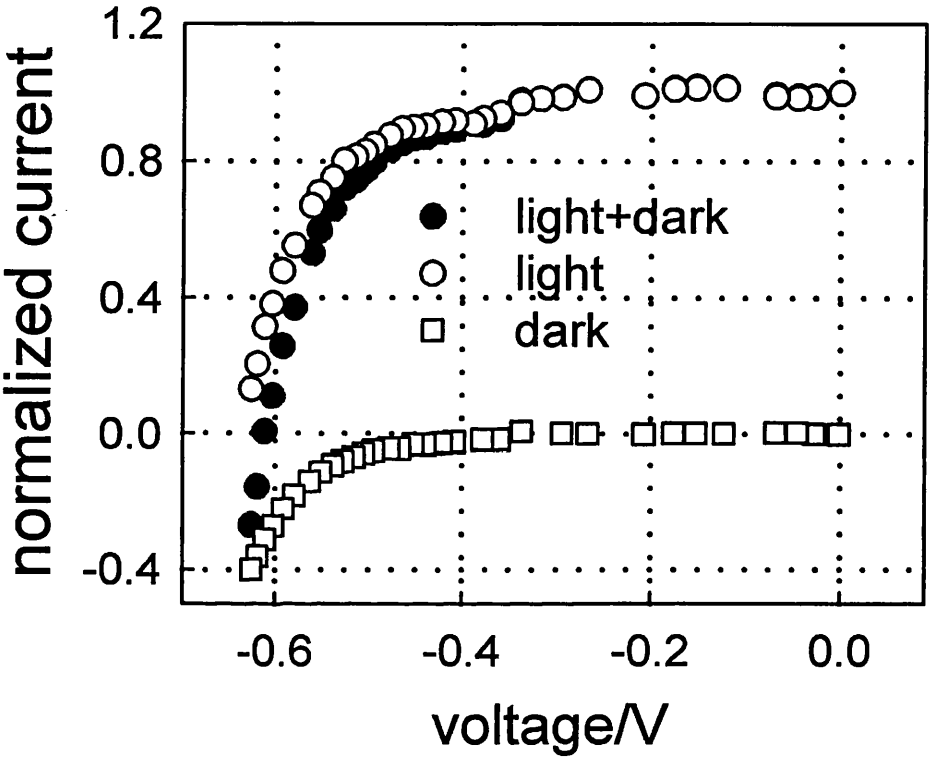

Figure 6.4. Dc current-voltage characteristics of the dye-sensitised TiO_2 cell in the dark and under illumination at the intensity level used for the measurements of $\Delta T/T$, IMVS,PEIS and IMPS. The photocurrent shown was calculated from the difference between the current under illumination and in the dark. Note that V_{oc}=0.61 V and the net efficiency for electron injection, $\eta(V_{oc})$, is equal to 0.3.

In principle, $\eta(V)$, can also be evaluated from the potential dependence of the photocurrent if it is assumed that the dark current and photocurrents are additive. **Figure 6.4** shows the potential dependence of the dc photocurrent measured under the same

illumination conditions as those used for the modulated transmittance experiments. At open circuit $i_{net}=0$, the ratio of the photocurrents at open and short circuit ($i_{photo}(oc)/i_{photo}(sc)$) is equal to $\eta(V_{oc})$. From **Figure 6.4** it can be seen that $\eta(V_{oc})\simeq 0.3$, which is in good agreement with the value calculated from the photovoltage and photocapacitance.

6.3.3 Analysis of the Frequency Dependence of the Photomodulated Transmittance

As shown in section 3.6 the short circuit modulated transmittance response for the trap-free case is a semicircle with ω_{MIN} identical to that measured by IMPS. In the short circuit trap-free case, the excess of electron density relaxes primarily by transport to the substrate. On the other hand the open circuit theoretical $\Delta T/T$ (see section 3.6) gives a semicircle with the same ω_{MIN} as that measured by IMVS because the electron concentration can relax only by the back reaction with I_3^-. **Figure 6.5** shows the short circuit IMPS response of the cell. It appears in the 4th quadrant (positive real + negative imaginary) of the complex plane as the result of the time delay between the generation and the collection of electrons. An order of magnitude estimate of the mean transit time for photogenerated electrons can be obtained from the frequency minimum in the complex plane plot: $\tau_d \simeq 1/\omega_{MIN} \simeq 1$ ms. This approach is an approximation; analytical treatment of the generation/collection problem allows the electron diffusion coefficient to be determined by the fitting of the complete IMPS response [6] (see section 3.5.1).

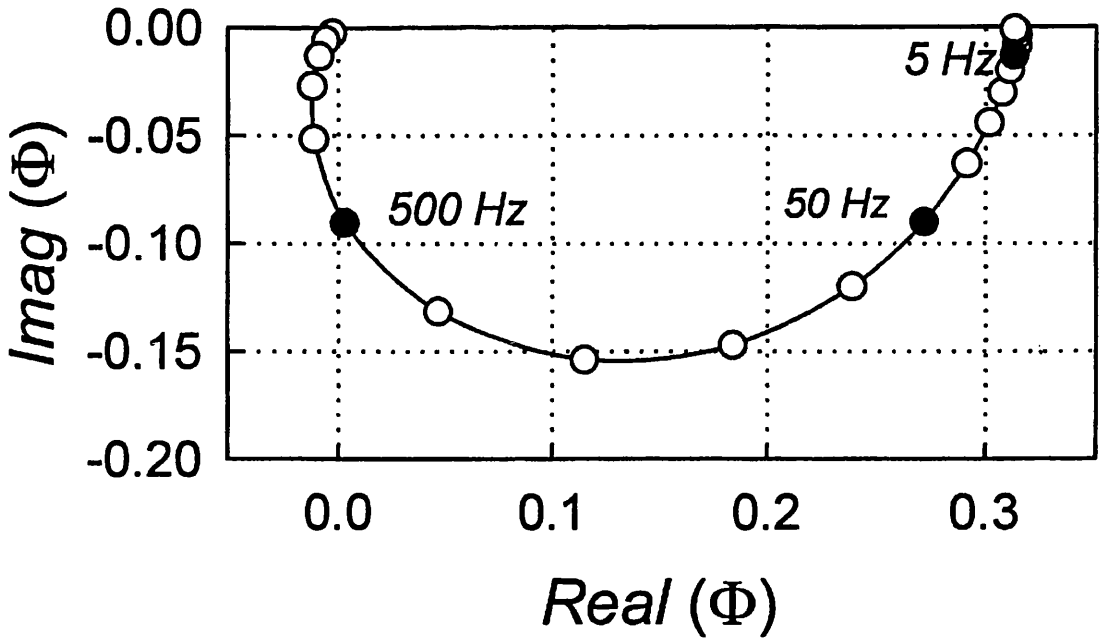

Figure 6.5. Short circuit IMPS response of the dye-sensitised solar cell under the same illumination conditions as those for $\Delta T/T$, IMVS and PEIS (**Figure 6.1** and **6.2**). The low frequency intercept can be used to calculate the incident photon flux to electron flux conversion efficiency (in this case 0.31). Note that the characteristic relaxation frequency ω_{MIN} is much higher in the IMPS response than in the IMVS response because IMPS detects the transit of electrons to the substrate, whereas the other methods detect the (slower) relaxation of the electron density by reaction with I_3^-.

As discussed in section 5.4.1 the IMPS plot shows the surprising feature of crossing the imaginary axis. This is not expected for illumination from the substrate side [11]. Experiments of dye-free nanocrystalline TiO_2 with strongly absorbed UV illumination also show this anomaly [11-13]. For the case of dye-sensitised TiO_2 cells this effect has been attributed to a non-homogeneous dye distribution [11]. **Figure 6.6** compares the Bode plot of the measured IMPS response with a theoretical plot (see equation (5.14)) that takes into account the 'dead layer' effect and the *RC* time constant of the cell [6]. It is important to note that the short circuit IMPS response is insensitive to the electron lifetime since the collection efficiency is close to unity, i.e. $\tau_D << \tau$. The electron diffusion coefficient calculated from the fitting of the IMPS plot shown in **Figure 6.6** is $2.8\times10^{-5}cm^2s^{-1}$.

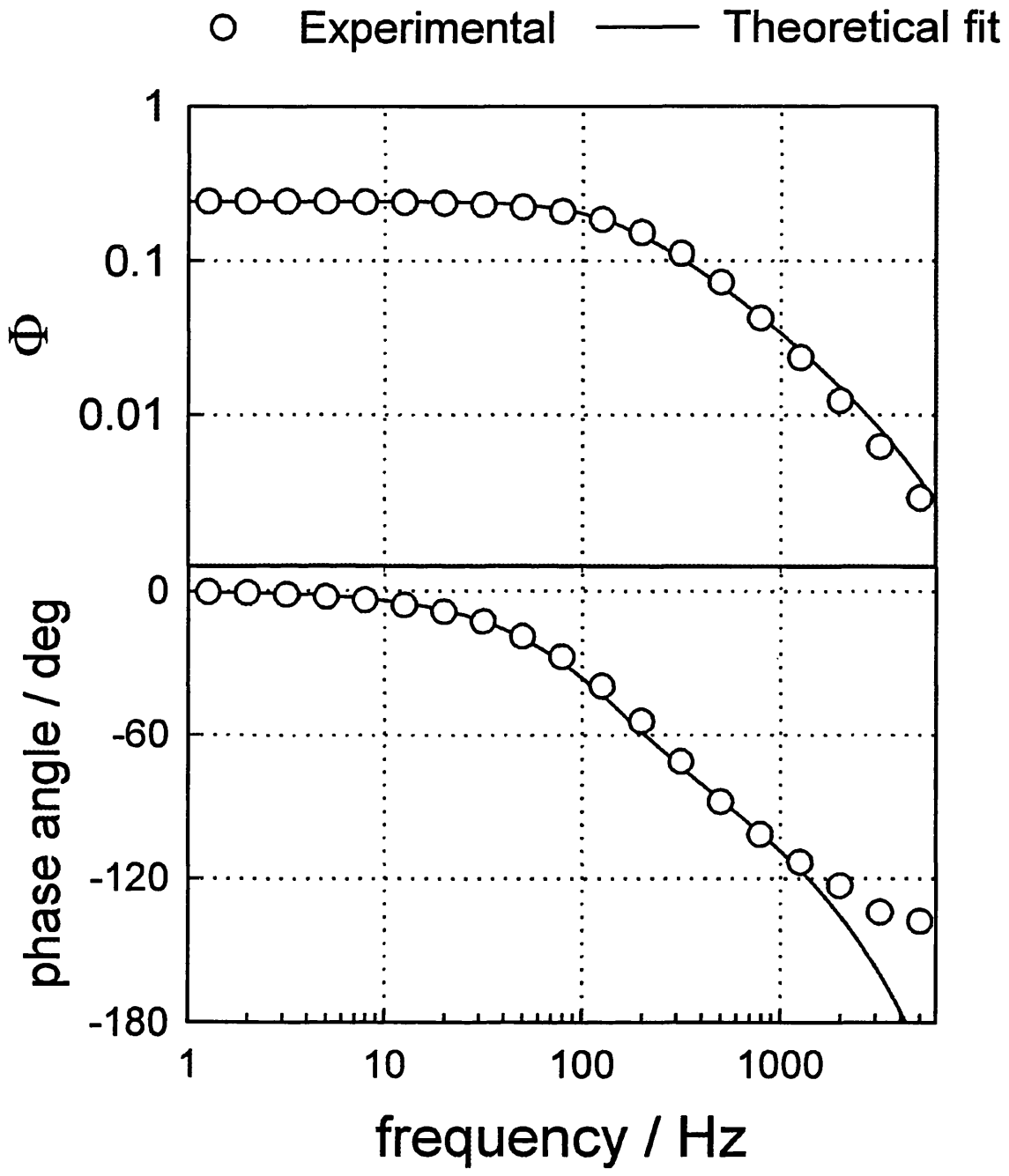

Figure 6.6. Bode plot of the IMPS response of the dye-sensitised TiO_2 cell. The plot also shows the theoretical response calculated taking the non-homogeneous dye distribution and the *RC* time constant of the cell into account. The electron diffusion coefficient obtained by fitting the IMPS response is $2.8\times10^{-5}cm^2s^{-1}$.

It is clear from the experimental complex plot of $\Delta T/T$ measured at open and short circuit (**Figure 6.1**) that the values of ω_{MIN} are essentially identical in the two cases to the value of ω_{MIN} in the IMVS response. This means that the short circuit $\Delta T/T$ response does not detect the relaxation of electron by diffusion to the substrate. It follows that most of the electrons detected optically are trapped at levels sufficiently deep that thermal release to the conduction band is slower than the reaction with I_3^-. The high surface area to volume ratio in nanocrystalline films justifies the fact that energy levels at or near the surface of the TiO_2 crystallites are responsible for trapping and back reaction of electrons. On the other hand, electrons trapped in the bulk of the nanocrystalline have to be released first to the conduction band before they can recombine.

6.3.4 Trapping and Back Reaction in Dye-Sensitised Cells

The effect of electron trapping on the IMPS [6] and IMVS [14] response of dye-sensitised TiO_2 solar cells has been treated in a first approximation using the single-level model. However, a more realistic approach would be to consider a distribution of traps throughout the band gap. In the dark, the Fermi level, E_F (and hence the trap occupancy), in the TiO_2 particles is determined by the electron exchange with the redox system I^-/I_3^-. Under illumination, the trap occupancy is determined by the position of the quasi-Fermi level for electrons $E_{n,F}$ (see section 2.5.2). The competition between thermal release of electrons from the traps and back reaction with I_3^- (effectively recombination) can be used to define the demarcation level $E_{n,d}$ (see section 2.4.3). The demarcation level is the energy at which the probability of an electron to back react with I_3^- and to be thermal released are the same [15]. Electrons below the demarcation level recombine with I_3^- before they can be released into the conduction band. On the other

hand, electrons above the demarcation level are released before they recombine with I_3^- and therefore contribute to the current under short circuit conditions. The relaxation time for electrons above the demarcation level is determined by the effect of trapping, detrapping and transport. Consequently the collection process, and therefore the IMPS response, can be described by an effective diffusion coefficient that determines τ_D. The position of the demarcation level, $E_{n,d}$, relative to the conduction band E_c is defined by:

$$\frac{1}{\tau_{trap}} = k_{release} = \nu e^{-\frac{(E_C - E_{n,d})}{kT}} \tag{6.2}$$

where τ_{trap} is the recombination lifetime of electrons in the traps, $k_{release}$ is the rate constant for thermal release from the traps at the demarcation level and ν is the preexponential factor (see **Figure 6.7**). For example if $\tau_{trap}=10^{-2}$s and $\nu=10^{12}s^{-1}$, equation (62) shows that $(E_c-E_{n,d})\simeq 0.6$eV. The fact that the steady state collection efficiency for photoinjected electrons approaches 100% under short circuit conditions places constraints on the rate at which electrons are trapped and recombine at deep levels. The integrated trapping rate of these centres must be smaller than the inverse of the transit time for electrons generated furthest away from the collector electrode. An order of magnitude estimate of this transit time for a film of thickness d is given by d^2/D. For d=2.7 μm and $D=2.8\times10^{-5}cm^2s^{-1}$, the time required for an electron to reach the substrate from the other side of the film is 2.6ms. The trapping lifetime must be at least 10 times longer, so that an upper limit of the trapping rate is $10s^{-1}$.

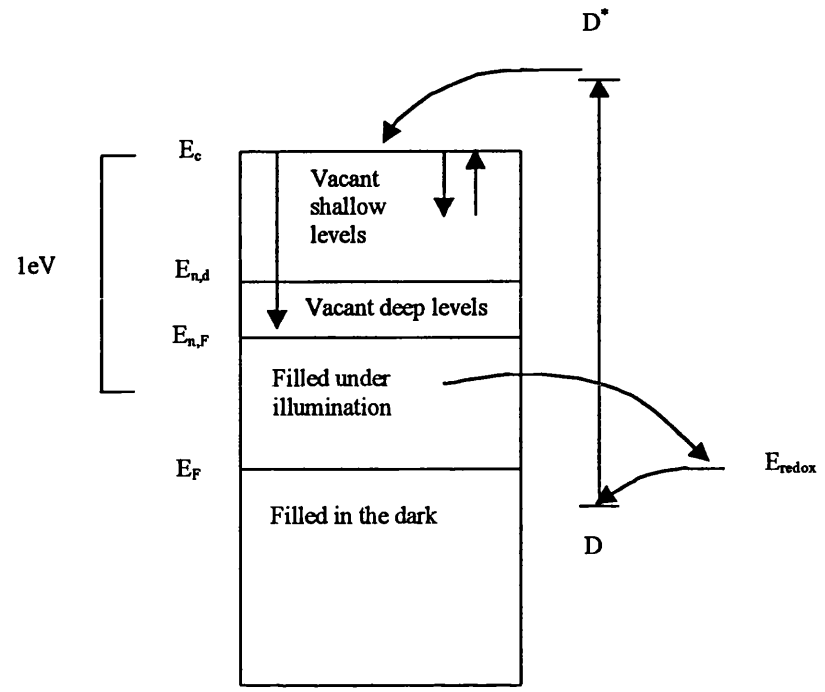

Figure 6.7. Energy level diagram illustrating the equilibrium Fermi level (E_F), the electron quasi-Fermi level under illumination ($E_{n,F}$) and the electron demarcation level ($E_{n,d}$) defined by the competition between thermal release of electrons from traps and recombination with I_3^-.

6.4 Conclusions

The measurement of the periodic component of the electron absorbance was measured in dye-sensitised solar cells using an intensity-modulated laser and an infrared LED. It was found that the majority of the electrons detected are trapped at deep levels where they make no contribution to the measured photocurrent. Instead they react slowly with I_3^-, so that their lifetime is a measure of the rate constant for the back reaction via surface states. At the light intensities of these experiments, the electron quasi-Fermi level lies below the demarcation level over most of the film thickness. The demarcation level, in fact, defines whether the reaction with I_3^- or the thermal release is the dominant relaxation process. The electrons collected under short circuit conditions may be captured briefly by shallow traps and released again before reaction with I_3^- can

occur. The electron transit time will be increased by the sequence of capture and release events, so that the effective diffusion coefficient is considerably lower than the real diffusion coefficient for free electrons. The observed intensity dependence of the diffusion coefficient, D [16], can be explained by the upward movement of the quasi-Fermi level through the distribution of shallow traps.

As dye-sensitised solar cells are very efficient, constraints are placed on the maximum rate at which carriers are trapped by deep traps that act as recombination centres by localising the electrons long enough to permit the back reaction with I_3^- to take place. The open circuit voltage is limited partly by back reaction of electrons with the oxidised state of the dye. Under open circuit conditions the injection efficiency is reduced to about 30 %.

6.5 References

[1] G. Franco, J. Gehring, L. M. Peter, E. A. Ponomarev and I. Uhlendorf, J. Phys. Chem. B, 103, 692, (1999).

[2] G. Rothenberger, D. Fitzmaurice and M. Grätzel, J. Phys. Chem., 96, 5983, (1992).

[3] G. Boschloo and D. Fritzmaurice, J. Phys. Chem. B, submitted for publication.

[4] B. O' Regan and M. Grätzel, Nature, 353, 737, (1991).

[5] M. K. Nazeeruddin, A. Kay, I. Rodicio, R. Hunphry-Baker, E. Müller, P. Liska, N. Valchopoulos and M. Grätzel, J. Am. Chem. Soc., 115, 6328, (1993).

[6] L. Dloczik, O. Ileperuma, I. Lauermann, L. M. Peter, E. A. Ponomarev, G. Redmond, N. J. Shaw and I. Uhlendorf, J. Phys. Chem. B, 101, 10281, (1997).

[7] L. M. Peter, Chem. Rev., 90, 753, (1990).

[8] L. M. Peter and N. J. Shaw, in preparation.

[9] B. O' Regan, J. Moser, M. Anderson and M. Grätzel, J. Phys. Chem., 94, 8720,

(1990).

[10] S. A. Haque, Y. Tachibana, D. R. Klug and J. R. Durrent, J. Phys. Chem. B, 102, 1745, (1998).

[11] G. Franco, L. M. Peter and E. Ponomarev, Electrochem. Comm., 1, 61, (1999).

[12] P. E. de Jongh and D. Vanmaekelbergh, J. Phys. Chem. B, 101, 2716, (1997).

[13] P. E. de Jongh and D. Vanmaekelbergh, Phys. Rev. Lett., 77, 3427, (1996).

[14] G. Schlichthörl, S. Y. Huang, J. Sprauge and A. Frank, J. Phys. Chem. B, 101, 8141, (1997).

[15] R. H. Bube, 'Photoelectric Properties of Semiconductors'; Cambridge University Press: Cambridge, England, 1992; p. 42.

[16] G. Schlichthörl, N. G. Park and A. J. Frank, J. Phys. Cehm. B, 103, 782, (1999).

CHAPTER VII

POTENTIAL-MODULATED TRANSMITTANCE

7.1 Introduction

As shown in section 2.5.1 the calculated thickness of the depletion layer in a nanoparticle is larger than the diameter of the nanoparticle itself, therefore no band bending occurs. However, it can be demonstrated [1,2,3] that the accumulation layer is considerably thinner than the depletion layer when the same amount of charge is transferred across the same interface. Therefore in a nanoparticulate system band bending can occur under accumulation conditions. Under weak accumulation conditions, adsorption/desorption processes control the voltage across the semiconductor/electrolyte surface pinning the band edges, so that any applied potential appears in the space charge region. On the other hand, under strong accumulation conditions the band edges unpin [4,5] so that any further increase in the applied potential occurs across the Helmholtz layer.

The present chapter is concerned with measurement of the potential-modulated infrared transmittance of TiO_2 nanoparticles in the dark under accumulation. The optical cross section of electrons is derived and compared with that obtained in section 6.3.1. This is a novel experiment and it presented some complications. Firstly, under strong accumulation conditions band edge unpinning occurs [6] and therefore the ac potential appears across the Helmholtz layer. Secondly, under strong accumulation conditions lithium intercalation takes place [7], affecting the transmittance response [8]. This narrows the potential window in which the TiO_2 film can be studied under

accumulation, making it difficult to achieve a complete picture of the mechanisms occurring in the present system.

7.2 Theory

In the general case where electrons may be located either in the conduction band or in traps, the near infrared optical transmittance, T, associated with electrons in a TiO_2 film of thickness d is given by:

$$T = \frac{I_t}{I_0} = \exp\left(-\int_0^d \left(\sigma_f(\lambda) n_f(x,t) + \sigma_t(\lambda) n_t(x,t)\right) dx\right) \tag{7.1}$$

here $n_f(x,t)$ and $n_t(x,t)$ are the position and time dependent densities of free and trapped electrons respectively, and $\sigma_f(\lambda)$ and $\sigma_t(\lambda)$ are the corresponding optical absorption cross sections at the wavelength λ. If the electrons are perturbed from their initial stationary values by a modulated potential superimposed on a larger dc level, it can be shown that the ratio $\Delta T/T$ is given by:

$$\frac{\Delta T}{T} = -\int_0^d \left(\sigma_f(\lambda) n_f(x,t) + \sigma_t(\lambda) n_t(x,t)\right) dx \tag{7.2}$$

where $\delta n_f(x)$ and $\delta n_t(x)$ are the induced perturbations of the free and trapped electron densities respectively and ΔT is the resulting change in transmittance.

To relate optical and impedance measurements, the meaning of the capacitances corresponding to the storage of charge in the conduction band and in the traps needs to be clarified. At open circuit in the dark the Fermi level, E_F, in the SnO_2, TiO_2 and the reference electrode are all equal. The equilibrium density of electrons, n_o, in the conduction band of TiO_2 is given by:

$$\frac{n_0}{N_C} = e^{-\frac{(E_C - E_F)}{kT}} \tag{7.3}$$

where N_C is the total number of states in the conduction band and E_C is the conduction

band energy of the semiconductor. On application of a negative bias, the Fermi level of the TiO_2 moves closer to the conduction band energy, increasing the density of free electron. Therefore in the dark the density of electrons in the conduction band under negative bias is given by:

$$n_0 + \Delta n = \int_{E_C}^{qV} N(E) f(E) dE \tag{7.4}$$

where $N(E)$ is the density of states, $f(E)$ is the Fermi-Dirac probability distribution function, E_C is the conduction band of the TiO_2 and V is the applied bias.

The charge across the thickness d of the film is given by:

$$Q_{cb} = q(n_0 + \Delta n)d \tag{7.5}$$

The differential conduction band capacitance can be defined as follows:

$$C_{cb} = \frac{dQ_{cb}}{dV} = q^2 df(E) N(E) \tag{7.6}$$

Analogously the capacitance of trapped electrons can be derived. In the dark the trapped electron density is given by:

$$n_t = \int_{E_V}^{qV} N(E) f(E) dE \approx \int_{E_V}^{qV} N(E) dE \tag{7.7}$$

where E_V, is the energy of the valence band of TiO_2, $N(E)$ is the density of states function for traps in the band-gap, $f(E)$ is the Fermi-Dirac function and V is the applied voltage.

The differential charge in the traps across the film is given by:

$$dQ_t = dq^2 N(E) dV \tag{7.8}$$

It follows that the differential trap capacitance can then be defined and it is given by:

$$C_t = dq^2 N(E) \tag{7.9}$$

The effect of detrapping can be represented by a resistance, R_{detrap}, in series with C_t, so that the time response, $\tau = R_{detrap} C_t$, of the serial circuit introduces the delay due to

detrappping, i.e. $\tau = R_{detrap}C_t = k^{-1}_{detrap}$. However in the present approach it is assumed that the frequency range considered does not show the effect of detrapping, i.e. $\omega << k_{detrap}$. R_{detrap} can then be neglected and the semiconductor/liquid interface can be represented by the parallel of two capacitances:

$$C_{tot}=C_t+C_{cb} \tag{7.10}$$

Although the electrolyte is a saturated solution of LiI in acetonitrile, due to photoxidation effects there are some traces of I_3^-. Therefore if the electrode is under accumulation, the electrons at the surface can, as well as be stored in the capacitances, reduce I_3^- into I^-. It follows that the semiconductor/liquid interface does not behave like a pure capacitance but in parallel with C_{tot} there is a Faradaic resistance responsible for the reduction of I_3^-. The system can, then, be represented by the parallel connection of a resistance and two capacitances with a serial resistance that represents the tin oxide coated glass sheet, as shown in **Figure 7.1**.

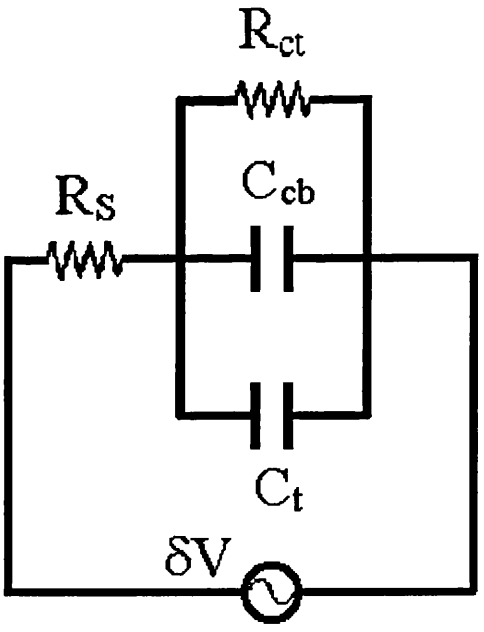

Figure 7.1. Equivalent circuit of the nanoparticulate TiO_2 film. Here C_t is the capacitance associated with trapped electrons, C_{cb} is the capacitance due to free electrons, R_{ct} is the charge transfer resistance, R_S is the sheet resistance and δV is the ac voltage source.

The charge stored by each capacitance is given by:

$$\delta Q_{cb}(\omega) = \frac{\delta V C_{cb}}{1 + \frac{R_s}{R_{ct}} + i\omega(C_t + C_{cb})R_S} \tag{7.11}$$

$$\delta Q_t(\omega) = \frac{\delta V C_t}{1 + \frac{R_s}{R_{ct}} + i\omega(C_{cb} + C_t)R_s} \tag{7.12}$$

where δV is the ac voltage perturbation, C_{cb} and C_t are the two capacitances of the TiO_2 nanoparticulate film, R_S is the serial resistance of the tin oxide coated glass sheet and R_{ct} is the charge transfer resistance. The frequency for which the imaginary component of the total charge is a minimum is given by $(1+R_S/R_{ct})/(2\pi R_S(C_{cb}+C_t))$. However $R_{ct}>>R_S$, therefore a good approximation of f_{min} is: $(2\pi R_S(C_{cb}+C_t))^{-1}$.

Equation (7.2) can then be written:

$$\frac{\Delta T}{T} = -\frac{\sigma_f(\lambda)\delta Q_{cb} + \sigma_t(\lambda)\delta Q_t}{q} \tag{7.13}$$

Hence a weighed optical cross, σ, section can be defined:

$$\frac{\Delta T}{T} = -\frac{\sigma(\lambda)}{q}\delta Q_{tot} \tag{7.14}$$

or equivalently:

$$\frac{\Delta T}{T} = -\frac{\sigma(\lambda)}{q} C_{tot}\delta V \tag{7.15}$$

Equation (7.15) provides a relationship between impedance and optical measurements, and the optical cross section can be evaluated.

7.3 Experimental Section

A three-electrode TiO_2 sandwich cell with a saturated solution of LiI in acetonitrile was prepared as described in section 4.2.2. Traces of I_3^- were present in

solution; therefore the redox couple I^-/I_3^- was used as an internal reference electrode. Measurements of the potential-modulated infrared transmittance in the dark were performed on TiO_2 nanoparticulate film as function of the applied bias vs. I^-/I_3^-. The reference potential of I^-/I_3^- was measured against Ag/AgCl in a saturated solution of LiI with traces of I_3^- (in the order of mmols) in acetonitrile. It was found that Ag/AgCl was 70mV more positive than I^-/I_3^-. Therefore the results obtained in the present experiment performed with a Pt quasi-reference electrode can be compared with the ones performed with Ag/AgCl as shown in the following section.

The cell was connected to a potentiostat operating in three-electrode mode and a modulated voltage was applied using a Solartron 1250 frequency response analyzer, see **Figure 4.7**. The ac voltage applied was 25mV and different values of the bias voltage were applied. The transmittance of the cell was measured at 940nm using a Kodenshi GaAs (OPE5594) light emitting diode (LED) source and Sharp silicon (PD481PI) diode detector with a built-in IR filter. The signal was amplified using a high-impedance low-noise preamplifier (Stanford model SR560). The measured modulated transmittance signal ΔT was divided by the dc transmittance to give the dimensionless complex quantity $\Delta T/T$, which is plotted in the complex plane.

Dc transmittance experiments at 940 nm were also carried out as function of the potential. The set up used was a three-electrode cell connected to a potentiostat and the dc transmission was measured as function of the bias applied. The result was then plotted on an X-Y recorder.

Impedance measurements were performed using a Solartron 1286 interface and a Solartron 1250 frequency response analyzer.

Absorption measurements were performed using a Perkin-Elmer Lamda 40 UV-vis spectrometer.

7.4 Results and Discussion

Figure 7.2 displayes the absorbance of the TiO_2 nanoparticulate film in a 1M $LiClO_4$ acetonitrile solution as function of the applied voltage vs Ag/AgCl as measured by Boschloo and Fitzmaurice [8]. Two processes have been considered to account for the potential dependent optical spectroscopy of nanostructured TiO_2. Firstly the absorption due to the accumulation of both free and trapped electrons and secondly the absorption due to the lithium intercalation [8]. Ion intercalation or ion insertion [7] is an electrochemical process in which anions are incorporated into the bulk lattice of a solid electrode. The double injection of electrons and Li^+ ions into TiO_2 leads to the formation of Ti^{3+} states [9,10] according to: $xLi^+ + TiO_2 + xe^- \rightleftharpoons Li_xTiO_2$, where x is the mole fraction of lithium in titanium dioxide. Controversial values of x have been reported in the literature: 0.5 [11], 0.6 [12], 0.8 [13], and 1 [14,15]. Reasonable insertion-extraction reversibility was reported only for $x \leq 0.5$ [12]. The value of the diffusion coefficients of Li in anatase and rutile has recently been reported by Lindström et al. [16,17] to be $1\times10^{-17}cm^2/s$ for Li insertion and $4\times10^{-17}cm^2s^{-1}$ for Li extraction.

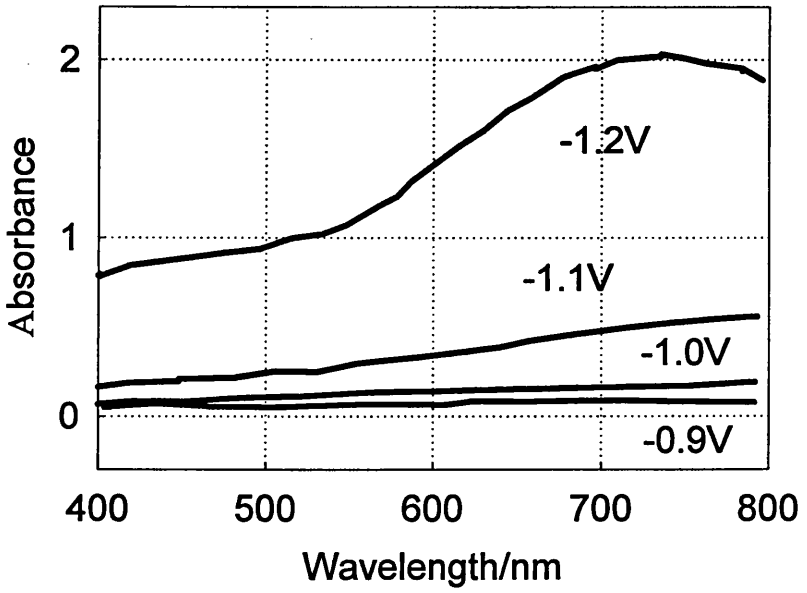

Figure 7.2. Potential-dependent absorbance spectra of a nanoporous TiO_2 film in 1.0M $LiClO_4$ in acetonitrile.

Södergen et al. [9] have shown that at 0V vs. Ag/AgCl only Ti^{4+} states are present in the TiO_2 electrode, whereas applying voltages more negative than –1.0 V vs. Ag/AgCl lithium intercalation occurs and at the same time Ti^{3+} states form. The lithium can be deintercalated, i.e. Ti^{3+} states disappear, at voltages more positive than –1.0V vs. Ag/AgCl. The intercalation and deintercalation of Li^+ in nanocrystalline TiO_2, and therefore the reduction of Ti^{4+} and the oxidation of Ti^{3+} states can be observed in **Figure 7.3**. This figure shows the dc normalized transmission at 940nm of TiO_2 as function of voltage vs. I^-/I_3^-, and the hysteresis is attributed to the lithium deintercalation. The dc transmission at 940nm detects both the accumulated electrons and the intercalated Li, but it is not possible to distinguish the two phenomena clearly. According to Boschloo et al. [8] and Södergen et al. [9] Li intercalation becomes dominant at voltages more negative than –1.0V vs. Ag/AgCl.

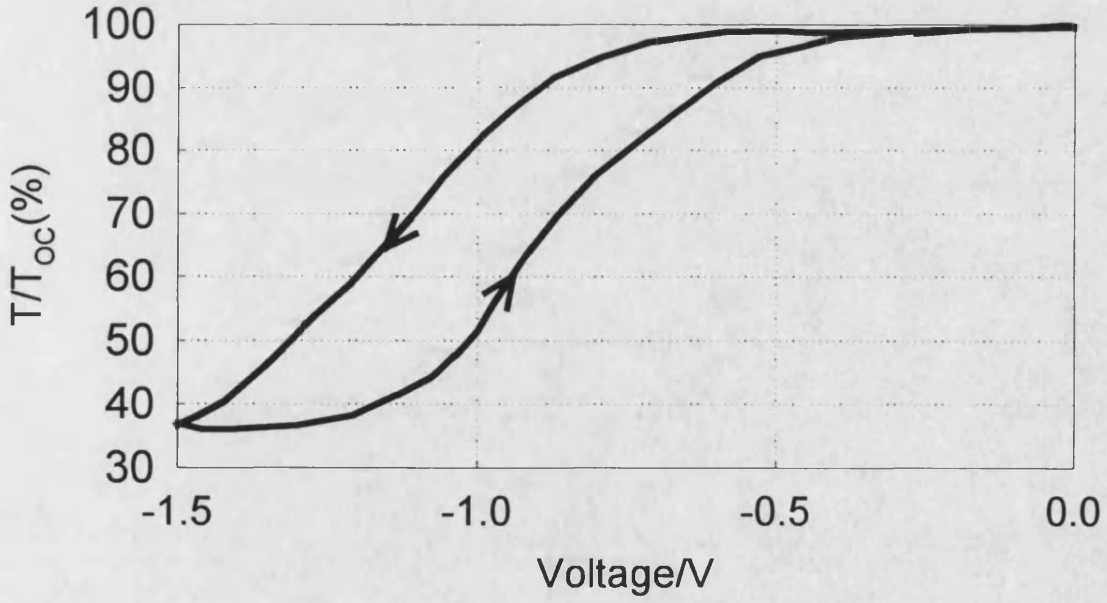

Figure 7.3. Potential dependent dc transmission at 940nm of a nanoparticulate TiO_2 film in a LiI saturated MeCN solution at a scan rate of 10mV/s.

Under strong accumulation conditions, lithium intercalation is not the only limiting factor; band unpinning must be taken into account as well. This means that changes in the applied voltage no longer appear in the space charge region but instead appear across the Helmholtz layer, i.e. the semiconductor starts behaving like a metal. Complications due to both lithium intercalation and band unpinning restricted the potential window in which the potential-modulated transmittance of nanocrystalline TiO_2 could be performed. **Figures 7.4(a),7.4(b),7.4(c)** and **7.4(d)** show the potential-modulated transmittance at 940nm measured at –0.55V, -0.6V, -0.65V and –0.7V vs. I^-/I_3^-. It can be noted that the ac transmittance is independent of the bias in the range considered; in fact both ω_{MIN} and the low frequency intercept are nearly the same for all voltages. As shown above $\omega_{MIN}=(R_S(C_{cb}+C_t))^{-1}$, the experimental results then suggest that the total capacitance is constant. The total capacitance can be evaluated separately through impedance measurements. However, due to the complicated electrochemistry, such as lithium intercalation, which occurs at the TiO_2/liquid interface these measurements were not very reliable. At -0.55V, although the impedance measurements were not too satisfactory, the value of the sheet resistance found was 11Ω and of the total capacitance 3.5×10^{-4}F. These values of R_S and C_{tot} are in good agreement with f_{MIN} in the ac transmittance experiment, as $2\pi R_S C_{tot}$ is equal to 40Hz.

Using equation (7.15) the weighed optical cross section can be evaluated and the value found is equal to $5\times10^{-19}cm^{-2}$, which is smaller than the value found previously (section 6.3.1) of $7.3\times10^{-18}cm^{-2}$. This discrepancy can be attributed to the fact that in the experiment described in chapter VI the Fermi level was lower than in the present one, so that the contribution of free electrons was smaller. It follows that in the present experiment, free electrons contribute strongly to the transmittance result and the weighed optical cross section is much closer to σ_f than to σ_t. For even more negative potentials, the distance between E_c and E_F decreases and hence C_{cb} should increase

exponentially according to equations (7.3) and (7.6). This should in principle be observed in the transmittance response, as it is proportional to C_{tot} (equation (7.15)), but in the potential range explored we are still far from this behavior. On the other hand, if the experiment had been carried out at even more negative potentials the problem of lithium intercalation and band unpinning would have been encountered.

To prove that the change in transmission is due to the electrons in the TiO_2 nanoparticulate film and not to the tri-iodide in solution, the absorbance spectrum of 0.5M LiI and 0.5mM iodine in acetonitrile is shown in **Figure 7.5.** It can be noted that the tri-iodide does not absorb at long wavelengths, therefore the infrared transmission observed can be attributed to electrons in the TiO_2 nanoparticulate film.

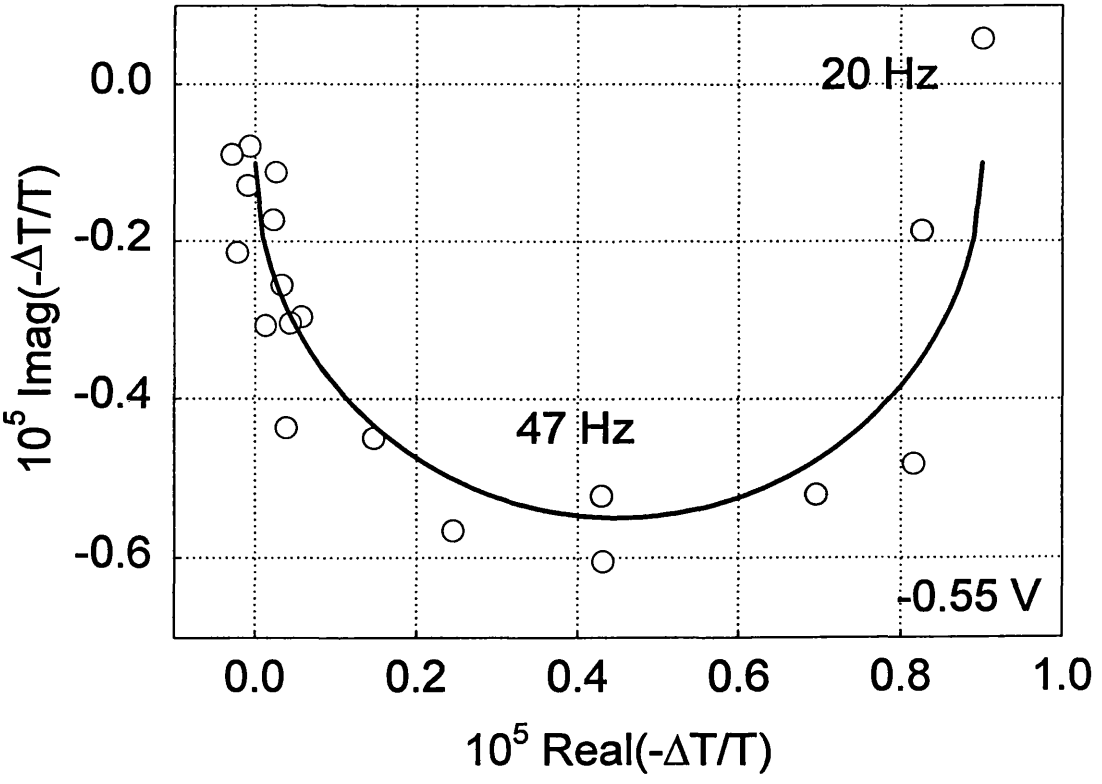

Figure 7.4(a). Potential dependence of the ac transmission at -0.55V of the nanoparticulate TiO_2 film at 940nm. The solid line represents the fitting with a semicircle.

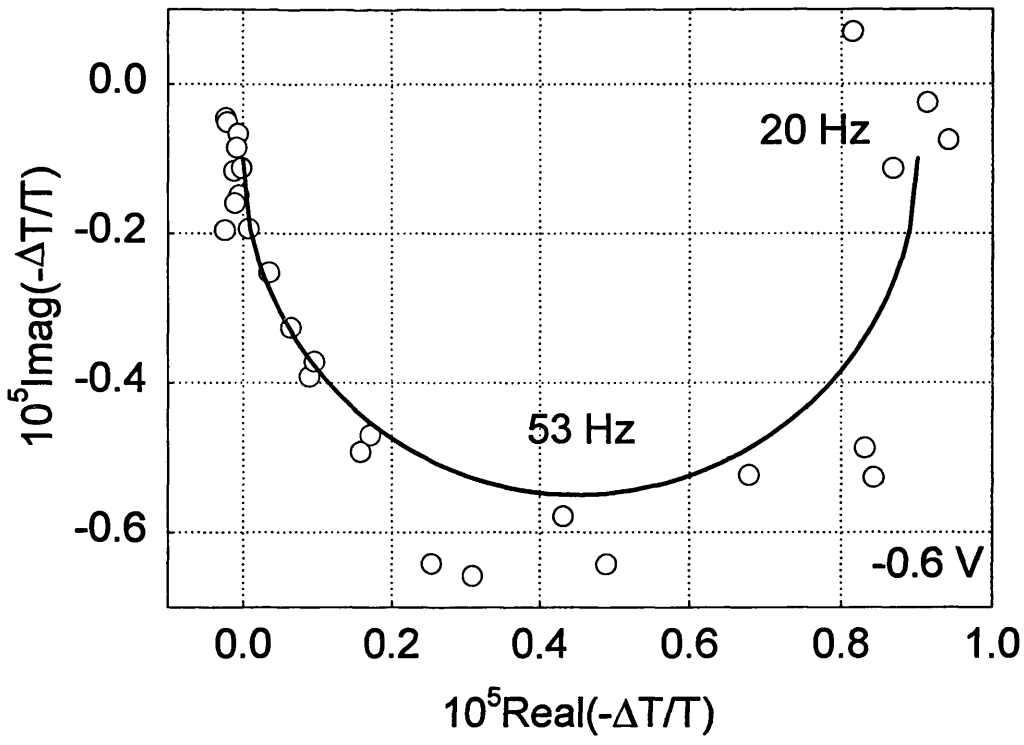

Figure 7.4(b). Potential dependence of the ac transmission at -0.6V of the nanoparticulate TiO_2 film at 940nm. The solid line represents the fitting with a semicircle.

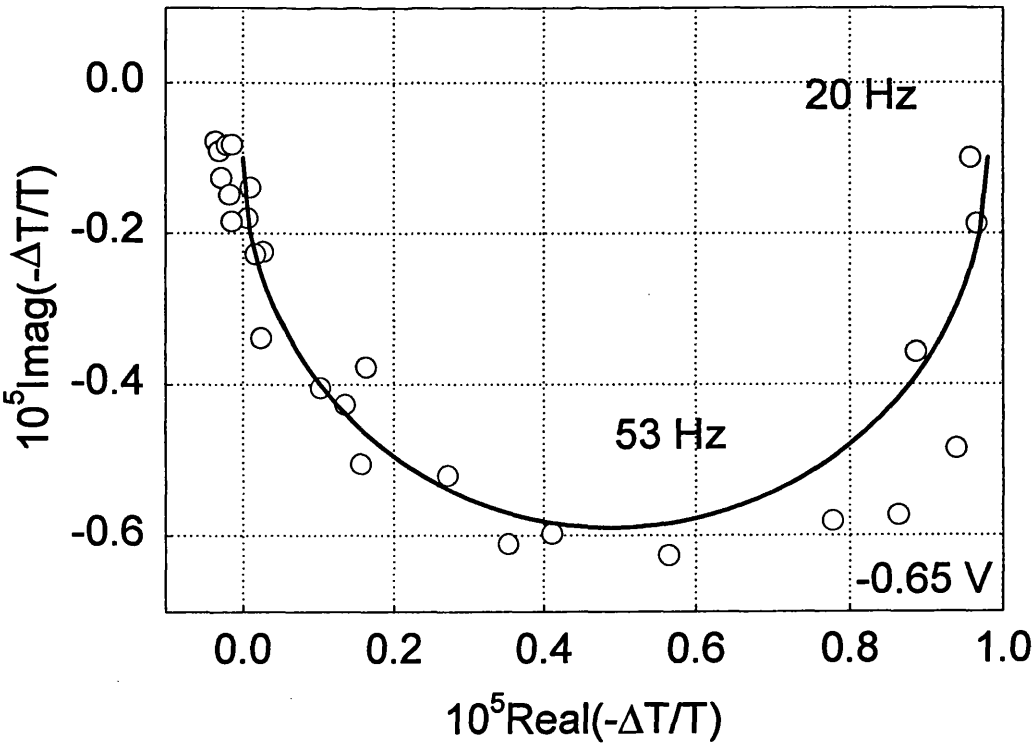

Figure 7.4(c). Potential dependence of the ac transmission at -0.65V of the nanoparticulate TiO_2 film at 940nm. The solid line represents the fitting with a semicircle.

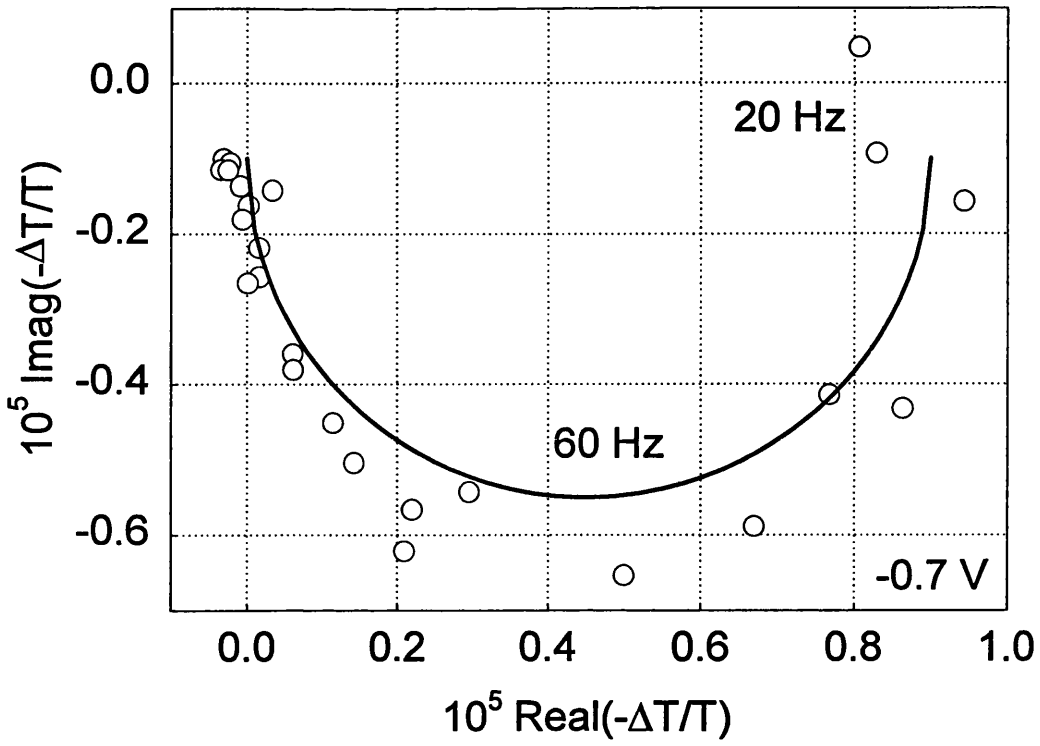

Figure 7.4(d). Potential dependence of the ac transmission at -0.7V of the nanoparticulate TiO_2 film at 940nm. The solid line represents the fitting with a semicircle.

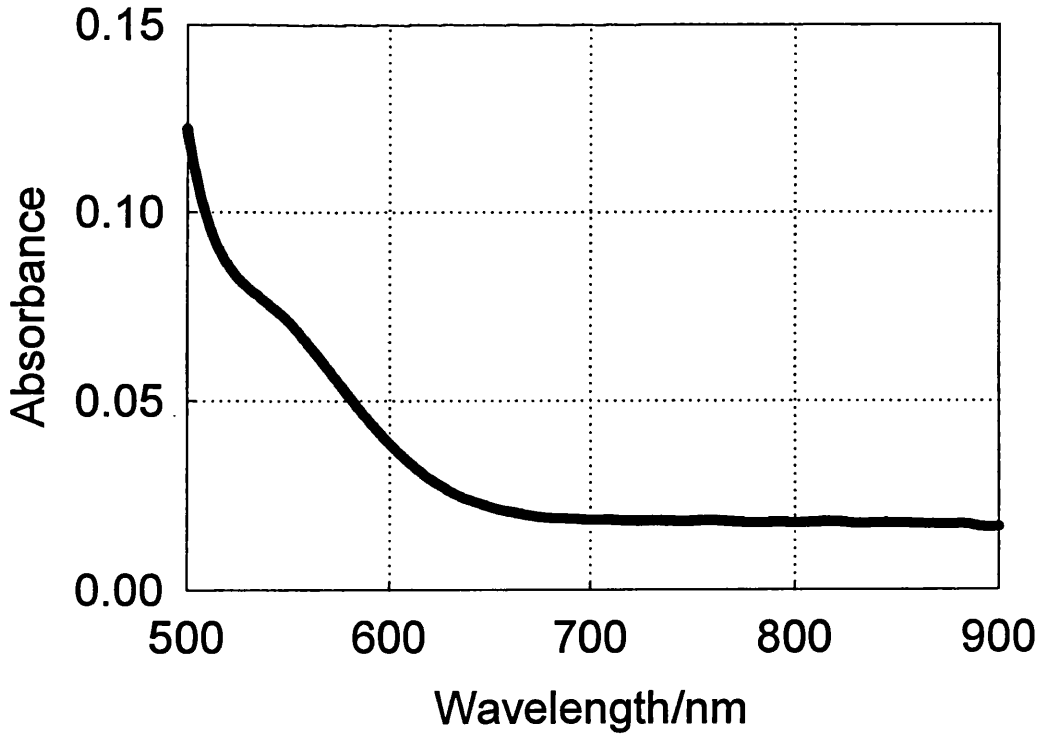

Figure 7.5. Absorbance spectrum of tri-iodide measured using 0.5M LiI and 0.5mM I_2 in acetonitrile.

7.5 Conclusion

Ac and dc potential-modulated infrared transmittance experiments have been performed on a TiO_2 nanoparticulate film in a saturated solution of LiI in acetonitrile between -0.55V and -0.7V vs. I^-/I_3^-. A very small variation of ω_{MIN} and of the low frequency intercept is observed, which suggests that in the voltage range analyzed the capacitance of free and trapped electrons in constant. Combining optical and impedance measurements, the optical cross section was evaluated and found equal to $5\times10^{-19}cm^{-2}$, which is smaller than the value found previously of $7.3\times10^{-18}cm^{-2}$. This discrepancy has been attributed to the fact that the contribution of free electrons is higher in the present experiment as the Fermi level is closer to the conduction band. This suggests that the optical cross section of free electrons is smaller than the one of trapped electrons at 940nm.

7.6 References

[1] G. Rothenberger, M. Grätzel and D. Fitzmaurice, J. Phys. Chem., 96, 5983, (1992).

[2] A. Many, Y. Goldstein and H. Z. Groover, 'Semiconductor Surfaces', Wiley & Sons, New York, (1965).

[3] S. R. Morrison, 'The Chemical Physics of Surfaces', Plenum Press, New York, (1977).

[4] A. Hagfeldt, U. Björkstén and M. Grätzel, J. Phys. Chem., 100, 8045, (1996).

[5] F. Cao, G. Oskam, P. C. Searson, J. M. Stipkala, T. A. Heimer, F. Farzard and G. J. Meyer, J. Phys. Chem., 99, 11974, (1995).

[6] A. J. Bard, A. B. Bocarsly, F-R. E. Fan, E. G. Walton, M. S. Wrighton, J. Am. Chem. Soc., 102, 3671, (1980).

[7] C. G. Granqvist, 'Handbook of Inorganic Electrochromic Materials', Elsevier

Science, Amsterdam, (1995).

[8] G. Boschloo and D. Fitzmaurice, J. Phys. Chem. B, submitted for publication.

[9] S. Södergren, H. Siegbahn, H. Rensmo, H. Lindström, A. Hagfeldt and S. E. Lindquist, J. Phys. Chem B, 101, 3087, (1997).

[10] A. Stashans, S. Lunell, R. Bergström, A. Hagfeldt and S. E. Lindquist, Phys. Rev. B, 53, (1996).

[11] B. Zachau-Christiansen, K. West, T. Jacobsen and S. Atlung, Solid State Ionics, 1176, 28, (1988).

[12] F. Bonino, L. Busani, M. Lazzari, M. Manstretta, B. Rivolta and B. Scrosatti, J. Power Sources, 6, 261, (1981).

[13] T. Ohzuku, Z. Takehara and S. Yoshizawa, Electrochim. Acta, 24, 219, (1979).

[14] T. Ohzuku and T. Kodama, J. Power Sources, 14, 153, (1985).

[15] T. Ohzuku and T. Hirai, Electrochim. Acta, 27, 1263, (1982).

[16] H. Lindström, S. Södergren, A. Solbrand, H. Rensmo, J. Hjelm, A. Hagfeldt and S-E. Lindquist, J. Phys. Chem. B, 101, 7717, (1997).

[17] H. Lindström, S. Södergren, A. Solbrand, H. Rensmo, J. Hjelm, A. Hagfeldt and S-E. Lindquist, J. Phys. Chem. B, 101, 7710, (1997).

CHAPTER VIII

CONCLUSIONS

8.1 Conclusions

Electron transport in dye-free [1] and dye-sensitised [2] nanoparticulate TiO_2 has been investigated using IMPS [3], IMVS [4], PEIS and PITS [5]. These techniques, which consist of an ac perturbation superimposed on a dc background, permit the linearisation of the response of electrochemical systems [6]. The combination of all these frequency-resolved measurements has proved a powerful tool in understanding the functioning of these novel structures. In the present work the fundamental aspects of frequency-resolved techniques were investigated from a theoretical point of view and related to the generation/collection equation developed by Södergen et al. [7]. This was extended adding the effect of trapping and detrapping for the single-trap case and related to the IMPS [8] and PITS [5] response. As for PEIS, the concept of non-linear circuit elements was introduced along with their corresponding differential quantities. The meaning of 'surface state capacitance' and 'conduction band capacitance', firstly introduced by Schlichthörl et al. [4], was clarified and related to IMVS measurements.

IMPS measurements were performed on dye-sensitised solar cells, this allowed the measurement of the diffusion time of electrons through the nanocrystalline network and therefore of their diffusion coefficient. Samples with similar film thicknesses ($\simeq\mu m$) gave reproducible values of the diffusion coefficient which was of the order of 10^{-5} cm^2s^{-1}. The IMPS measurements presented in chapter V were performed on two dye-sensitised solar cells prepared with different techniques (long and short impregnation), a

big excursion in the III quadrant, which was not predicted theoretically, was observed in the IMPS response of the cell with less dye. However, most dye-sensitised solar cells present this excursion in the IMPS response, the measurements in chapter VI show the same behaviour even though they were performed on a different sample. This suggested the presence of a dye-free region in the film, the simple generation/collection model was then modified introducing the effect of a 'dead layer' [9]. Excellent agreement was then found between the experimental IMPS response and the novel 'dead layer' model for a thickness of the dead layer of about half the total film thickness. The same anomaly, i.e. crossing of the real axis, in the IMPS response for illumination from the substrate side for dye-free TiO_2 was also observed. This suggested that the porosity of the TiO_2 is not uniform across the film, and therefore near the substrate, where there is low porosity, the net injection efficiency, η, approaches zero. The IMPS response was then fitted with the 'dead layer' model and excellent agreement was obtained for a compact region of the same thickness as the light penetration depth.

In chapter VI the IMPS, IMVS, PEIS and PITS responses of a single dye-sensitised solar cell were presented, the same experimental techniques applied to other samples showed a similar behaviour. Combining IMPS, IMVS, PEIS and PITS [5] the optical cross section of electrons at 940nm was determined, $7.3\times10^{-18}cm^{-2}$, as well as the net injection efficiency at open circuit, 0.3, and short circuit, 1. This indicates that under strong accumulation the reaction of electrons from the TiO_2 with the oxidised dye competes with the dye regeneration. It was found that the majority of the electrons detected are trapped at deep levels where they make no contribution to the measured photocurrent. Instead they react slowly with I_3^-, so that their lifetime is a measure of the rate constant for the back reaction via surface states. The rather poor agreement obtained between the single-trap generation/collection model and the PITS response suggests that a distribution of traps should be considered instead.

The model used to describe these systems has been discussed in the present work and modifications have been applied in order to obtained a better agreement with the experimental results. However further work is required to achieve a complete and more realistic picture of the mechanisms taking place in the device and especially the effect of trapping and detrapping. In the present work the trapping and detrapping rates have been considered constant, even though this approximation is acceptable for the former mechanism, it is not for the latter as it depends strongly on the trap energy. The model presented other limitations such as the fact that the diffusion coefficient was not considered distance dependent. As these imperfections of the model were acknowledged the experimental data were only partially fitted with the simulations.

Finally potential-modulated transmittance at 940nm was performed on porous dye-free TiO_2 under accumulation. The optical cross section of electrons was evaluated, $5\times10^{-19}cm^{-2}$. The discrepancy with this result and the value found previously was attributed to the fact that in this experiment the Fermi level is higher and therefore the contribution of free electrons to the optical response is dominant. However, it was not possible to achieve a complete picture of the mechanisms taking place in the system as under strong accumulation conditions the problems of lithium intercalation and band unpinning were encountered.

Other experimental techniques can be used in order to support and extend the results found in the present work. For example the non-uniformity of the films that the IMPS results suggested can be explored performing high resolution cross sectional imaging. This should give further information on the porosity of the TiO_2 film and the adsorption of the dye. Moreover, other infrared spectroscopy techniques can be applied in order to supplement the findings of this work and help to distinguish free and trapped electrons. Attempts have been made using a spectrographic array but due to thermal

fluctuations no reproducible results were obtained. This suggests the use of more sophisticated infrared techniques such as SNIFTIRS.

In conclusion a variety of frequency-resolved techniques were employed and photomodulated infrared transmittance spectroscopy was developed in this work. The combination of these techniques offers a powerful approach for the investigation of electron transport in porous systems. These techniques were also explored from a theoretical point of view. Work is in progress to expand the generation/collection problem to introduce a distribution of trap levels and the distance/density dependence of the parameters involved.

8.2 References

[1] P. E. Jongh and D. Vanmaekelbergh, J. Phys. Chem. B, 101, 2716, (1997).

[2] B. O'Regan and M. Grätzel, Nature, 353, 737, (1991).

[3] L. Dloczik, O. Ileperuma, I. Lauermann, L. M. Peter, E. A. Ponomarev, G. Redmond, N. J. Shaw and I. Uhlendorf, J. Phys. Chem. B, 101, 10281, (1997).

[4] G. Schlichthörl, S. Y. Huang, J. Sprauge and A. Frank, J. Phys. Chem. B, 1997, 101, 8141.

[5] G. Franco, J. Gehring, L. M. Peter, E. A. Ponomarev and I. Uhlendorf, J. Phys. Chem., 103, 692, (1999).

[6] F. Cao, G. Oskam, G. J. Meyer and P. C. Searson, J. Phys. Chem., 100, 17021, (1996).

[7] S. Södergen, A. Hagfeldt, J.Olsson and S.-E. Lindquist, J. Phys. Chem., 95, 5522, (1994).

[8] L. M. Peter, E. A. Ponomarev, G. Franco and N. J. Shaw, Electrochim. Acta, submitted for publication.

[9] G. Franco, L. M. Peter and E. A. Ponomarev, Electrochem. Comm., 1, 61, (1999).